

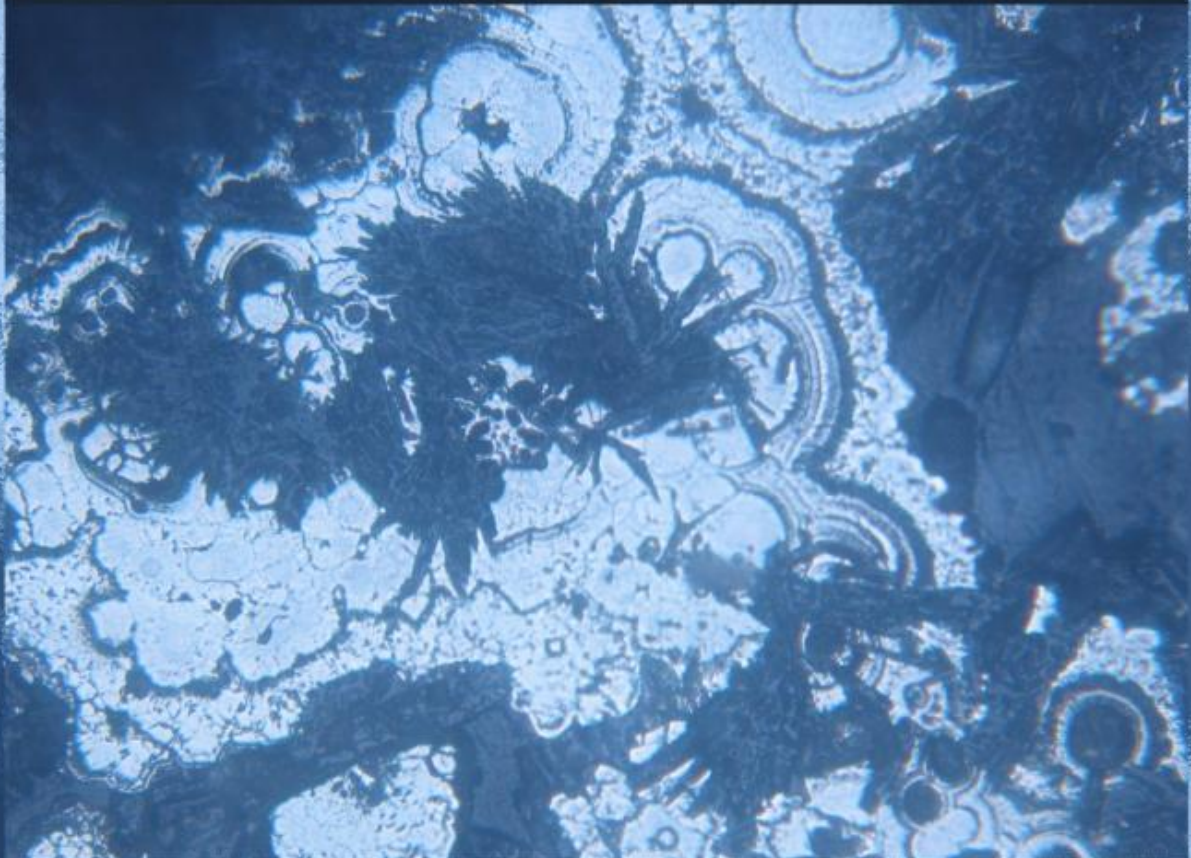


ΕΘΝΙΚΟ ΚΑΙ ΚΑΠΟΔΙΣΤΡΙΑΚΟ ΠΑΝΕΠΙΣΤΗΜΙΟ ΑΘΗΝΩΝ
ΣΧΟΛΗ ΘΕΤΙΚΩΝ ΕΠΙΣΤΗΜΩΝ ΤΜΗΜΑ ΓΕΩΛΟΓΙΑΣ ΚΑΙ ΓΕΩΠΕΡΙΒΑΛΛΟΝΤΟΣ

ΠΡΟΓΡΑΜΜΑ ΜΕΤΑΠΤΥΧΙΑΚΩΝ ΣΠΟΥΔΩΝ
"ΕΦΑΡΜΟΣΜΕΝΗ ΠΕΡΙΒΑΛΛΟΝΤΙΚΗ ΓΕΩΛΟΓΙΑ"

ΜΕΤΑΠΤΥΧΙΑΚΗ ΕΡΓΑΣΙΑ ΕΙΔΙΚΕΥΣΗΣ

"Antimony fixation in solid phases at the hydrothermal field of Kolumbo submarine arc-volcano (Santorini): deposit model and environmental implications"



ΓΟΥΣΓΟΥΝΗ ΜΑΡΙΑ

Επιβλέπων:

Στέφανος Κίλιας,
Αναπληρωτής Καθηγητής Ε.Κ.Π.Α

Εξεταστική Επιτροπή:

Αριάδνη Αργυράκη,
Επίκουρος Καθηγήτρια Ε.Κ.Π.Α

ΑΘΗΝΑ
ΙΟΥΛΙΟΣ 2014

Αθανάσιος Γκοντελίτσας,
Επίκουρος Καθηγητής Ε.Κ.Π.Α



ΕΘΝΙΚΟ ΚΑΙ ΚΑΠΟΔΙΣΤΡΙΑΚΟ ΠΑΝΕΠΙΣΤΗΜΙΟ ΑΘΗΝΩΝ

**ΣΧΟΛΗ ΘΕΤΙΚΩΝ ΕΠΙΣΤΗΜΩΝ
ΤΜΗΜΑ ΓΕΩΛΟΓΙΑΣ ΚΑΙ ΓΕΩΠΕΡΙΒΑΛΛΟΝΤΟΣ**

**ΠΡΟΓΡΑΜΜΑ ΜΕΤΑΠΤΥΧΙΑΚΩΝ ΣΠΟΥΔΩΝ
"ΕΦΑΡΜΟΣΜΕΝΗ ΠΕΡΙΒΑΛΛΟΝΤΙΚΗ ΓΕΩΛΟΓΙΑ"**

ΜΕΤΑΠΤΥΧΙΑΚΗ ΕΡΓΑΣΙΑ ΕΙΔΙΚΕΥΣΗΣ

**"Η ενσωμάτωση του Αντιμονίου στις στερεές φάσεις του
υδροθερμικού πεδίου του υποθαλάσσιου ηφαιστείου του Κολούμπο.
Μοντέλο γένεσης και περιβαλλοντική σημασία"**

ΓΟΥΣΓΟΥΝΗ ΜΑΡΙΑ

Επιβλέπων : Στέφανος Κίλιας, Αναπληρωτής Ε.Κ.Π.Α

Εξεταστική επιτροπή : Αριάδνη Αργυράκη, Επίκουρος Καθηγήτρια Ε.Κ.Π.Α

Αθανάσιος Γκοντελίτσας, Επίκουρος Καθηγητής Ε.Κ.Π.Α

ΑΘΗΝΑ

ΙΟΥΛΙΟΣ 2014



NATIONAL AND KAPODISTRIAL UNIVERSITY OF ATHENS

**SCHOOL OF SCIENCE
DEPARTMENT OF GEOLOGY AND GEOENVIRONMENT**

**ΠΡΟΓΡΑΜΜΑ ΜΕΤΑΠΤΥΧΙΑΚΩΝ ΣΠΟΥΔΩΝ
"ENVIRONMENTAL APPLIED GEOLOGY"**

MASTER'S THESIS

**Antimony fixation in solid phases at the hydrothermal field of
Kolumbo submarine arc-volcano (Santorini): deposit model and
environmental implications"**

GOUSGOUNI MARIA

Supervisor : Stephanos Kiliadis, Assoc. Professor
Examiners committee : Ariadne Argyraki, Assist. Professor
Athanasios Godelitsas, Assist. Professor

ATHENS

July 2014

Acknowledgements

A heartfelt thanks to my hardworking, patient, and dedicated supervisor, Dr. Stephanos P. Kiliadis for his encouragement and help on my journey of science maturity. Additionally special thanks also to my professors, Dr. Ariadne Argyraki & Dr. Athanasios Godelitsas, who supported me and provided me many useful comments and indications. The Synchrotron Radiation (SR) study was conducted by members of the Kolumbo Study Group Athanasios Godelitsas, Platon Gamaletsos, Theo J. Mertzimekis, Joerg Goettlicher, and Ralph Steininger at the ANKA facility, Karlsruhe Institute of Technology, (Germany) and was a fundamental addendum to my Msc thesis.

I am grateful for the help of Stathopoulou Elizabeth to careful preparation of the sulphide samples in the Lab of Historical Geology & Palaeontology, U.O.A. The opportunity to work and learn at her laboratory was an invaluable experience. Also, I thank Salaounis Panagiotis about the preparation of polished thin sections and polished blocks in the labs of I.G.M.E, (Attiki). Thanks to Stathopoulou Eleni for her supervision in sequential extraction methodology, conducted in the laboratories of Department of Chemistry, N.K.U.A. Furthermore, I would like to thank Stamatis Philippou, for his work on the solutions of Sequential Extraction steps, which were analyzed by inductively coupled plasma-mass spectrometry (ICP-MS), at Quality control laboratory for solid fuels, department of analytical laboratories (I.G.M.E-Attiki). Moreover I would like thank George Oikonomou, the director of the Laboratory of Mineralogy, Petrology and Economic Geology at National Technical University of Athens. Finally I wish to thank Evangelos Michailidis who helped navigate me through the world of the scanning electron microscope, housed in the Department of Geology and Geoenvironment at the N.K.U.A. and Dr Elias Chatzitheodoridis for his interest and his guidance in scanning electron microscope, housed at in the Laboratory of Mineralogy, Petrology and Economic Geology at National Technical University of Athens.

I was very fortunate to meet Marina Dimitroula who helped me gain experience and knowledge in ore microscopy. I am grateful for her help for taking some photos in optical microscope, housed in I.G.M.E. Addition to them I would like to thank Aikaterini Gousgouni for the professional photographs of the samples. Finally I want to thank the people of "Kolumbo team" for giving me the opportunity to participate in a scientific team and very interesting discussions. Special thanks to Paraskevi Nomikou for her positive attitude, her initiative, her dedication in Santorini research, the investigation for research financial

programs and for her great skills of communication. Finally I want to thank my friend and colleague Isidoros Livanos for his GMT maps I used in my Msc thesis.

Last but not least I would like to thank my friend and colleague Fotis Kafantaris for his advices and encourage starting this wonderful study. I would like to thank Zeno Sittas, who inspire me and always give me good energy, as well as, for the beautiful cover picture of the thesis. Finally, I want to thank my parents, Nikolaos Gousgounis and Eleni Koutsandrea and all my friends for being so supportive and offering me the basic values to be able to function and achieve my goals.

"The answer is never the answer. What's really interesting is the mystery. If you seek the mystery instead of the answer, you'll always be seeking. I've never seen anybody really find the answer, they think they have, so they stop thinking. But the job is to seek mystery, evoke mystery, plant a garden in which strange plants grow and mysteries bloom. The need of mystery is greater than the need for an answer".

Attributed to Ken Kesey

Table of Contents

List of Tables.....	iii
List of Figures.....	iv
ABSTRACT	xi
1. Introduction.....	1
2. Antimony in the environment: what we know and what we don't know.	3
2.1 Antimony in the terrestrial environment	5
2.2 Antimony in the aquatic environment (freshwater and seawater)	7
2.3 Antimony speciation in hydrothermal fluids.....	10
2.4 Antimony in seafloor hydrothermal systems	10
2.5 Speciation and incorporation of antimony into natural Fe-(oxy)hydroxides.....	17
2.6 Speciation and incorporation of antimony in pyrite	17
2.7 Antimony in organisms -Bioaccumulation.....	18
3. Antimony in the unique shallow-submarine volcano, Kolumbo (Santorini), Hellenic Volcanic Arc (HVA).....	20
3.1 Geodynamic and geological setting of the HVA	20
3.2 The Kolumbo submarine volcano and hydrothermal system	21
3.3 Antimony enrichment in Kolumbo, central HVA.....	28
4. Scope of thesis.....	31
5. Material and methods	32
5.1 Sampling	32
5.2 Preparation of samples.....	35
5.3 Analytical methods.....	40
5.3.1 Chemical analysis.....	40
5.3.2 Mineralogical analysis	43
5.3.3 Synchrotron Radiation analysis: Phase Contrast Imaging and Micro-spectroscopy	44
6. Results	45
6.1 Mineralogy and mineral chemistry	45
6.1.1 Politeia Vent Complex	45
6.1.2 Champagne Vent Complex	61

6.1.3 Active sulphide-sulphate mounds from Diffuser II complex	64
6.1.4 Anonymous Vent (AV)	66
6.2 Bulk Geochemistry of the Kolumbo chimneys	71
6.2.1 Major and trace elements	71
6.2.2 Rare earth elements geochemistry	73
6.2.3 Partitioning of elements in extractable phases.....	78
7. Discussion	80
7.1 The Kolumbo polymetallic seafloor hydrothermal chimneys	80
7.2 Source of antimony.....	81
7.3 Antimony fixation in seafloor hydrothermal solid phases	82
7.4 Rare earth element distributions	84
7.5 Genetic model of Sb mineralization and cycling within the Kolumbo chimneys	85
Second precipitated episode: Antimony in the OAsL (Fig. 7.2).....	87
Third precipitated episode: Antimony in the SFeC (Fig.7.3).....	87
Fourth precipitated episode: Antimony in the IPNC (Fig.7.4).	88
7.6 Environmental considerations.....	90
8. Summary and Conclusions	94
References.....	97

List of Tables

Table 5.1	List of samples which be made for mineralogical and geochemical studies. In this MSC thesis were studied the samples in red color.....	39
Table 5.2	The sequential chemical extraction scheme used in this study. (Motified after Rauret et al., 1999).....	41
Table 6.1	Major elements content (wt % except Ba in ppm) of hydrothermal vent samples from the Kolumbo deposits.....	72
Table 6.2	Minor elements content (in ppm) of hydrothermal vent samples from the Kolumbo deposits.....	73
Table 6.3	REE concentrations in ppm (mg kg^{-1}), chondrite normalized properties of REE enrichments and REE fractionation ratios of hydrothermal vent samples from the Kolumbo deposits analysed and seafloor hydrothermal deposits from various tectonic settings : Brothers Volcano (de Ronde et al., 2005); Tyrrhenian Sea Palinuro (Eckhardt et al., 2008), Galapagos rift (Tao et al., 2011).	75

List of Figures

Figure 2.1	Redox cycle of antimony in nature (modified after Boyle et al., 1983).....	4
Figure 2.2	Generalized biogeochemical cycle of antimony (modified after Boyle et al. 1983).....	5
Figure 2.3	Eh-pH diagram of antimony in the Sb-S-H ₂ O system at a dissolved antimony concentration of 10 ⁻⁸ mol/l and a dissolved sulfur concentration of 10 ⁻³ mol/l. (Modified after Filella et al., 2002b).....	9
Figure 2.4	Known sites of hydrothermal venting along mid-ocean ridges, in back-arc basins, rifted arcs, and at submerged island-arc volcanoes (red), and areas of activity as indicated by mid-water chemical anomalies (yellow)(Figure after Tivey et al., 2007).....	13
Figure 2.5	(a) Photograph of a black smoker chimney from the southern East Pacific Rise, taken from the submersible <i>Alvin</i> on Dive 3296 (courtesy of Woods Hole Oceanographic Institution (WHOI); M. Lilley and K. Von Damm chief scientists) and a schematic drawing showing across section of a black smoker chimney with one small pipe with slower advection and diffusion occurring across the walls. (b) Photograph of a 284°C diffusely venting spire from the Vienna Woods vent field in the Manus Basin taken on <i>Jason</i> Dive 207 (courtesy of WHOI; M. Tivey chief scientist), and a schematic drawing of the cross section across an East Pacific Rise diffusely venting spire that is composed of an inner, very porous zone of pyrrhotite (Fe _{1-x} S), wurtzite (Zn,Fe)S, and cubanite (CuFe ₂ S ₃); a less-porous mid layer of wurtzite, pyrite (FeS ₂) and chalcopyrite (CuFeS ₂); and an outer layer of marcasite (FeS ₂)(after Tivey et al., 2007).....	15
Figure 3.1	Location of Kolumbo submarine volcano within the Hellenic volcanic (Nomikou et al., 2013).....	21
Figure 3.2	Geodynamic setting of the Santorini-Kolumbo volcanic field (a-d): Schematic cartoons of different geodynamic environments where seafloor hydrothermal vents occur (Kiliass et al., 2013).....	24
Figure 3.3	Swath bathymetric map of the submarine Kolumbo volcanic chain using 10m isobaths. Right inset: Bathymetric map reciting the 19 volcanic domes in two	

	NE-SW trending lines. Left inset: Geographical index map (Nomikou et al., 2012).....	25
Figure 3.4	Swath bathymetry map of Christianna-Santorini-Kolumbo volcanic field (CSK) and tectonic zone (red line) (Nomikou et al., 2012).....	25
Figure 3.5	Detailed bathymetric map of Kolumbo hydrothermal vent field using 0,5m grid interval created with the ROV Hercules and the 1,375 kHz Blue View multibeam sonar in the northern part of the crater floor. (Kilias et al., 2013).....	27
Figure 3.6	Geochemical spidergram of selected trace metals from Kolumbo (see below) crater pumice, Santorini metamorphic basement and Santorini caldera bottom sediments (push core) (Kilias et al., 2014; Godelitsas et al., 2013)*. Concentrations are normalized to Upper Continental Crust (UCC) Rudnick et al., 2003).....	29
Figure 3.7	Geochemical spidergram of selected trace metals from Kos-Yali sediments, Methana sediments, and Milos and Santorini (Palaia and Nea Kameni) metalliferous sediments (Kilias et al., 2014; Godelitsas et al., 2013). Concentrations are normalized to Upper Continental Crust (UCC) (Rudnick et al., 2003).....	29
Figure 3.8	Geochemical spidergram comparing the investigations of Kolumbo polymetallic chimneys, with marine sediments of Hellenic Volcanic arc (Santorini, Milos, Methana). Data from: Gamaletsos et al. (2013); Kilias et al. (2013).....	30
Figure 3.9	Geochemical spidergram of selected trace metals from Kolumbo polymetallic chimneys, Santorini metamorphic basement and Santorini caldera push core. Concentrations are normalized to Upper Continental Crust (UCC) (Rudnick et al., 2003). Au: 32 ppm, Ag: 1,913 ppm, Pb: 6.7 wt %, Sb: 2.2 wt %). "Epithermal suite of elements" enrichment Au, As, Sb, Hg, Ag, Tl on the seafloor (Kilias et al., 2013).....	30
Figure 5.1	Ex-situ photographs of solid hydrothermal vent samples. Politeia Vent Complex.	33
Figure 5.2	Ex-situ photographs of solid hydrothermal vents samples, Champagne vent complex.	34
Figure 5.3	Ex-situ photographs of solid hydrothermal vent samples. Hydrothermal mound samples recovered from Diffuser II vent complex.....	34

Figure 5.4	Ex-situ photographs of solid hydrothermal vent samples. Sample NA014-016 was recovered from an anonymous active vent site at Latitude ($36^{\circ} 31.2020\text{N}$) and Longitude ($25^{\circ} 29.5877\text{E}$) at depth 499.7 m.....35
Figure 5.5	(a) Interior cut face of one halve of NA014-003. Polished thin sections D1,D2,D3,D4,D5,D6,D7,D8,CDE9',E8,FG2',FG4',EFG5',FG6',FG4'*,FG6'* were made based on a grid sampling strategy explained in the text. (b) View of exterior surface..... 36
Figure 5.6	(a) Interior cut face of one halve of NA014-039. Polished thin sections C2, C3, C4, C5, C6, C7, AB2', AB4') were made based on a grid sampling strategy explained in the text. (b) View of exterior surface.....37
Figure 5.7	The red arrow shows the cross section of orange-yellow slab. Two polished blocks were made (NA014-003-OAsL a, b).....37
Figure 5.8	Unidentified dark-violet phases similar to Sb-Zn-S are lining interior porous conduit network of (a) Sample NA014-003 (IPCN) –in polished thin section FG3 (Fig.2.5) (b) Sample NA014-003 (IPCN) –polished thin section EFG5'(Fig.2.5).....38
Figure 5.9	(a) Orange-yellow outer As-sulphide-dominated layer (OAsL) of Politeia spire 1, (b) small pieces recovered by OAsL (c) detail of b in reflected microscope.....38
Figure 6.1	Photomicrographs of commonly seen textures in the inner sulphide-sulphate core (ISSC).....47
Figure 6.2	Textures of pyrite/marcasite from the ISSC as observed in optical microscopy and backscattered electron images.....48
Figure 6.3	Politeia vent 1, sample 003, polished thin section EFG5.....49
Figure 6.4	Occurrence of Pb-Sb sulphosalt phases.....51
Figure 6.5	Politeia vent 1, sample 003, polished thin section EFG5. (a) Backscattered electron (BSE) image of finely concentrically laminated spheroids mantled by anhedral to subhedral intergrowths of Sb-Pb-sulphosalts. (b) Point of

analysis (in yellow) on μm -scale intermingle filament-like texture of sulphosalt phase. (c) SEM-EDS spectrum of the Sb-Pb-sulphosalt phase.....52

- Figure 6.6 Sample NA014-003, polished thin section D5: (a) Backscattered electron (BSE) image, and EDS spot analyses of concentrically laminated trace-metal (Sb, Pb) rich pyrite oncoïd (generation 1) with embedded galena (white), overgrown by thin porous spongy pyrite (generation 2). (b) Element profile across the pyrite oncoïd, by EDS spot analyses (Numbers on x-axis refer to analysis points).....53
- Figure 6.7 Sample NA014-003, polished thin section EFG5: (a) Backscattered electron (BSE) image of concentrically laminated pyrite oncoïd (pyrite 1), overgrown by thin porous spongy pyrite (pyrite 2). (b) Element profile (EDS spot analyses) across the spheroid (Numbers on x-axis refer to analysis points).....54
- Figure 6.8 Synchrotron radiation μ -XRF elemental distribution maps for Ba, Fe, Zn, As and Sb in an area dominated by layer of finely banded Fe-sulfide (light yellow), set in a barite matrix (Kilias et al., 2013b).....55
- Figure 6.9 (a) Normalized (edge jump of 1) Sb L3 XANES spectra of the sample (black) compared to the spectra of elemental Sb (blue), $\text{Sb}^{3+}\text{2O}_3$ (green) and Tripuhyite ($\text{Fe}^{3+}\text{Sb}^{5+}\text{O}_4$) (red). Note that Sb_2O_3 is not pure and seems to contain some Sb^{5+} which may have shifted the position of the Sb_2O_3 flank to a higher energy position than for pure Sb_2O_3 . (b) Derivatives of the normalized Sb L3 XANES spectra of the sample (black) compared to the spectra of elemental Sb (blue), $\text{Sb}^{3+}\text{2O}_3$ (green) and tripuhyite ($\text{Fe}^{3+}\text{Sb}^{5+}\text{O}_4$) (red). Note that Sb_2O_3 is not pure and seems to contain some Sb^{5+} (see the peak in its derivative at about 4143.6 eV) where the Sb^{5+} reference (tripuhyite) peak has its maximum. Strange is the position of the second derivative peak of the sample spectrum which plots significantly before the Sb^{3+} peak (Kilias et al., 2013b).....56
- Figure 6.10 (a) Photomicrograph taken in reflected light, of the outer As-sulphide layer (OAsL) of NA014-003: filamentous As-rich sulphides with typical colors of red and yellow; filament compositions approximate orpiment (As_2S_3) (characterized by XAFS) (Kilias et al., 2013). (b)(c)(d) SEM-BSE micrographs of hydrothermal precipitates with fragile morphologies: Overview of amorphous orpiment (As_2S_3)-type phase morphologies, including clustered microspheres and globular aggregates of various sizes (1-10 μm), and

- straight, curved and branching filaments with ringed grooves overlying layer of barite blades.....57
- Figure 6.11 (a) BSE image of colloform laminated orpiment (As_2S_3)-type As-sulphide phase (NA014-003 OASL). (b) Element profile across the colloform orpiment showing significant enrichment of in light laminae in Sb (up to 16wt%) (point 2).....58
- Figure 6.12 SEM images of Fe microbial mat designated as "surface Fe-rich crust" (SFeC). (a) (b) Amorphous Ferrihydrite-type (Characterized by XAFS) Fe-(hydrated)-oxyhydroxides occurring as laterally extensive slime-like material, forming an intimate extension of straight and/or curved filamentous, coccoidal, rod-shaped, and long straight stick structures (Kilias et al., 2013).....59
- Figure 6.13 (a)(b)(c) SEM-EDS elemental analysis collected from ferrihydrite-type Fe-(hydrated)-oxyhydroxides (NA014-0039 SFeC) gluing and overlying layer of barite blades and roses, indicates Sb content (The asterisks indicate the analysis point).....60
- Figure 6.14 EDS spectra show the presence of Zn and Sb. (The asterisks indicate the analysis point). (a) earthy mush of Sb-Zn-S phases in barite substrate, (b) Overview of Sb-Zn-S phase, possible biogenic, morphologies including curved and twisted hair like filaments entwined with each other forming dense arrays and colonizing barite crystal face (ba). A large variation in additional accumulation of oblate or imperfect aggregated microspheres developed on the surface of filaments (Kilias et al., 2013a).....61
- Figure 6.15 Photomicrographs of metallic phases. Sample NA014-028: (a) SEM-EDS photomicrograph shows colloform banded masses of amorphous trace-metal rich pyrite manded by barite blades. Spectrum diagrams show that core, "bright" zones in BSE, is enriched in Sb (up to 11 wt%), and/or Pb, As and Si.(b) Sample NA014-027:SEM-EDS photomicrograph shows laterally linked low-relief planar to domical (micro)stromatolitic pyrite morphology (Lazar et al., 2012; Alwood et al., 2006). (c) Cross-polarized RLP showing marcasite anisotropy, and plane polarized RPL showing marcasite pleochroism with inclusions of Cpx (d). (e) RLP of pyrite colloform banded planar layers commonly intergrowth with sphalerite (dark grey). (f) Intergrowths of pyrite/marcasite, chalcopyrite and Pb-Sb sulphosalts.....63
- Figure 6.16 (a) BSE image of intricate colloform banding of pyrite polished section NA014-027). (b) Elemental profile across the pyrite show chemical growth zoning defined by Cu and As variations. Sb is not be detected! (This picture

- is redrawn without the Fe and S ,because by this way the variation in As and Cu is shown better).....64
- Figure 6.17 Photomicrographs taken in reflected light of metallic phases. Sample NA014-005, polished block: (a) Barite laths and rosettes forming a substrate for disseminated sulphides of mainly colloform banded pyrite-marcasite (py-m) (b) Colloform banded pyrite intergrowth with barite overgrown by thin porous spongy pyrite(generation 2). (c) Porous spongy pyrite (generation 2) overgrown by eudral pyrite (generation 3) (d) Pyrite-sphalerite-barite intergrowth. (e) Idiomorphous crystals of pyrite intergrowth with barite (f) Spherical aggregates of Pyrite-Marcasite.....65
- Figure 6.18 Photomicrographs, taken in reflected light of Pb-Sb sulphosalt phases (Sample NA014-005, polished block: (a),(b) Spherules of pyrite, with concentric lamina, rimmed by a serrated Sb-Pb sulfosalts bright rim, in barite matrix (c) Random concentrically laminated, zoned Sb-rich pyrite spheres (microglobles) rimmed by dentate Sb-Pb sulphosalts (white) in massive pyrite; the latter is intergrown with or overgrown by barite laths. (d) Inclusions of Sb-Pb sulphosalts in pyrite intergrown with sphalerite.....66
- Figure 6.19 SEM backscatter images of anonymous vent (NA014-016) mineral phases.....68
- Figure 6.20 (a) SEM-EDS photomicrograph shows colloform banded masses of amorphous trace-metal rich pyrite mantled by barite blades. (b)Spectrum diagrams show that core, “bright” zones in BSE, is enriched in Sb (up to 11 wt%), and/or Pb, As and Si (spectrum 1,3).....68
- Fig.6.21 SEM-EDS elemental maps for Ba, Fe, Pb, Sb and S show that Pb may be concentrated in thin layer of galena (PbS) mantling the pyrite spheroids (Kilias et al., 2013 b).....69
- Fig.6.22 Anonymous Vent (AV) sample NA014-016 (ISSC): (a) BSE image of colloform overgrowths with trace metals-rich cores (light grey) interpreted as colony of pyrite in association with galena (b)SEM-EDS spectrum showing significantly high amount of Sb, Pb, Cu, Zn in core of colloform pyrite.....70
- Figure 6.23 Anonymous Vent (NA014-016): (a) Backscattered electron (BSE) image of concentrically laminated trace-metal (Sb, Pb) rich pyrite spheroid (generation 1) overgrown by thin white lamination of galena and overgrown by microcrystalline masses of pyrite (generation 2) with white inclusions of

	galena (3 wt% Sb). (b) Element profile across the pyrite spheroid. (Numbers on x-axis refer to analysis points).....	71
Figure 6.24	Chondrite-normalized REE patterns for representative samples of Politeia Vent Field (NA014-003 ISSC, NA014-003 CRUST, NA014-039 ISSC, NA014-039 CRUST, NA014-016 CRUST), compared to Upper Continental Crust (UCC)(black) and seawater (Tanaka. et al., 1990).....	76
Figure 6.25	REE abundance patterns normalized to chondrite for Champagne's samples (NA014-007,NA014-027,NA014-028), the Upper Continental Crust (UCC)(-in black) and seawater (Tanaka. et al., 1990).....	76
Figure 6.26	REE abundance patterns normalized to chondrite for Diffuser's sample (005) and the Upper Continental Crust (UCC)(-in black) and seawater(Tanaka. et al., 1990).....	77
Fig.6.27	REE abundance patterns normalized to chondrite for AV sample (NA014-016) and the Upper Continental Crust (UCC) (-in black) and seawater (Tanaka. et al., 1990).....	77
Fig.6.28	Binary plot of $(Ce/Ce^*)_{SN}$ against $(Pr/Pr^*)_{SN}$ to distinguish between anomalous Ce_{SN} and La_{SN} behavior for the Samples of the Kolumbo chimneys (after Bau and Dulski, 1996).....	78
Figure 6.29	Extractability order of the studied elements in each extraction stage of the BCR sequential extraction procedure and residual phase for 5 samples.....	79
Figure 7.1	Deposition model. First precipitated event: Antimony in ISSC of Politeia Chimneys (Modified after Kiliass et al., 2013).....	89
Figure 7.2	Deposition model. Second precipitated event: Antimony in OASL of politeia chimneys (Modified after Kiliass et al., 2013).....	89
Figure 7.3	Deposition model. Third precipitated event: Antimony in SFeC of politeia chimneys (Modified after Kiliass et al., 2013).....	90
Figure 7.4	Deposition model. Fourth precipitated event: Antimony in IPNC of politeia chimneys. (Modified after Kiliass et al., 2013).....	90

ABSTRACT

Submarine volcanic arcs represent a previously unheeded but potentially extensive source of shallow (<2 km water depth) vent fields expelling fluids of potential environmental and economic significance into the oceans. The observed metal enrichments in Sb and Tl (Hg, As, Au, Ag, Zn) of hydrothermal solids on the floor of the acidic (pH~ 5) crater of the Kolumbo shallow-submarine (<505 m water depth) arc-volcano, near Santorini, have implications for toxic metal (i.e. Tl, Sb, As, Hg) transport and biogeochemical cycling in seafloor hydrothermal systems, and underscores the importance of submarine volcanic and hydrothermal activity as sources of toxic metals in the oceans.

Despite its notoriety as an environmental toxin, antimony (Sb) is one of the few elements, which has been rarely investigated in the marine hydrothermal vent environment. Motivated by the virtual lack of investigations, we explored the fixation of Sb in seafloor hydrothermal solid phases of the Kolumbo (Santorini) shallow-marine active hydrothermal field. Here we report on the results of optical and Scanning Electron Microscopy-Backscattered Electron (SEM-BSE) studies, combined with Synchrotron Radiation (SR) based μ -XRF elemental mapping, and μ -XAFS spectra at LIII-edge for Sb studies of these mineral phases, and bulk trace and RE elements geochemical studies, in an attempt to decipher the inorganic and possibly biogenic mode(s) of deposition of Sb and the consequent environmental implications.

Bulk Rare Earth Element(REE) characteristics of Sb-rich samples, such as positive Eu anomalies, and lack of seawater REE signature and strong negative Ce anomaly, and light-REE enrichment, combined show that Kolumbo solid precipitates are derived from seafloor venting of reducing evolved hydrothermal fluids.

Antimony mineralization is ubiquitous throughout the life of particular hydrothermal edifices. Four (4) distinct modes (A-D) of Sb sequestration and enrichment have been revealed in ore-grade samples (≤ 2 wt% Sb) from different mineralogical zones of diffuser chimneys (i.e. ISSC, OAsL, SFeC, IPCN): (A) High concentrations (up to 11 wt% Sb) occur in micron-scale concentric zones of laminated chemically-zoned pyrite/marcasite (ISSC), where Sb may occur in the reduced relatively more toxic Sb^{3+} form, in accordance with high organic carbon content ($C_{org} \leq 5.3$ % TOC), and reducing hydrothermal fluids. Antimony and Pb either occupy the Fe and S sites, and/or at least part of the Sb occurs in sulphosalt nanoparticles of Sb and Pb, in the pyrite/marcasite structure; the concentration of Pb is considered important

in controlling the uptake of Sb into the pyrite/marcasite structure. Therefore, the control that pyrite e/marcasite apply to the concentration of Sb, and possibly other trace metals of economic and environmental importance, in shallow-seafloor hydrothermal vents, is more significant than previously thought. Antimony is additionally partitioned in individual antimoniferous crystalline phases that are clearly visible in optical microscopy and SEM-EDS and constitute unidentified non-stoichiometric $Pb_nSb_mS_p$ sulphosalts. (B) The highest concentrations of Sb (up to 16 wt %) are found in growth zones of colloform banded orpiment (As_2S_3)-type As-sulphide phases (OAsL). (C) Antimony is linked with poorly ordered ferrihydrite-type (characterized by XAFS), Fe-(hydrated)-oxyhydroxides (SFeC). This is the first time that Sb is reported linked with short-ordered Fe^{3+} -oxyhydroxides/ferrihydrite in shallow-marine hydrothermal systems associated with submarine arc-volcanos. (D) Unidentified antimoniferous ($Zn_mSb_nS_p$) sulphosalt phases occur as dark violet metallic aggregates, as well as filaments, in the interior porous conduits (IPCN).

The selective partitioning of Sb is most likely the result of changes in hydrothermal fluid composition, as well as pH and temperature, which are likely linked to the episodic nature of the Kolumbo hydrothermal vent system, i.e. periodic influx of magmatic hydrothermal fluids and associated cycles of Sb-(Pb) rich hydrothermal activity. Alternatively, these variations can evolve from ultra-local fluid composition variations due to short-lived fluid flow events linked to a seismic cycle, or they may suggest different chemical microenvironments within chimneys that may arise from geomicrobiological processes.

The most important implication of the discovery of possibly biogenic filamentous fungal and/or microbial $Zn_mSb_nS_p$ is that this is a mechanism of bio-sequestration of hydrothermal Sb in solid phases at seafloor hydrothermal sites, not recognized before. Moreover, Sb linked with the biogenic ferrihydrite-type Fe^{3+} -(hydrated)-oxyhydroxides on the surface of the Kolumbo chimneys (SFeC) may prove very helpful for making predictions on the long-term fate of Sb associated with ferrihydrite in such shallow seafloor hydrothermal systems environments. Moreover, It is also possible that extremophile biota (bacteria or Archea) may thrive on and in the antimoniferous Fe-rich layers, and those microorganisms may possess enzymes that allow them to survive in such toxic environments.

The solid phases that fix Sb on the seafloor are proved crucial for reducing the high hydrothermal flux of this notorious environmental toxin to seawater, near the fishing area of Santorini that is also one of the most popular tourist places in the world. Moreover, these

results offer novel insights to the geoenvironmental and biogeochemical Sb-cycle in the marine environment.

All our results emphasize the weight of shallow-submarine geothermal activity as a potential source of toxic metals (Sb^{3+}) during seafloor weathering, and/or natural disasters (i.e. explosive volcanic/hydrothermal, and seismic activity).

1. Introduction

Antimony (Sb), atomic number 51 (atomic mass: 122), is a trace element and the 63rd most abundant of the 92 naturally occurring elements in the Earth's crust, with concentrations of 300 $\mu\text{g}/\text{kg}$ (0.3 mg/kg or ppm) in the continental crust (**Wedepohl, 1995**), in unpolluted natural fresh waters typically below 1 $\mu\text{g}/\text{L}$ (0.001 ppm) (**Fouquet et al., 2010**), and in ocean seawater between 1.7 and 3.8 nmol/L (**Filella et al., 2002a**). Antimony is a metalloid that belongs to Group 15 of the periodic table along with nitrogen (N), phosphorus (P), arsenic (As), and bismuth (Bi); it has been exploited since the beginning of modern civilization and belongs to the critical raw materials on the European Union level (**Maher, 2009; Majzlan and Filella, 2012; Critical Raw Materials for the EU (2010)**). Antimony is broadly used in a variety of products such as batteries, flame retardants, textiles, plastics, ammunition, ceramic opacifiers, glass decolorizers and certain therapeutic agents (**Filella et al., 2002a**); the worth of Sb to such diverse industries as nanotechnology and health is highlighted by the fact that it is currently the 9th-most mined metal worldwide.

Recent reports show that Sb in the environment is an emerging toxic contaminant, a potential human carcinogen and a new puzzle of global concern (**Filella and Williams, 2012; Wilson et al., 2010; Roper et al., 2012; Maher, 2009; Amarasiriwardena and Wu, 2011; Beyersmann and Hartwig, 2008**). Antimony and its compounds have been regarded as pollutants of priority interest by the United States Environmental Protection Agency (USEPA) and the European Union (EU) (**Filella et al., 2002a**). It's on the list of hazardous substances under the Basel convention concerning the restriction of transfer of hazardous waste across borders (United Nations Environmental Program, 1999). It is of significant environmental concern because of its high toxicity and the growing contamination of waters and soils in certain regions from mining, industry, and fire arms (**e.g. Scheinost et al., 2006**). Although its toxicity mirrors that of its Group 15 neighbor arsenic, its environmental chemistry is very different, and, unlike arsenic, relatively little is known about the fate and transport of Sb, especially with regard to biologically mediated redox reactions (**Filella et al., 2007**). One of the most urgent questions yet to be answered concerning the chemistry of antimony (**Maher et al., 2009**) concerns the forms that antimony takes, and how does it cycle through different environmental compartments.

Natural antimony abundances are disturbed by anthropogenic and natural factors which largely exceed physical fluxes and concentrations (**Filella et al., 2002a**). Antimony is

among those trace elements that are exported by from the lithosphere, hydrosphere and atmosphere to the ocean; high amounts of antimony can be discharged into the oceans by continental riverine runoff affected by mining or industrial effluents (**Filella et al., 2002a**), natural sources such as geothermal fluids (**Douville et al., 1999**), atmospheric precipitation (**Shotyk et al., 2005; Krachler et al., 2005**), and possibly biological activity (**Filella et al., 2007; Abin and Hollibaugh, 2013**). Up to date underestimated and virtually unstudied input is contributed by submarine hydrothermal fluids discharging at the seafloor at concentrations up to several hundred times those of seawater (**Douville et al., 1999; Fouquet et al., 2010**). Studies of antimony speciation in seafloor hydrothermal vent environments are very scarce, and the effects of different ligands, mineral and organic surfaces or particles and live organisms on Sb mobility in seawater are insufficiently known. A recent study of the Kolumbo submarine arc-volcano, Santorini, has highlighted the importance of submarine volcanic-geothermal activity as a source of seawater acidity and potentially toxic trace metals, including antimony, to microbial metabolism and marine food webs, and in areas exploited by fishing (**Kilias et al., 2013**). It is critical for such hazard assessment having measurements of trace metals on seabed and sea column materials as well as study the fixation and speciation in solid phases. Antimony fixation in solid phases at the submarine hydrothermal vents is essential for reducing the high hydrothermal flux of this toxic element to seawater and is an important part of the biogeochemical antimony-cycle (**Dekov et al., 2013**). Therefore, this thesis will focus on the accumulation and transformation of potentially toxic element antimony in seafloor hydrothermal vent solid phases and its possible environmental fate, using the Kolumbo shallow-submarine hydrothermal field as a natural laboratory.

2. Antimony in the environment: what we know and what we don't know.

Unless otherwise noted, the following synthesis is based on **Fillela et al. (2002a,b, 2007, 2009, 2012)**, **Reimann et al. (2010)**, **Maher et al. (2009)**, **Gunn, (2013)** and **Borch et al. (2009)**.

Life and element cycling on Earth are directly related to biochemical redox processes, which control the chemical speciation, bioavailability, toxicity, mobility and therefore the environmental fate of many major and trace elements (Fe, Mn, C, P, N, S, Cr, Cu, Co, As, Sb, Se, Hg, Tc, and U) and play key roles in the formation and dissolution of mineral phases. Redox cycling of naturally occurring trace elements and their host minerals controls the release or sequestration of inorganic contaminants. Solution speciation of many elements control the chemical behavior and influences solubility, bioavailability, adsorptive phenomena and oceanic residence times, volatility and oxidation/reduction behavior (**Byrne, 2002**). The total concentration of an element in a system doesn't necessarily represent its biological availability or potential toxicity (**Newman and Jagoe, 1994**). 'Bioavailability' is a function of the abundance and chemical form of the toxin in solution (i.e. oxidation state), the nature of its binding to sediment grain (**Newman and Jagoe, 1994**) and also the degree to which an element or molecule is able to move into or onto an organism (*sensu* **Benson, 1994**).

Antimony occurs in four oxidation states [Sb(V), Sb(III), Sb(0), and Sb(-III)]. The two oxidation states +3 and +5 predominate in environmental samples and mineral deposits (see also **Boyle et al., 1983; Gunn, G., 2013**). Antimony has two naturally occurring stable isotopes (^{121}Sb and ^{123}Sb) with abundances of 57.21% and 42.79%, respectively. Zerovalent antimony occurs in nature as native antimony and in certain metallic alloys (immobile forms). The mobile trivalent antimony forms (SbO_3^{3-} , Sb^{3+}) occur in nature as oxides and sulphides in soils and colloidal gels, soluble species, complex ions in solution, absorbed ions in organic chelates and colloids, as volatile hydrides and in hydrocarbons. Thermodynamic calculations showed that the hydroxide complex $\text{Sb}(\text{OH})_3(\text{aq})$ (antimonite) is primarily responsible for hydrothermal transport of antimony, especially at temperatures above 250°C (**Zotov et al., 2003**). The mobile pentavalent antimony forms (e.g. SbO_4^{3-} and thioantimonates) occur in nature as oxides in soils, in iron- hydrous manganese colloids, as organic chelates or in gels, antimonate or thioantimonate ions in solution, as complex ions or polymeric ions in solution and in hydrocarbons. On the other hand the immobile

trivalent/pentavalent forms occur in oxide, sulphide, and various complex antimonites /antimonates, in hydrous manganese oxide rich gels, in iron-manganese rich organic matter, in plants and in animals.

A generalized cycle of antimony interconversions in nature is shown in Figure 2.1. Zerovalent antimony oxidizes to trivalent antimony by O_2 , metal ions etc. The direct oxidation of zerovalent antimony to pentavalent is rare. For trivalent antimony the mechanism appears to be reduction to zerovalent antimony under chemical, biological and photochemical conditions and oxidation to pentavalent antimony in solution or by action of bacteria. For pentavalent antimony the mechanism appears to be reduction to trivalent antimony under chemical or bacterial conditions. Direct reduction to zerovalent antimony is rare.

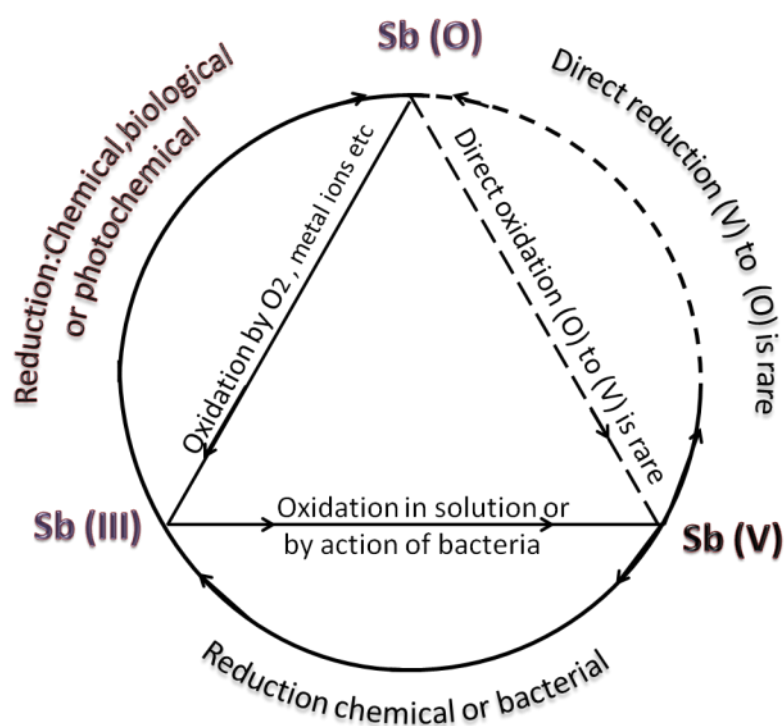


Fig.2.1 Redox cycle of antimony in nature (modified after Boyle et al., 1983)

The biogeochemical cycle of antimony through the atmosphere, biosphere, pedosphere, lithosphere, and hydrosphere is shown in Figure 2.2; the speciation, toxicity and bioavailability of antimony in the various compartments of the cycle are considered in some detail below. Very recent findings make predictions on the fate of antimony in aquatic environments, and evoke the prospect of a microbial biogeochemical antimony cycle in natural environments (**Mitsunobu et al., 2010, 2013; Kulp et al., 2013; Abin and Hollibaugh, 2013**).

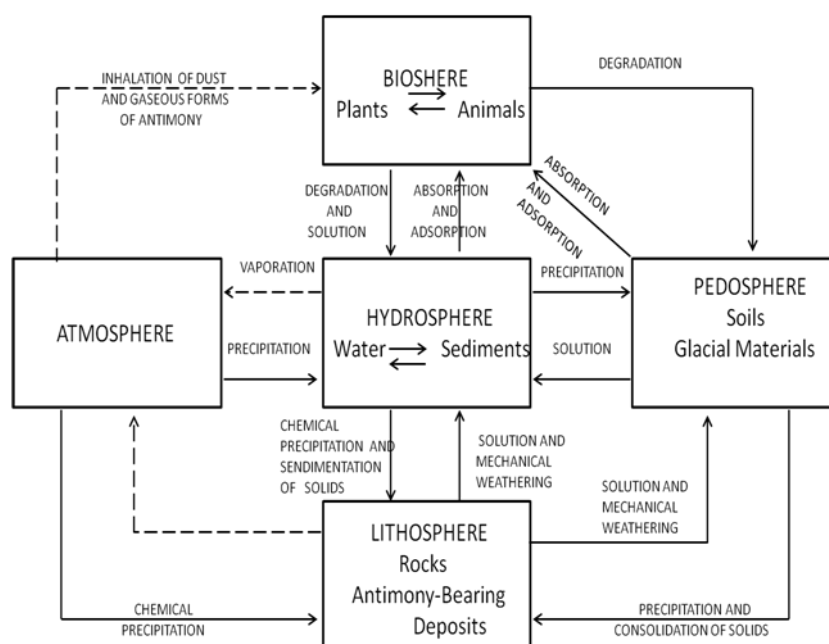


Fig.2.2 Generalized biogeochemical cycle of antimony (modified after Boyle et al. 1983)

2.1 Antimony in the terrestrial environment

Antimony concentration in normal sediments and soils in various localities of the world is about 0.18-2.5 ppm, except for areas near ore deposits containing the element (**Boyle et al., 1983**). Elevated concentrations of antimony in soils and sediments are either related to anthropogenic sources or associated with high arsenic concentrations in sulphide ores (**Filella et al., 2009**). Antimony fate in soils may be a key element in antimony cycling in the environment (**Filella et al., 2002a**). Available data showed antimony accumulation near the soil surface, followed by a concentration decrease with depth, suggesting that the source is most probably atmospheric and that antimony is rather non-reactive in these media (**Filella et al., 2002a and references therein**). It's generally accepted that antimony is

essentially immobile in soils (**Filella et al., 2009**). The form antimony arrives in contaminated soils near mines and smelters is Sb_2O_3 and is mostly immobile, because much antimony remains as non-reactive oxides (**Filella et al., 2009 and references therein**). However it's generally accepted that antimony is present as Sb^{5+} in soils (**Oorts et al., 2008**). Soil mineralogy plays an important role in the bioavailability of antimony in defunct mine sites and the incorporation of antimony in plants depends on the mobility and fate of the host mineral phase of antimony (**Perez-Sirvent et al., 2011**).

Antimony belongs to a group of metals and metalloids, usually referred to as the "epithermal" suite of elements, which includes gold, silver, tellurium, selenium, mercury, arsenic, antimony and thallium (e.g. **Taylor, 2007**). Antimony is widely present in many types of mineral deposits in trace, minor and major amounts. An estimate of 165,000 tons of Sb were produced worldwide in 2008 (U.S Geological Survey Mineral Resources Program, 2009), with China being the most important producer (**Fan et al., 2004**). High antimony concentrations are generally associated with high arsenic concentrations in sulphide ores. The use of antimony concentration in soils has been proposed as pathfinder for gold, confirming the chalcophilic nature of this element. It is concentrated in sulphide-enriched deposits as a separate mineral or as a trace constituent of sulphides, arsenides, and sulphosalts (**Filella et al., 2002a, Filella et al., 2009**). The most common primary antimony minerals in hypogene mineral deposits are native antimony (Sb), stibnite (Sb_2S_3) and a great variety of sulphosalts the most of which are tetrahedrite ($(\text{Cu,Fe})_{12}\text{Sb}_4\text{S}_{13}$), jamesonite ($\text{Pb}_4\text{FeSb}_6\text{S}_{14}$), boulangerite ($\text{Pb}_5\text{Sb}_4\text{S}_{11}$), bournonite (PbCuSbS_3), polybasite ($(\text{Ag,Cu})_{16}\text{Sb}_2\text{S}_6$), and pyrargyrite (Ag_3SbS_3). The most common secondary minerals in deposits are kermesite, seramontite, stibiconite, nadorite, and bindheimite (**Boyle, 1983**).

Most antimony deposits are of hydrothermal origin (Gunn, 2013, and references therein). Three main antimony deposit types can be distinguished, based on fluid generation and metal source: (i) low-temperature hydrothermal (epithermal) origin in shallow crustal environments associated with magmatic fluids; (ii) metamorphogenic hydrothermal associated with magmatic heat and expelled fluids; and, (iii) reduced intrusion-related gold systems. The highest antimony concentrations commonly occur in low-temperature magmatic hydrothermal systems in the epithermal environment.

Major styles of antimony ores are:

- **Gold-antimony epithermal deposits.**

Epithermal type antimony deposits include strata bound mantos (e.g. Wadley, Sierra de Catorce antimony district, Mexico), vein deposits controlled by fault zones (e.g. Bolivian antimony belt), fault-controlled veins and limestone replacements (e.g. Bau district, Sarawak, Malaysia) and Carlin-type gold (arsenic, mercury, antimony) deposits (e.g. Getchell, Turquoise Ridge, Twin Creeks, Nevada; Zarshuran, Iran; Alsar, FYROM). According to **Muntean et al., (2011)** the most important economic manifestation of this activity is the formation of Carlin-type gold deposits (CTGDs) in northern Nevada, which contain over 6,000 tons of gold (Au), constituting the second largest concentration of Au in the world. The deposits account for 6% of annual worldwide production, making the United States the fourth largest producer of Au.

- **Greenstone-hosted quartz-carbonate vein and carbonate replacement deposits.**

Examples of syn-orogenic hydrothermal antimony-gold deposits occur in Archean greenstone terrains in Southern Africa (e.g. the Antimony Line, Murchison, South Africa; and the Kadoma and Kwekwe goldfields, Zimbabwe (**Buchholz et al., 2007**).

- **Reduced magmatic gold systems.**

Type examples of reduced intrusion-related gold systems are known in the Fairbanks area of central Alaska (e.g. Ford Knox deposit) and central Yukon (e.g. Tombstone gold belt;), southern New Brunswick, the Bolivian polymetallic belt and the Yanshanian orogen of the North China craton (**Thompson et al., 1999**)

2.2 Antimony in the aquatic environment (freshwater and seawater)

The maximum contaminant level (MCL) of antimony in drinking water is regulated to be 6 µg/L by United States Environmental Protection Agency (USEPA), and set to be 5 µg/L in EU and China. Although the concentration of antimony or Sb³⁺ in natural waters is normally below 1 µg/L (Filella et al., 2002a), yet in contaminated locations especially around shooting ranges, mining and smelter industrial sites, large quantities of antimony have been released into the environment with concentrations up to 100 times the natural levels (Filella et al., 2002a). Antimony is present in the freshwater environment because of rock weathering, soil runoff and anthropogenic activities; for example airborne Sb in sediments from Qinghai lake in the northwest region of the Qinghai Plateau in China (e.g. Xu et al., 2011), and considerable concentrations in hot spring precipitates, boreholes and geothermal waters

(Filella et al., 2002a). According to Filella et al. (2002a) concentrations of antimony ranging from 500 mg/l up to 10 wt. % can be readily determined using analytical techniques such as ICP-MS and ICP-OES. Antimony concentration in seawater is about 200 ng/l (Filella et al., 2002a). Some authors report that antimony behavior in open oceans is not considered to be highly reactive and others believe that antimony shows a pattern corresponding to a mildly scavenged element with surface (atmospheric) input. Antimony behavior in estuaries seems to be rather variable depending on the estuary characteristics.

Knowledge of trace element speciation in waters is important to understanding the aquatic toxicity and bioaccumulation in natural water, as well as partitioning between water and colloidal and particulate phases (Florence et al., 1992). Antimony as well as several other elements, such as As and Cr, are more difficult to characterize because they occur in several oxidation states in sediments and water, hence they have a different degree of bioavailability (Gebel et al., 1997). Trivalent species are reported to be more toxic than pentavalent forms (Bencze et al., 1994). Pentavalent antimony form is the predominant oxidation state in surface waters, whereas, trivalent antimony form is usually found in anoxic environments such as groundwater and sediments (Leuz et al., 2005).

Under oxic conditions pentavalent antimony is the predominant species in different marine water, freshwater, groundwater and rain water, however thermodynamically unstable trivalent antimony has also been detected (Filella et al., 2002a *and references within*). Some authors invoke biological activity as the cause of trivalent antimony presence in aquatic environments (Kantin et al., 1983; Andreae et al., 1984) and some others pointed out the convenience of considering photochemical reduction of pentavalent antimony as a potential source of the trivalent form (Cutter et al., 2001). Under anoxic conditions the speciation of antimony remains unclear. According to thermodynamic calculations, antimony should be completely present in trivalent form, but also oxidised antimony species $[Sb^{5+}]$ has also been detected in different systems (e.g Black sea) (Cutter et al., 1991). This can be explained with the following mechanisms: (i) delivery of pentavalent antimony forms on sinking detritus from oxic waters (Andreae et al., 1984, Cutter et al., 1991) (ii) formation of thiocomplexes with the pentavalent element (Andreae et al., 1984) and (iii) advection of surface waters containing high concentrations of antimonate (Cutter et al., 1991).

Depending on chemical conditions such as pH, temperature, and redox potential, elements will exist in different forms. Pentavalent antimony in seawater is present dominantly as (antimonate) $Sb(OH)_6^-$ and the speciation of the trivalent form is similar to

that of Bi in that Sb(OH)_3^0 (antimonite) is dominant over a wide range of pH (Byrne, 2002). The redox behavior of antimony can be illustrated by Eh-pH diagrams (Fig. 2.3). According to this diagram, antimony is present as soluble Sb(OH)_6^- in oxic systems and as soluble Sb(OH)_3 in anoxic ones at natural pH values. Under reducing conditions, and in the presence of sulfur, insoluble stibnite, Sb_2S_3 is formed at low to intermediate pH values. At higher pH values, the SbS_2^- species replaces stibnite (Filella et al., 2002b).

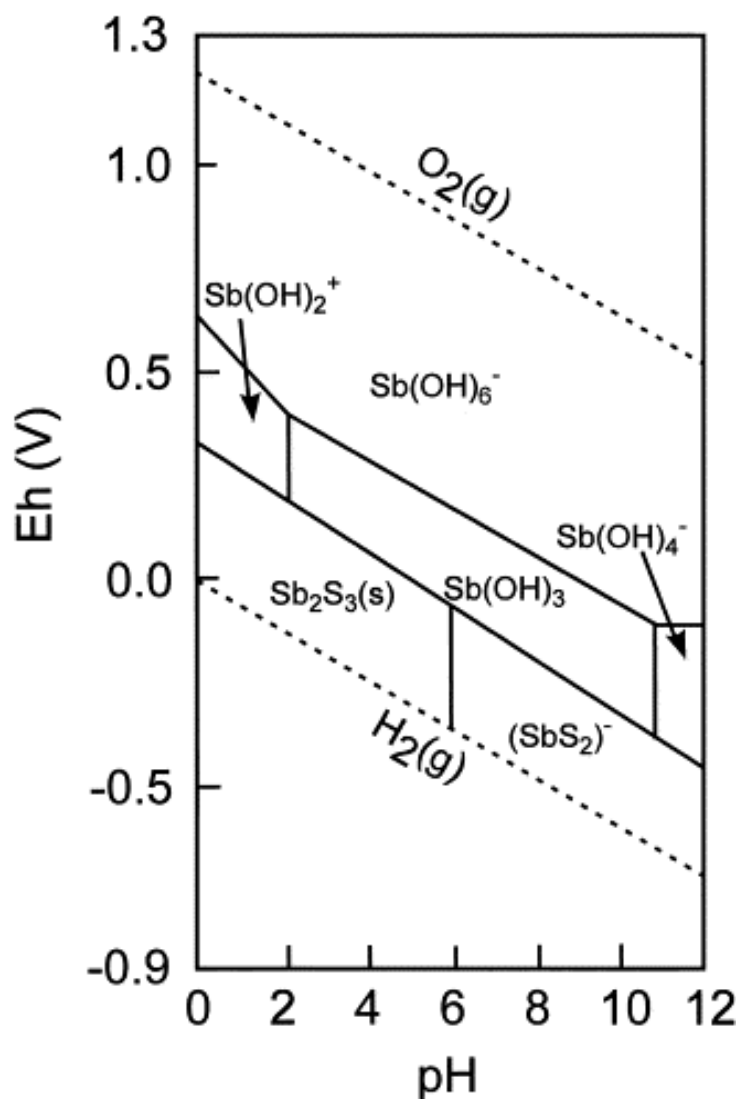


Fig.2.3 Eh-pH diagram of antimony in the Sb-S- H_2O system at a dissolved antimony concentration of 10^{-8} mol/l and a dissolved sulfur concentration of 10^{-3} mol/l. Modified after Filella et al., 2002b)

2.3 Antimony speciation in hydrothermal fluids

Trivalent antimony form is by far the dominant oxidation state in volcanic and magmatic-hydrothermal fluids (**Spycher and Reed, 1989**). Results from XAFS spectroscopy showed Sb aqueous speciation in ore-forming fluids: Antimony forms the neutral hydroxide species, $\text{Sb}(\text{OH})_3$, in pure water; chloride complexes in concentrated HCl solutions; and mixed Sb-OH-Cl species in NaCl-HCl solutions typical of acidic high-temperature hydrothermal fluids (**Pokrovski et al., 2006**). The role of mixed hydroxyl-chloride complexes in antimony transport by saline high-temperature hydrothermal fluids at acidic conditions has been reported for the first time by **Pokrovski et al. (2006)**. Antimony chloride and hydroxyl-chloride species are more volatile than $\text{Sb}(\text{OH})_3$ (e.g. **Pokrovski et al., 2005b**) and they are expected to preferentially partition into the vapor phase during vapor-brine separation processes occurring in magmatic-hydrothermal systems.

More specifically, thermodynamic calculations by **Prokovski et al. (2006)**, indicated that:

- At moderate temperatures below 300°C and acid ($\text{pH}<3$), Sb(III) speciation in hydrothermal fluids is represented by hydroxyl-chloride species $\text{Sb}(\text{OH})_{3-n}\text{Cl}_n$ with $1<n<3$, and at higher pH by $\text{Sb}(\text{OH})_3$ and $\text{Sb}(\text{OH})_3\text{Cl}^-$ existing in comparable amounts. Antimony hydroxyl-chloride complexes are however minor in the neutral low- to moderate-temperature solutions ($\leq 250\text{--}300^\circ\text{C}$) typical of Sb deposits formation; the antimony speciation in these systems is dominated by $\text{Sb}(\text{OH})_3$ and potentially Sb-sulfide species.
- At higher temperatures, the single $\text{Sb}(\text{OH})_2\text{Cl}$ complex likely becomes the predominant species in acidic fluids ($\text{pH}<4$); it is replaced by $\text{Sb}(\text{OH})_3$ and $\text{Sb}(\text{OH})_3\text{Cl}^-$ in slightly acid to neutral fluids.
- At temperatures above 350°C , the Sb transport is not controlled by solid-phase precipitation in high-temperature saline solutions and this may explain the scarcity of antimony-bearing minerals in high-temperature deposits (**Williams-Jones and Normand, 1997**)

2.4 Antimony in seafloor hydrothermal systems

Overview of seafloor hydrothermal systems

Seafloor hydrothermal systems are one of the most spectacular manifestations of the connection between crustal processes and the deep oceanic system. Scientists discovered hydrothermal vents in 1977, while exploring an oceanic spreading ridge near Galapagos

Islands (**Corliss et al., 1979**). More than 200 vent fields have been documented since the late 1970's (**Kelley et al., 2005**). Most vent fields – 65 per cent – have been found along mid-ocean ridges (**Hannington et al., 2011**), with another 22 per cent occurring in back-arc basins and 12 per cent along submarine volcanic arcs. Very few sites – only 1 per cent – have been observed at intra plate volcanoes. According to **Tivey et al. (2007)**, by comparing the fluids and deposits formed in distinct geologic and tectonic settings, it is possible to examine the role that specific factors play in determining fluid composition (e.g., substrate composition, input of magmatic volatiles, permeability structure of the substrate, geometry and nature of heat source, temperatures and pressures at which reactions occur) and mineral deposit size, shape, and composition (e.g., vent fluid composition, styles of mixing between fluids, longevity of venting). Future progress in understanding the impact that hydrothermal systems have on Earth processes will be made through taking advantage of the observed variability in tectonic and geologic settings of venting. Many of the world's spreading centers have yet to be explored (Fig. 2.4), particularly ultraslow-spreading ridges in the polar regions.

A hydrothermal vent is a fissure in the ocean floor, from which hydrothermal fluid is exhaled. Common land-type hydrothermal vents include hot springs, fumaroles and geysers. Under the sea, the hydrothermal fluids exit through narrow chimneys known as black or white smokers (e.g. **Tivey, 2007**) and diffusers (**Fouquet et al., 1993; Koski et al., 1994**), and **are actively** forming polymetallic massive sulphide deposits. Sea-floor massive sulphides (SMS) deposits form on and below the seabed as a consequence of the interaction of seawater with a heat source (magma) in the sub-sea-floor region (**Hannington et al., 2005**). During this process, cold seawater penetrates through cracks in the sea floor, reaching depths of several kilometers below the sea-floor surface, and is heated to temperatures above 400°C. The heated seawater leaches out metals from the surrounding rock. The chemical reactions that take place in this process result in a fluid that is hot, slightly acidic, reduced, and enriched in dissolved metals and sulphur. Due to the lower density of this evolved seawater, it rises rapidly to the sea floor, where most of it is expelled into the overlying water column as focused flow at chimney vent sites. The dissolved metals precipitate when the fluid mixes with cold seawater. The minerals forming the chimneys and sulphide mounds include iron sulphides, such as pyrite, as well as chalcopyrite and sphalerite (**Hannington et al., 2005**).

Another form of hydrothermal venting is known as “diffuse venting” (**Fouquet et al., 1993; Koski et al., 1994**), where lower temperature (100°C to < 300°C) fluids come out as “shimmering water” which generally do not contain enough dissolved metal and sulfide to form “smoke”. According to **Tivey et al., (2007)**, diffusely venting structures generally emit clear, nearly particle-free fluids. The key difference between diffuse and focused vents is how much mixing with seawater occurs before they are released. The plumbing of diffuse vents is leaky and allows seawater to mix with the vent fluid and this mixture exits the seafloor over a larger area. However, they still contain high levels of hydrogen sulfide and other compounds that specialized microbes can use for energy. These diffusely venting spires likely host unique microbial ecosystems similar to those found to inhabit hydrothermal systems on and beneath the seafloor. Examples of diffusely venting chimneys are the Mothra Hydrothermal Field (MHF) on the Segment of the Juan de Fuca Ridge (Fig. 2.5b) (**Kristall et al., 2006**) and Kolumbo Volcanic field (KVF) in the Hellenic Volcanic Arc (**Kilias et al., 2013**). Diffusely venting structures are formed under evolving conditions in the absence of central throughgoing conduits. The growth of such chimney is facilitated by flow through complex, discontinuous and anastomosing network of tortuous channels and broad regions of diffuse flow through high permeable walls (Fig.2.5 b) (**Kristall et al., 2006**).

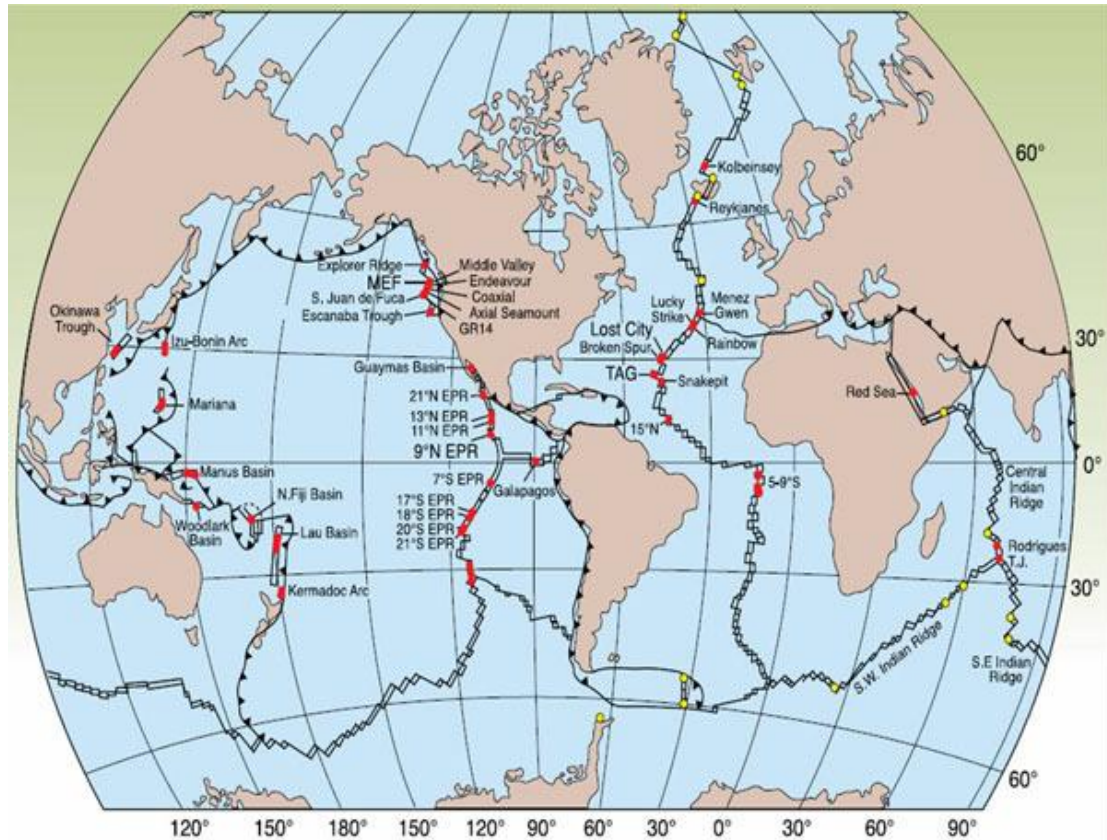


Fig. 2.4 Known sites of hydrothermal venting along mid-ocean ridges, in back-arc basins, rifted arcs, and at submerged island-arc volcanoes (red), and areas of activity as indicated by mid-water chemical anomalies (yellow). EPR= east pacific rise. TAG= transatlantic Geotraverse, MEF = Main endeavour Field, and Gr-14 = Sea cliff hydrothermal field on the northern Gorda ridge. (Figure after Tivey et al., 2007)

The most spectacular kind of hydrothermal vent is called "**black smoker**", where a steady stream of "smoke" gushes from a chimney-like structures (e.g. Tivey, 2007, and references therein). The "smoke" consists of tiny metallic sulphide particles that precipitate out of the hot vent fluid as it mixes with the cold seawater. When the hot fluids exit the seafloor and mix with cold seawater, the dissolved chemicals precipitate instantly into tiny sulfide mineral particles, forming the plumes that we see at black smokers. They spew out mineral rich water filled with iron and sulfide, which combines and forms mainly iron sulfide. Typical smoker vents on volcanic ridge crests have temperatures of 300 to 400°C, with pH values ranging from 2 to 5. Black smokers are examples of focused vents, in which almost all the vent fluid comes out of one small pipe (Fig. 2.5a). Examples of black smokers is the chimney called Finn, recovered the Mothra Hydrothermal Field (MHF) on the Segment of the Juan de Fuca, and chimneys in Brothers Hydrothermal field, Tonga-Kermadec arc (Berkenbosch et al., 2012).

Another form of hydrothermal venting is “white smokers” which are hydrothermal vents that spew out barium, calcium and silicon, which give it its white color. These white smokers are cooler than their higher temperature counterparts, the black smokers. In white smokers, the hydrothermal fluids mix with seawater under the seafloor. When the fluid exits the chimney, the silica precipitates out. Another chemical reaction creates a white mineral called anhydrite. Both of these minerals turn the fluids that exit the chimney white. A white smoker is a hydrothermal vent emitting alkaline high-pH hydrothermal fluid on the ocean floor. These fluids are cooler (~91°C) (Kelley et al., 2005) than those emitted by black smokers (~360 °C) and are located away, or “off-axis”, from the mid-ocean ridges.

Antimony in seafloor hydrothermal fluids

Antimony is among the trace elements that are exported from the lithosphere to the ocean through seafloor hydrothermal systems; underestimated and virtually unstudied input is contributed by submarine hydrothermal fluids discharging at the seafloor at concentrations several hundred times those of seawater (Douville et al., 1999; Fouquet et al., 2010) (see below).

Up to date, very few works report antimony analytical data in seafloor hydrothermal fluids, mostly from deep-water Mid Ocean Ridge (MOR) environments (Douville et al., 1999; Pichler et al., 1999; Fouquet et al., 2010; Mottl et al., 2011); Sb concentrations of shallow (5–10 m) submarine hydrothermal fluids have only been reported once (Pichler and Veizer, 1999). Reported measurements of antimony reveal concentrations of <3–11(nM) in Mid-Atlantic Ridge (MAR) (Fouquet et al., 2010), <3–17(nM) in East Pacific Rise, <3–188(nM) in back-arc basins (Douville et al., 1999), 100–1,300 (nM) in Oceanic island arc-Tutum Bay (Pichler et al., 1999) and 28 nM in Eastern Lau Basin (Mottl et al., 2011). Reported measurements of antimony with maximum concentrations of 28 nmol/kg were mistakenly measured on unacidified samples, and probably do not represent the real concentrations in the vents because of precipitation subsequent to collection (Mottl et al., 2011).

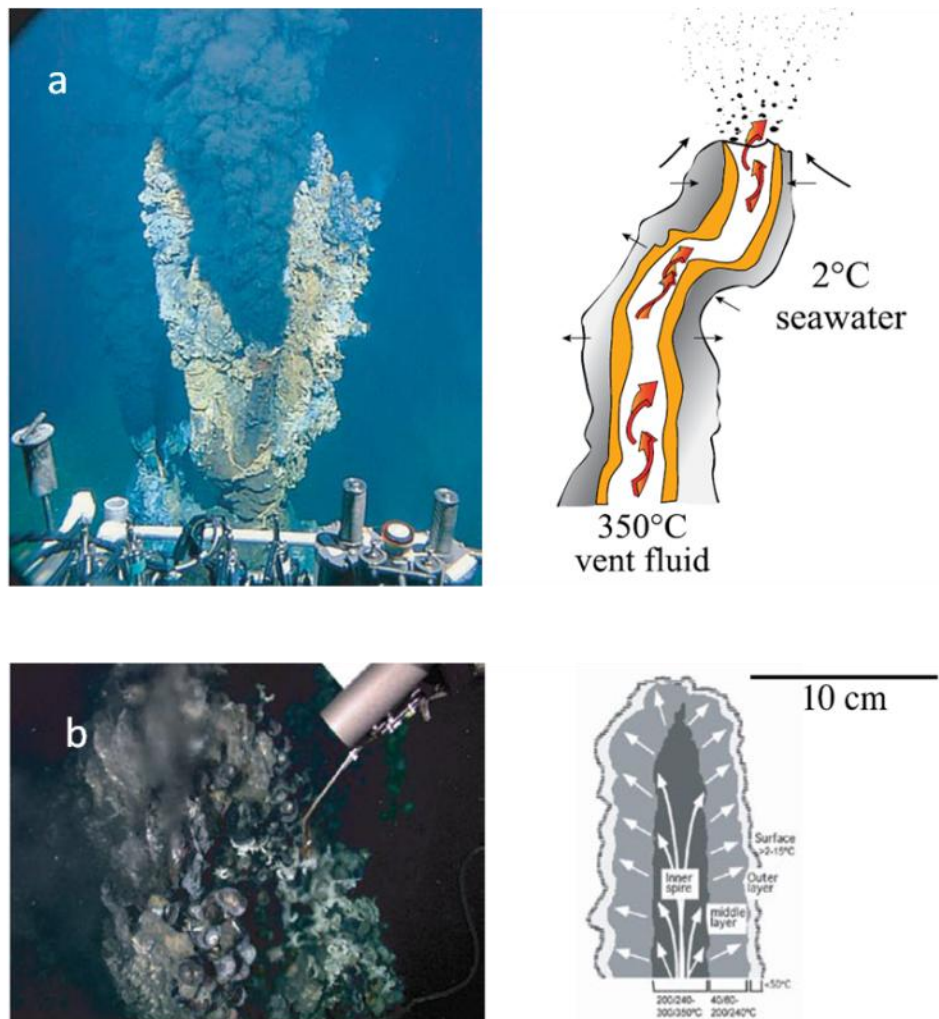


Fig.2.5 (a) Photograph of a black smoker chimney from the southern East Pacific Rise, taken from the submersible *Alvin* on Dive 3296 (courtesy of Woods Hole Oceanographic Institution (WHOI); M. Lilley and K. Von Damm chief scientists) and a schematic drawing showing cross section of a black smoker chimney with one small pipe with slower advection and diffusion occurring across the walls. (b) Photograph of a 284°C diffusely venting spire from the Vienna Woods vent field in the Manus Basin taken on *Jason* Dive 207 (courtesy of WHOI; M. Tivey chief scientist), and a schematic drawing of the cross section across an East Pacific Rise diffusely venting spire that is composed of an inner, very porous zone of pyrrhotite (Fe_{1-x}S), wurtzite (Zn,FeS), and cubanite (CuFe_2S_3); a less-porous mid layer of wurtzite, pyrite (FeS_2) and chalcopyrite (CuFeS_2); and an outer layer of marcasite (FeS_2) (after Tivey et al., 2007)

Antimony in hydrothermal solid phases

The modes of antimony occurrence in seafloor hydrothermal solids of different seafloor hydrothermal fields have reported in mid-ocean ridge environment, back arc basins and island arcs.

Mid-ocean ridge environment:

(1) **Koski et al. (1988)** have identified traces of Pb-Sb sulfosalts with ~ 2 wt.% Zn (+As, Ag) corresponding to the mineral formulas $(\text{Pb,Zn})_5\text{Sb}_4\text{S}$ (boulangerite) and $(\text{Pb,Zn})_{10}\text{Sb}_6\text{S}_{19}$ (Zn-boulangerite) in massive sulfides from the Escanaba Trough, the sediment-covered southern end of Gorda Ridge spreading axis. Two polymetallic sulfide samples have very high bulk Sb (2,700; 1,000; 960; 8,700; 16,000 ppm)(+Pb, As, Se, Ag) contents. Pb, As, and Sb concentrations of this magnitude have not been reported for bulk samples from any mid-ocean ridge. In addition arsenopyrite containing 0.11-0.18 wt% Sb and lollingite with 0.20-0.33 wt% Sb were also reported.

(2) **Hannington et al. (1986)** identified Pb-As-Sb-Ag sulfosalts in low-temperature zones of sulfide mounds and spires from Axial Seamount (Juan de Fuca Ridge) and the southern Explorer Ridge.

(3) **Fouquet et al. (2010)** have identified traces of Tetrahedrite $[(\text{Cu,Fe})_{12}\text{Sb}_4\text{S}_{13}]$ in ultramafic-hosted sulfide mineralization along the Mid-Atlantic Ridge (MAR), {Tetrahedrite-Tennantite $(\text{Cu,Fe})_{12}(\text{Sb,As})_4\text{S}_{13}$ }.

Back-arc basins:

(1) Traces of stibnite (Sb_2S_3), and enargite (Sb: 0.24 wt%), and tennantite (Sb: 3.38 wt%) were reported from Yonaguni IV hydrothermal field, Okinawa Trough Back-Arc Basin (**Suzuki et al. 2008**).

(2) Orpiment with 0.05 wt% Sb was reported from Kaia Natai Seamount, PNG: (**Dekov et al., 2013**); (3) Traces of tetrahedrite $(\text{Cu,Fe})_{12}(\text{Sb})_4\text{S}_{13}$ were detected in JADE site of Izena Cauldron in the central Okinawa Trough (**Nakashima et al., 1995**).

Island arcs:

(1) Traces of possible Sb-bearing jordanite $(\text{Pb}_{14}(\text{As, Sb})_6\text{S}_2)$ have been reported from Brothers submarine volcano, Kermadec arc, New Zealand (**Berkenbosch et al., 2012**);

(2) Polymetallic veins with minor Cu-Pb-As-Sb sulfosalts (tetrahedrite, tennantite, jordanite), minor stibnite (Sb_2S_3), colloform sulfosalts with a highly variable mineral chemistry i.e., Fe, Pb, As, Sb, Hg, Ag; [Sb:0.91-9.22 wt %]) and an unknown Fe-As-Sb sulfide($(\text{As}_{0.80}\text{Sb}_{0.15}\text{Fe}_{1.08}\text{S}_3)$) intergrown with sphalerite, chalcopyrite, and amorphous silica, have been reported from Conical Seamount, New Ireland fore-arc, PNG (**Petersen et al., 2002**); as well as orpiment (As_2S_3) with 0.14 wt % antimony and realgar (As_4S_4) with 0.63 wt % Sb (**Dekov et al., 2013**),

(3) Thallian arsenian pyrite with antimony (up to 15 wt%) occurs in crusts of ore minerals from shallow (< 100 m--some tens of meters) submarine hydrothermal vent field of Dominica Island, Lesser Antilles (**de Roche et al., 2012**).

2.5 Speciation and incorporation of antimony into natural Fe-(oxy)hydroxides

The structural incorporation of cations into various Fe-(oxy)hydroxides has been reported for a number of cations: Me(II) (NiII, ZnII, CuII, CoII, MnII, and CdII), Me(III) (AlIII, CrIII, MnIII, RhIII, GaIII, InIII, NdIII, ScIII, CoIII, and VIII), Me(IV) (PbIV, GeIV, SnIV, SiIV, TiIV, and CeIV), and Me(V) (PV and AsV) (**Cornell et al., 2003; Voegelin, et al., 2010; Galvez et al., 1999**). **Mitsunobu et al. (2010)** studied first the structural incorporation of Sb(V) into the Fe(III) site of iron oxides. It was found that Sb(V) can be incorporated into the structure of the ferrihydrite and goethite by substitution during formation of the solids. Sb(V) incorporated into the structure is not greatly influenced by factors such as the pH, ionic strength, and concentration of competitive ions, because antimony species coprecipitated in the solid structure are mostly unavailable to the aqueous phase. Therefore, this is an important finding to predict Sb(V) behavior in aquatic environments under oxic conditions.

Mitsunobu et al. (2013) studied the the behavior of Sb(V) during transformation of poorly crystalline Fe(III) oxyhydroxides, i.e. two-line Ferrihydrite; it was proved that goethite and hematite are the primary transformation products of the ferrihydrite in the presence of Sb(V) that does not influence the transformation. Moreover, Sb(V) is structurally incorporated into crystalline goethite and/or hematite generated by the ferrihydrite transformation. As a result, the transformation products may serve as a reliable sink for long-term immobilization of Sb(V) and this finding is valuable for making predictions on the fate of Sb associated with ferrihydrite in natural environments.

2.6 Speciation and incorporation of antimony in pyrite

Pyrite commonly contains a range of trace elements, including Ag, As, Au, Bi, Cd, Co, Cu, Hg, Mo, Ni, Pb, Pd, Ru, Sb, Se, Sn, Te, Tl, and Zn (**Abraitis et al., 2004**). Among these elements, As, Co, Ni, Sb and, possibly, Cu, Ag, Au, and Sn can be efficiently incorporated in the pyrite structure (**Reich et al., 2013; Deditius et al., 2011**). Pyrite may play a significant role as a scavenger of precious metals and metalloids (i.e. Au, Ag, Ni, Pb, Bi, As, Sb, Cu, Te) in hydrothermal systems; this may reflect true substitution into the pyrite structure or

coexistence of metals in closely adjacent micro- and/or nano-sized mineral particles (**Reich et al., 2011, 2006; Deditius et al., 2011**).

Studies of trace element zoning in pyrite have been conducted in various geologic settings, i.e. (i) Carlin-type precious metal deposits (Lone Tree, Screamer, Deep Star (Nevada, USA) (**Deditius et al., 2011**), (ii) high-sulfidation epithermal Au-Ag-Cu systems (Pueblo Viejo (Dominican Republic), Yannacocha (Peru), and Porgera (Papua New-Guinea) (**Deditius et al., 2009; 2011**), (iii) Au-(U)-bearing conglomerates (Witwatersrand, South Africa; Pardo and Clement Townships, Ontario, Canada)(**Ulrich et al., 2011; Agangi et al., 2012**), (iv) porphyry Cu systems (Dexing porphyry, China)(**Reich et al., 2013**) and, (v) Seafloor hydrothermal vent fields (Dominica Island, Lesser Antilles) (**de Roche et al., 2012**); Semenov-1 hydrothermal field (Mid-Atlantic Ridge, 13°30.87' N) (**Meleketseva et al., 2014**). It has been reported that marcasite-pyrite from Semenov-1 is enriched in Sb (0.71-15 ppm) as well as V, Mn, As, Mo, Au, Hg, and Tl. Except for two recently published cases (**de Roche et al., 2012., Meleketseva et al., 2014**) there is a lack of published data on the concentration and speciation of Sb in amorphous and/or crystalline Fe-sulfides from active seafloor hydrothermal fields, unless stibnite is formed (**Deditius et al., 2011**), It should be emphasized that, trace metal zoning studies of concentrically laminated pyrite have been very rare, and to our knowledge limited to a single case of Au-(U)-rich conglomerates (Witwatersrand, S. Africa) (**Agangi et al., 2013**).

2.7 Antimony in organisms -Bioaccumulation

Organisms are exposed to antimony through air, water, and food sources. The exposure to antimony and its daily intake to organisms is usually not a health concern, because the concentrations in surrounding air and air particle matter, drinking water, and food are usually very low (**Belzile et al., 2011**). Not all of antimony that enters the human body is bioavailable, since the assimilation strongly depends on speciation (**Newman et al., 1994**) and the size of particles (**Belzile et al., 2011**), for which there not enough data so more systematic studies are needed. The bioaccumulation behavior of antimony reflects its bioavailability to organisms and its believed that it maybe be similar to that of As and may be comparatively predicted (**Filella et al., 2007**).The bioavailability of antimony is generally lower than of As (**e.g Telford et al., 2009**).

Some studies were conducted on the bioaccumulation behavior of Sb in a large Sb mining/smelting area in Hunan, China (Xikuangshan(XKS) Sb mine), which had been severely polluted by antimony (**Liu et al., 2010; Fu et al., 2010; Feng et al., 2010. Liu et al. (2010)**

found that elevated levels of Sb as well as As were present in hair from children and adults who live in the vicinity of the XKS antimony mine. **Fu et al. (2010)** showed evidence of bioaccumulation of Sb in fish, amphibians and invertebrate organisms in the vicinity of the XKS mine. Antimony concentrations in terrestrial invertebrates were higher than those in aquatic and amphibious species. **Feng et al. (2010)** found that Sb is accumulated in rice grown in contaminated fields. Seedlings of paddy rice were exposed to 5 mg L^{-1} Sb ($\text{KSbC}_4\text{H}_4\text{O}_7 \cdot \frac{1}{2} \text{H}_2\text{O}$) and highest Sb contents measured among all treatments in this experiment in the leaves, stems and roots were 65.5, 298.5 and 195.7 mg kg^{-1} , respectively. **Duester et al., (2011)** reported high phytotoxicity of trimethylantimony (V) [TMSb(V)] on aquatic floating water plants. **Qi et al. (2011)** described several species of wild plants that accumulate elevated Sb concentrations, especially in their above-ground parts such as shoot, leaf, and flower.

Some studies were conducted on the mechanisms of Sb uptake by bacteria. It has recently been proved that an integral membrane protein (aquaglyceroporins) is involved in Sb^{3+} uptake by *Escherichia coli*, *Saccharomyces cerevisiae*, *Leishmania major* and *Leishmania tarentolae* (**Filella et al., 2007**). It is reasonable to assume that similar mechanism may be active in other organisms too. Since aquaglyceroporins mediate the transport of neutral molecules, it is not surprising that they facilitate the uptake of the neutral $\text{Sb}(\text{OH})_3$ molecule. The penetration mechanism of Sb^{5+} in the organisms mentioned is still unknown.

3. Antimony in the unique shallow-submarine volcano, Kolumbo (Santorini), Hellenic Volcanic Arc (HVA).

3.1 Geodynamic and geological setting of the HVA

The Hellenic Subduction System (HSS) represents a unique situation in convergent settings, different from Pacific geodynamic settings (**see Kiliyas et al., 2013 and references therein**). The difference is that the 5 Ma-to-present Hellenic Volcanic Arc (HVA) (Methana, Milos, Santorini, Nisyros, Fig. 3.1) (**Papanikolaou, 1993; Royden et al., 2011**) where volcanism and hydrothermal activity occur through thinned continental crust due to extensional regime, is separated from the Hellenic Sedimentary Arc (HSA) (Peloponnesus, Crete, Rhodes) by the Cretan basin, a “back arc” molassic basin (Middle-Late Miocene-Quaternary age), which lies behind HSA but in front of the HVA (Fig. 3.2). The Cretan Basin is the result of extension north of Crete, whereas the Hellenic trench and fore arc basin of the HSS south of Crete is dominated by compression. The draping of the slab over the 660-km discontinuity resulted in accelerated slab retreat and it provides a cause for ~300 km of extension and the ensuing opening of the Aegean Sea basin (**Ring et al., 2010**).

Volcanic activity along the Hellenic Volcanic Arc has started in the Pleistocene and has continued during the Holocene in the main volcanic centers: Methana-Poros, Milos, Santorini, Kos, Nisyros (**Fytikas et al., 1984**). Submarine volcanic centers have been discovered in the Epidavros Basin, in the Anyhdros basin northeast of Santorini, which includes the Kolumbo submarine volcano (**Alexandri et al., 2003**) and around Nisyros (**Papanikolaou et al., 2001; Nomikou et al., 2004**).

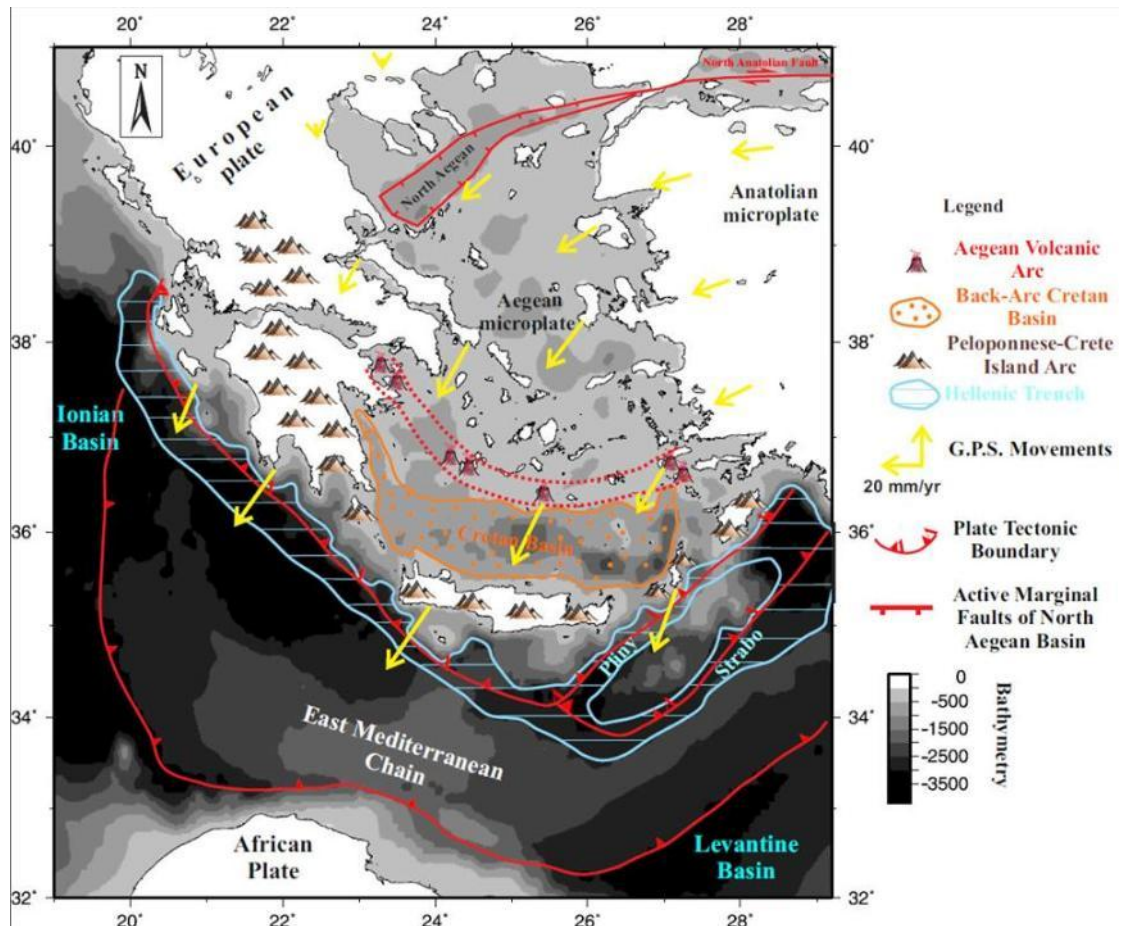


Fig. 3.1 Location of Kolumbo submarine volcano within the Hellenic volcanic (Nomikou et al., 2013).

3.2 The Kolumbo submarine volcano and hydrothermal system

Kolumbo is a submarine volcano of the HVA, located about 7 km off the north-eastern coast of Thera (Santorini) in the Aegean Sea along a northeast-southwest-trending linear volcano-tectonic field that extends for 20 km (Fig. 1.7, 1.8) (Nomikou, et al., 2012). Kolumbo was believed to have formed during a single eruptive phase in 1650 AD (Fytikas et al., 1990) when an explosive eruption produced about 2 km³ of magma across the sea surface that caused 70 deaths on Thera from toxic gases (Dominey-Howes et al., 2000). Seismic reflection profiles revealed two cone-like volcanoclastic deposits, which indicate that the Kolumbo volcano evolved from at least two eruptions (Huebscher et al., 2006). Other areas of volcanism surrounding Santorini include the Christianna islands, around 20km to the southwest, and the 19 submarine volcanic cones of varying sizes which extend

20 km to the northeast of the main island of Thera, within the Anyhdros sedimentary basin (**Alexandri et al., 2003; Nomikou, et al., 2012**)(Fig. 3.3). According to **Nomikou et al. (2013)** Kolumbo volcanism, tectonism and hydrothermal activity, and the Santorini 2011-2012 both seismic and geodetic unrest, occurred along a NE-SW tectonic zone named as Christianna-Santorini-Kolumbo (CSK) line (Fig. 3.4).

The Kolumbo submarine volcano is built on pre-Alpine continental basement of Cyclades (10-15 km thick) (Fig. 3.2 f). As magma rises through the Aegean lithosphere, which is very thin due to the extensional regime, it crosses the pre-Alpine continental crust component, approximately 10-15km thick. This includes a core of carboniferous granites (ortho-gneisses) and a mantle of garnet-mica schists (**Van der Amar et al., 1983**) corresponding to the Palaeozoic Metamorphic Basement cropping out on los island (**Fortster et al., 1999**). Then it crosscuts various Alpine units including: (i) Mesozoic metamorphic rocks with HP/LT Tertiary metamorphism (Athinos/ los blueshists) (1) ,(ii) non metamorphic Mesozoic carbonates and Tertiary flysch (Proph. Ilias/Anafi autochthon) (2) and (iii) Late Cretaceous allochtonon metamorphic units (Anafi greenschists and granites) (3, 4, 5)(Fig. 1.7f)(**Kilias et al., 2013a**).The Mesozoic Carbonates and Tertiary flysch (2) revealed at the SE part of Santorini continue towards the south and southeast and re-appear at the basal unit of Anafi Island (**Kilias et a., 2003a**).

The Kolumbo submarine volcano is built on pre-Alpine continental basement of Cyclades (10-15 km thick) (Fig. 3.2) (**Kilias et al.,2013a**).The Kolumbo crater walls reveal stratified pumiceous deposits at a depth of 270-250 m which continue to 150 m, above which the deposits are covered by loose talus and bacterial overgrowths (**Cantner et al., 2013; Nomikou et al., 2003**). Analyzed pumice from Kolumbo crater walls, is largely high-K rhyolite (73.7 to 74.2 wt% SiO₂, and 3.85 to 3.94 K₂O; 4 analyses) with a high pre-eruption volatile content of 6-7 % (**Sigurdsson et al., 2006**). The eastern crater walls reveal some massive lava flows with impressive columnar jointing and isolated NE-SW trending dikes parallel to the CSK (**Nomikou et al., 2012; Cantner et al., 2010**).This linear contribution of the volcanic cones is controlled by the NE-SW Christiana-Santorini-Kolumbo (CSK) volcano-tectonic zone which provides pathways for subduction-generated magmas to reach the surface (Fig. 3.4) (**Nomikou et al., 2012, 2014**).

Kolumbo is the largest volcano of the Christiana-Santorini-Kolumbo (CSK) volcano-tectonic zone, and its elongated cone has a basal diameter of 7 km, a crater width of 1.7 km and rises up from at least 504 m to 18 m (**Carey et al. 2011**). Data of Kolumbo volcano was

collected during 4 marine geological surveys using the E/V Nautilus, R/V Aegaeo and R/V Endeavor conducted northeast of Santorini island. First, swath bathymetry of the study area was conducted in 2001 using the 20 kHz SEABEAM 2120 swath system on R/V Aegaeo. Detailed swath bathymetry carried out in 2001 and 2006 revealed the existence of at least nineteen small submarine volcanic cones NE of Santorini within Anyhdros sedimentary basin (**Nomikou et al., 2004**). The second survey took place in the northern part of Kolumbo's crater floor in 2006 onboard R/V Aegaeo and R/V Endeavor and included complementary swath bathymetry data that refined the existing map, airgun 10ci single channel seismic profiling, gravity and box coring, and ROV dives. During the second marine survey of 2006 an extensive "diffuse-flow"-style hydrothermal vent field, Kolumbo Hydrothermal Field (KHF), was discovered inside the crater (**Sigurdsson et al., 2006**). In 2010 and 2011, onboard E/V Nautilus gas and geological samples were collected (**Carey et al., 2011**), bathymetric map of KHF was created (Fig.3.3) with the ROV Hercules and the 1,375 kHz Blue View multibeam sonar, and structured light and stereo imagery was also carried out (**Roman et al., 2012**).

The entire crater floor of Kolumbo (area of approximately 600 x 1200 m) is covered by a few-cm-thick orange to brown smooth sediment (**Carey et al., 2011**), that consists of Fe-encrusted flocculent microbial mats and amorphous Fe-oxyhydroxide deposits with temperature varies between 16.2C and 17 °C (**Kilias et al., 2013**). The hydrothermal fluids and CO₂ gas bubbles, which discharge from the Fe-microbial mats through small pockmark-like craters,(Fig 3.5a) have low-temperature (<70 °C). This "diffuse flow" may be supporting microbiological productivity in Kolumbo's crater floor and therefore the Fe-mat formation (**Kilias et al., 2013**). The margins of the crater wall in the northeast have streams of white microbial mats (**Kilias et al., 2013**).

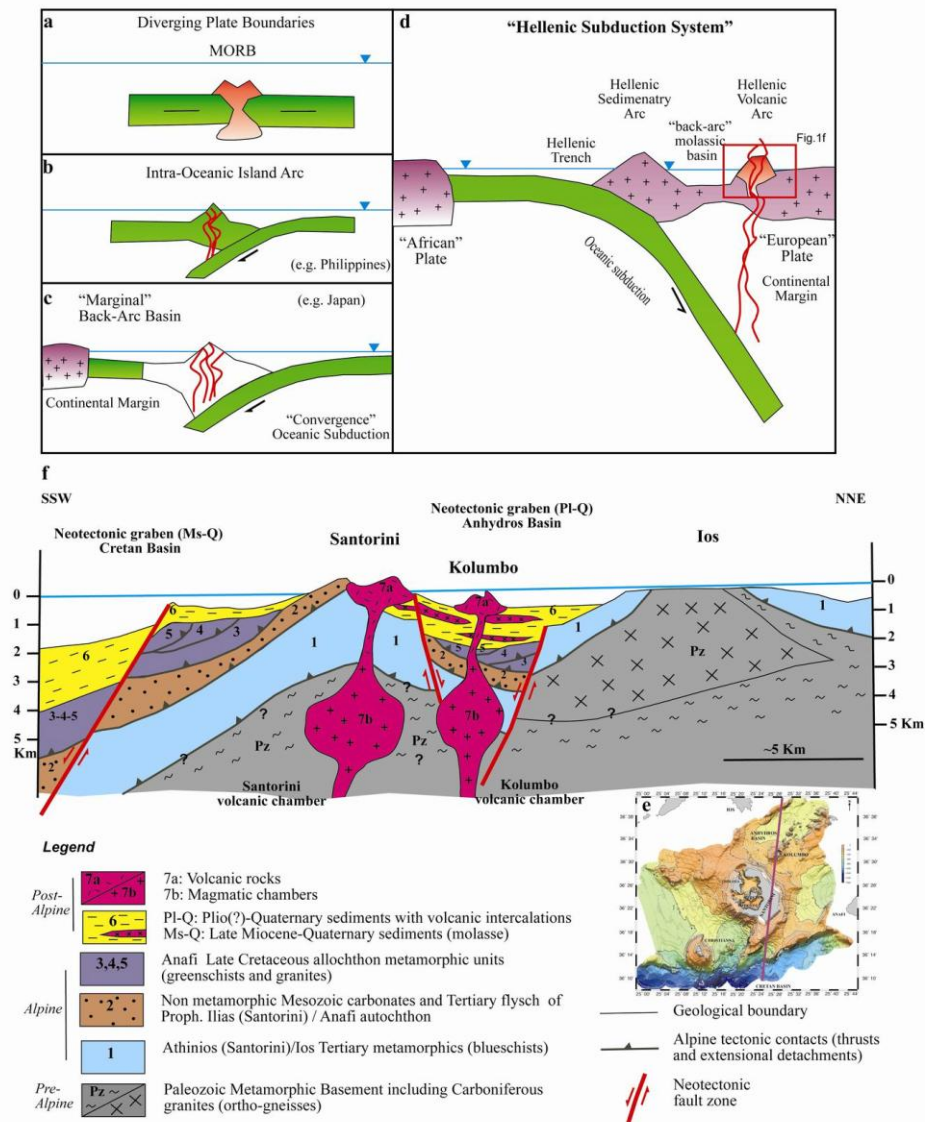


Fig.3.2 Geodynamic setting of the Santorini-Kolumbo volcanic field (a-d): Schematic cartoons of different geodynamic environments where seafloor hydrothermal vents occur. (a) Mid-Ocean ridges along divergent plates, (b) Intra-Oceanic Arcs within convergent boundaries (e.g. Philippines). (c) Marginal back-arc basins and island arcs along active continental margins with oceanic subduction (e.g. Japan), (d) "Hellenic Subduction System", within active continental margin, developed behind the molassic back arc basin, hosted over thinned continental crust. (e) Swath bathymetry map of Santorini Volcano volcanic field. (f) Schematic cartoon of the geological cross section through the Hellenic Volcanic Arc, from the molassic back-arc Cretan Basin to the Cycladic island of Ios in the basic-arc area (Kilias et al., 2013).

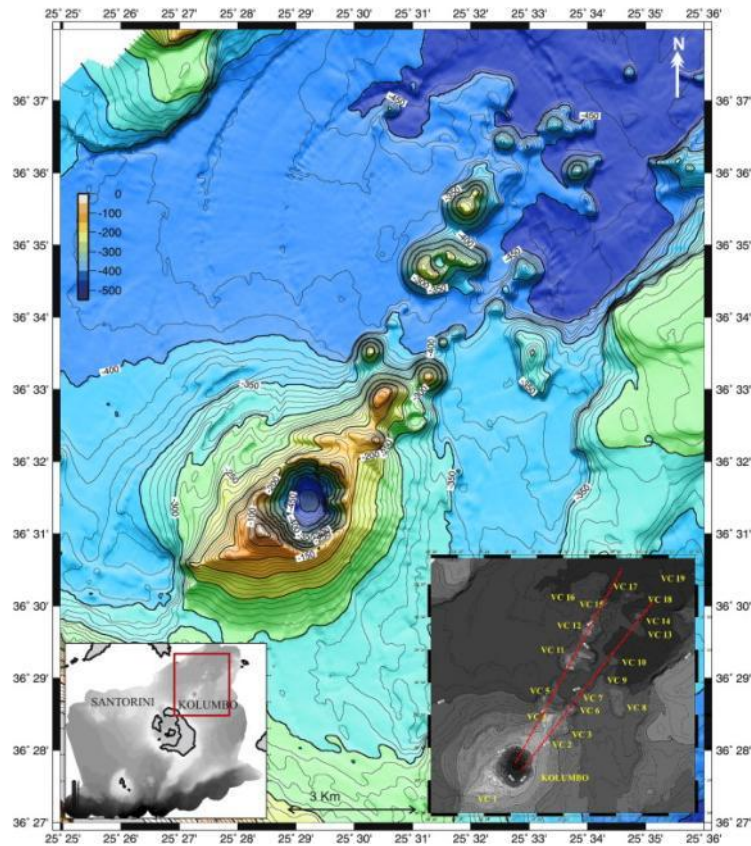


Fig.3.3 Swath bathymetric map of the submarine Kolumbo volcanic chain using 10m isobaths. Right inset: Bathymetric map reciting the 19 volcanic domes in two NE-SW trending lines. Left inset: Geographical index map (Nomikou et al., 2012)

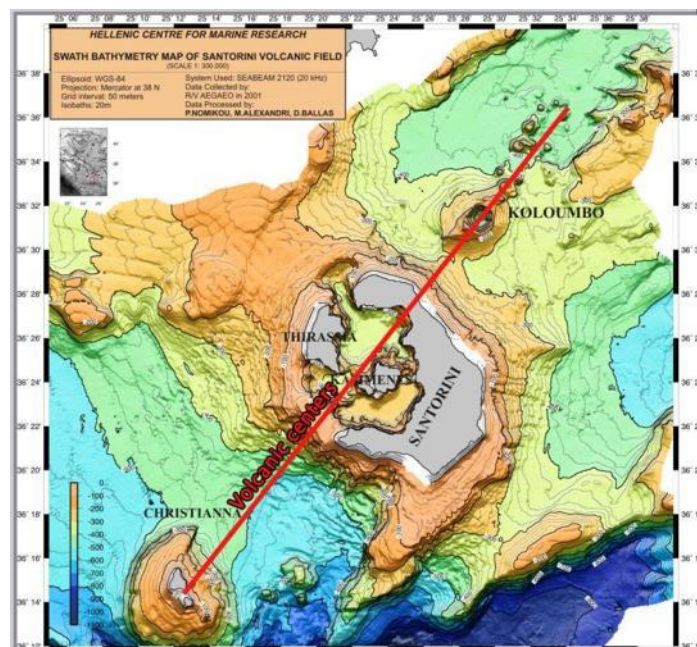


Fig.3.4 Swath bathymetry map of Christianna-Santorini-Kolumbo volcanic field (CSK) and tectonic zone (red line) (Nomikou et al., 2012).

The following description of the Kolumbo hydrothermal vents is synthesized from **Sigurdsson et al. (2006), Carey et al. (2013) and Kiliyas et al. (2013)**.

In the widespread hydrothermal vent field was observed active and inactive sulphide-sulphate structures in the form of vertical spires and pinnacles, mounds and flanges along a NE-SW trend, sub-parallel to the CSK volcano-tectonic zone (Fig.3.4). These vents are surrounded by sites of low temperature (<70C) diffuse venting from the Fe-mats. There are many short (<3 m tall), slender, intermediate-temperature diffusely-venting, isolated and/or merged, sulphide-sulphate spires or “diffusers”. These spires usually taper to their top, and rise up from a hydrothermal mound that grows directly on the sediment and Fe mat-covered seafloor. A typical spire-type vent, named Politeia Vent Complex, covers an area of 5x5 m (Fig 3.5b) in the western part of KHF (Fig.3.5). Diffusely venting structures generally emit clear, nearly particle free-fluids. Similar vents have been observed at shallow-water boiling vents on the Tonga arc, SW Pacific, the Juan de Fuca Ridge, and the Mid-Atlantic Ridge near Iceland. The exterior of the Politeia spires is covered by grayish suspended filamentous microbial biofilms (streamers) that could not be recovered (Fig.3.5b).

In the central part of the vent field are smooth-sided sulphide sulphate mounds with no spire structures such as the Champagne Vent Complex (“Champagne”) and the Diffuser II Vent Complex (“Diffuser II”) (Fig.3.5 c, d) that are covered by orange to brown Fe-rich microbial mats (**Kiliyas et al., 2013**). They commonly discharge streams of bubbles, mainly CO₂, from small holes and cracks on their sides and bases. The dissolution of the gas causes accumulation of stably-stratified CO₂-rich water within the enclosed basin of the Kolumbo crater, and the accumulation of acidic seawater above the vents (pH 5.0) (**Carey et al., 2013**). At the northern crater slope is located the largest observed hydrothermal vent Poet’s Candle (height , 4 m) with Fe microbial mat covering. It’s an inactive vent with no clear evidence of shimmering fluids (Fig. 3.5e).The highest vent temperature that was measured in 2010 was 210C.

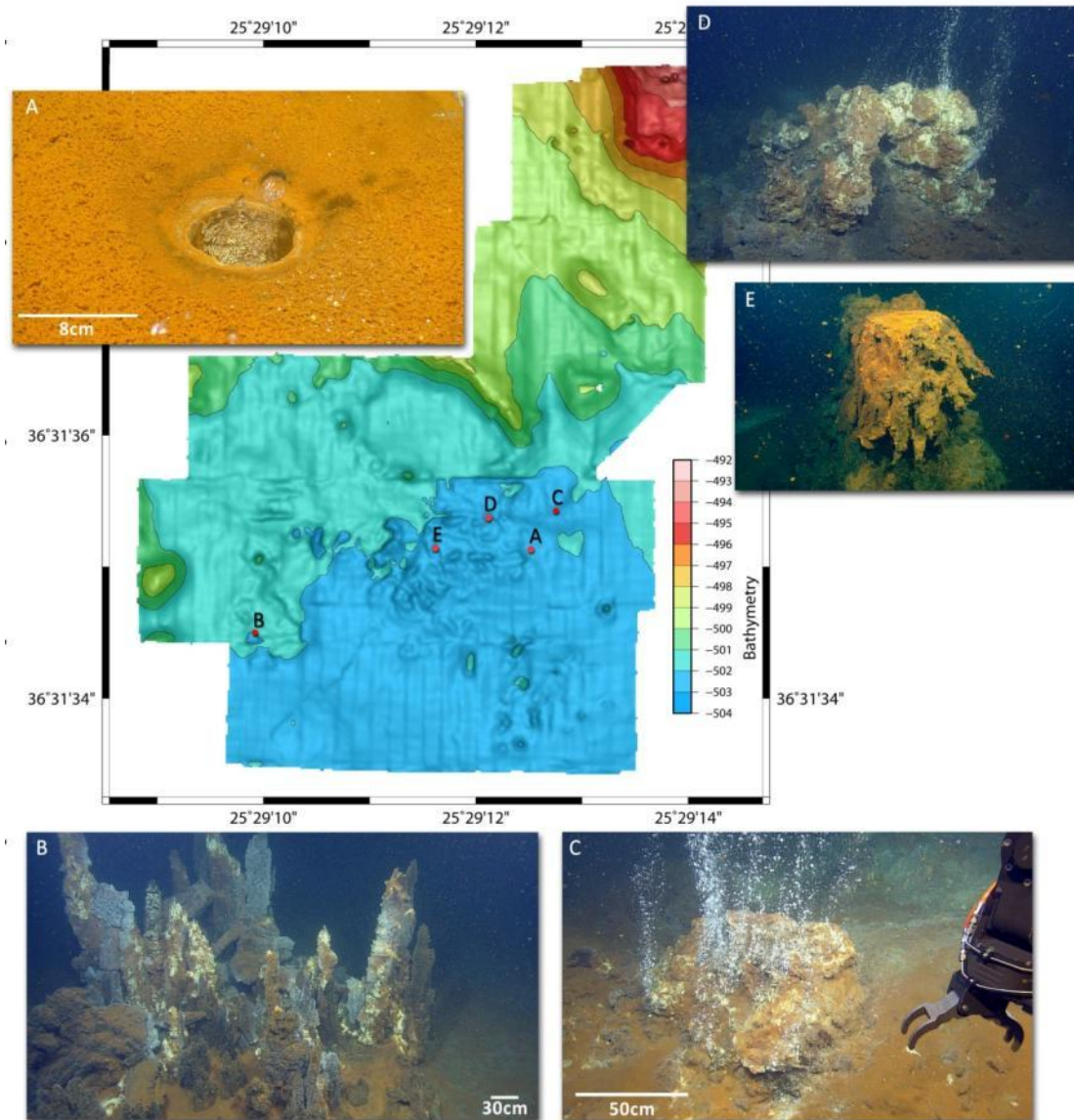


Fig. 3.5 Detailed bathymetric map of Kolumbo hydrothermal vent field using 0,5m grid interval created with the ROV Hercules and the 1,375 kHz Blue View multibeam sonar in the northern part of the crater floor. The more active vents are located in the southern part and the larger, less-active vents in the northern part of the crater floor (red square in a).The location of hydrothermal vents, Politeia, Champagne, Diffuser II and Poet's Candle are and small pockmark-like crater indicated by red dots.

A: Small pockmark-like crater discharging low-temperature fluids through the Fe-bacterial mats that covered the entire crater floor of Kolumbo. **B:** "Politeia Vent Complex": Field of multiple inactive and active sulphide/sulphate spires ~ 2 m high on top of a hydrothermal mound, draped by Fe bacterial mats. Clear fluids vent from active spires (not visible) **C:** "Champagne Vent Complex": Active high-temperature (220°C) vent discharging both gases (>99 % CO₂) and fluids. **D:** "Diffuser II Vent Complex" with Fe bacterial covering and gas bubbling. **E:** "Poet's Candle": The largest observed (height ~ 4 m) inactive vent with bacterial covering (Kilias et al., 2013).

3.3 Antimony enrichment in Kolumbo, central HVA

The active hydrothermal submarine and subaerial systems of Santorini and Milos represent the most important hydrothermal centers of the Hellenic Volcanic Arc (**Varnavas and Cronan., 2005**). A regional study of the geochemistry of sediments from the central Hellenic Volcanic Arc showed that they are mainly composed of biogenic and detrital volcanoclastic and terrigenous phases (**Hodkinson et al., 1994**). The influence of volcanically derived hydrothermal components in the sediments of the region is limited compared to local hydrothermal enrichments of some elements near the vents in the vicinity of Santorini and Milos (**Varnavas et al., 2005**).

According to **Varnavas et al. (2005)**, hydrothermal waters and associated sediments of the Santorini hydrothermal field are enriched chiefly in Fe, Mn and As (Fig. 3.6). Sediment cores recovered from Palaea Kameni consist mainly of pyrite, diatoms and amorphous iron hydroxides. The Nea Kameni sediments consist mainly of amorphous Fe oxyhydroxides with substantial amounts of Si, S and Na and minor amounts of Zn, P, As and organic C. The geochemical spidergram illustrated in Figure 3.7 depicts enrichment in As and Zn in Kos-Yali sediments, Methana sediments, and Milos and Santorini (Palaia and Nea Kameni) metalliferous sediments (**Kilias et al., 2014; Gamaletsos et al., 2013**). For reasons yet unclear Kolumbo polymetallic chimneys (see below) located in the central HVA are uniquely enriched in Sb (avg.: 8,330 ppm; max: 2.2 wt%) as well as Tl (avg.:510 ppm; max: 1,000 ppm)(Fig. 3.8, 3.9); these values are among the highest reported from modern seafloor hydrothermal systems (**Kilias et al., 2013**). Moreover, the same samples show epithermal geochemical association and enrichment (Au, As, Sb, Hg, Ag, Tl, Ag) (Fig. 3.9).

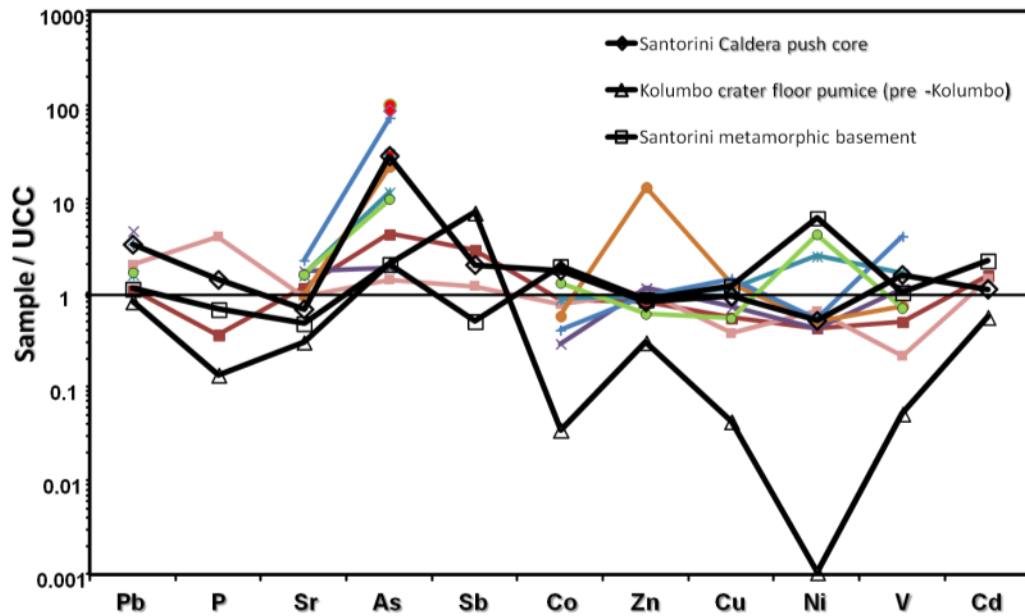


Fig.3.6 Geochemical spidergram of selected trace metals from Kolumbo (see below) crater pumice, Santorini metamorphic basement and Santorini caldera bottom sediments (push core) (Kiliyas et al., 2014; Godelitsas et al., 2013)*. Concentrations are normalized to Upper Continental Crust (UCC) Rudnick et al., 2003).

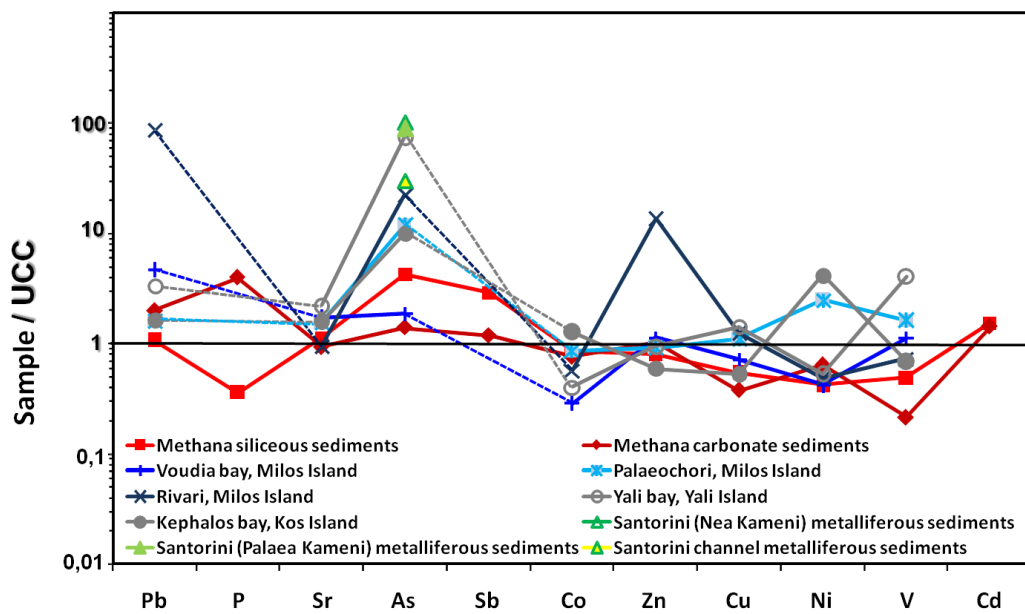


Fig.3.7 Geochemical spidergram of selected trace metals from Kos-Yali sediments, Methana sediments, and Milos and Santorini (Palaia and Nea Kameni) metalliferous sediments (Kiliyas et al., 2014; Godelitsas et al., 2013). Concentrations are normalized to Upper Continental Crust (UCC) (Rudnick et al., 2003).

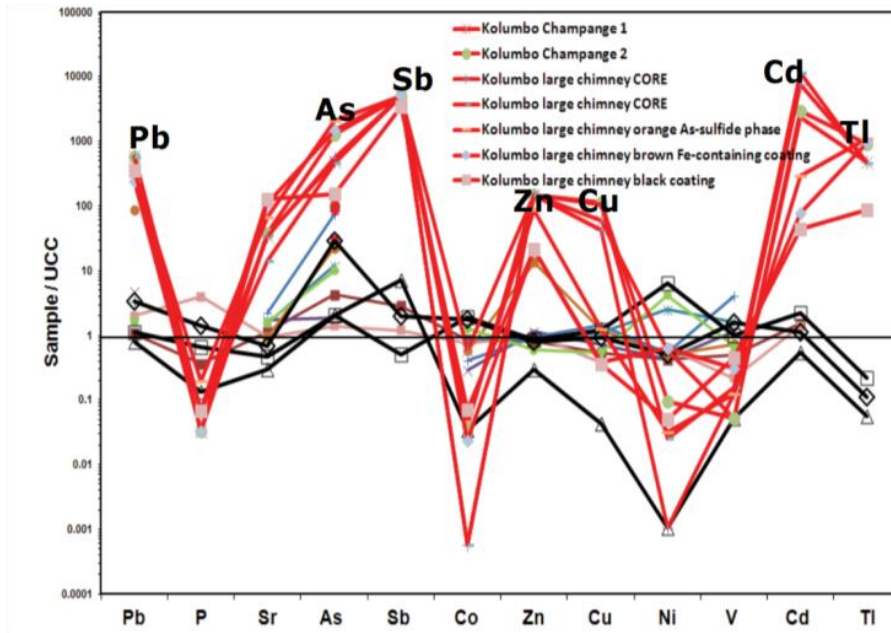


Fig.3.8 Geochemical spidergram comparing the investigations of Kolumbo polymetallic chimneys, with marine sediments of Hellenic Volcanic arc (Santorini, Milos, Methana). Concentrations are normalized to Upper Continental Crust (UCC) (Rudnick et al., 2003). Unique enrichment of polymetallic chimneys of Kolumbo: Tl (avg.:510 ppm; max: 1,000 ppm) and Sb (avg.: 8,330 ppm; max: 2.2 wt%) are among the highest reported from modern seafloor hydrothermal systems. Data from: Gamaletsos et al. (2013); Kiliyas et al. (2013).

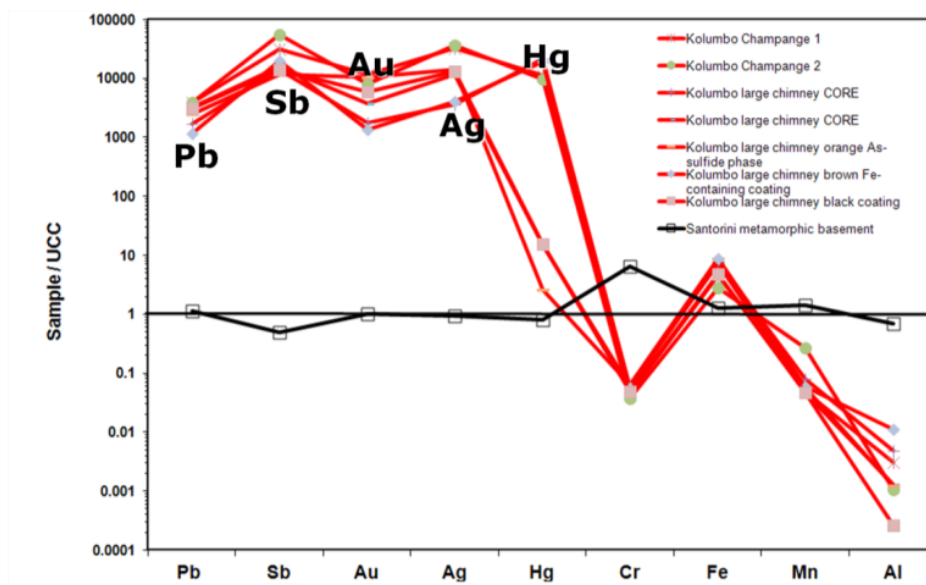


Fig.3.9 Geochemical spidergram of selected trace metals from Kolumbo polymetallic chimneys, Santorini metamorphic basement and Santorini caldera push core. Concentrations are normalized to Upper Continental Crust (UCC) (Rudnick et al., 2003). Au: 32 ppm, Ag: 1,913 ppm, Pb: 6.7 wt %, Sb: 2.2 wt %. “Epithermal suite of elements” enrichment Au, As, Sb, Hg, Ag, Tl on the seafloor (Kiliyas et al., 2013).

4. Scope of thesis

This study aims to contribute to a better understanding of the mechanisms of concentration and cycling of Sb in seafloor hydrothermal systems, and thus fill the knowledge gap of the biogeochemical cycling and fate of Sb that is released into the ocean water through submarine hydrothermal venting.

Towards this scope, the main objectives dealt with here are:

- to study pyrite zoning as a record of antimony mineralization and environmental cycling.
- to study atomic scale antimony speciation in pyrite from samples of submarine polymetallic chimneys.
- to make a genetic model of antimony mineralization and cycling in shallow-submarine hydrothermal vent systems associated with arc-volcanoes. What is the source of antimony and the host phases in hydrothermal chimney samples?
- to improve our knowledge about the fate of antimony during environmental processes (e.g. seafloor hydrothermal diagenesis, weathering etc). Can seafloor hydrothermal biogenic and abiotic solids act as environmentally reliable sink for long-term immobilization of Sb^{5+} ? Is it possible to make predictions on the fate of antimony associated with Fe-sulfides and oxyhydroxides in natural seafloor environments?

5. Material and methods

The studied Kolumbo samples were recovered in September 2011 during the oceanographic expedition with cruise number NA014 (“Hellenic Volcanic Arc and Cretan Basin”) of the “New Frontiers in Ocean Exploration 2011” project (**Principal Investigator Robert Ballard, Institute for Exploration & Ocean Exploration Trust, University of Rhode Island URI, USA**)(State File No. F2011-049, 2012)

The expedition with the use of Exploration Vessel (E/V) Nautilus and was sponsored by: (1) Institute for Exploration (IFE), a division of Mystic Aquarium & Institute for Exploration (MAIFE); (2) National Geographic Society (NGS); (3) NOAA Office of Ocean Exploration and Research (OER); (3) Ocean Exploration Trust (OET); (4) Office of Naval Research (ONR). Chief scientists for NA014 were Katherine Croff Bell (Ocean Exploration Trust, University of Rhode Island (URI) USA, and Paraskevi Nomikou (National and Kapodistrian University of Athens, Dept. of Geology and Geoenvironment, Greece.

The E/V *Nautilus* is a 64-meter research vessel, owned and operated by the *Institute for Exploration, Ocean Exploration Trust & University of Rhode Island (URI) Center for Ocean Exploration* and is equipped with the remotely operated vehicles (ROVs) Hercules and Argus. The Hercules and Argus system is a state-of-the-art deep sea robotic laboratory capable of exploring depths up to 4,000 meters and is equipped with a dedicated suite of cameras and sensors that receive electrical power from the surface through a fiber-optic cable, which also transmits data and video. The ROV Hercules is equipped with a number of tools, including a suction sampler, sampling boxes, and sediment coring equipment, a suite of mapping instruments that enable detailed visual and acoustic seafloor surveys.

5.1 Sampling

Sampling campaign and methods are detailed in Institute for Exploration, Ocean Exploration Trust & URI Center for Ocean Exploration-State File No. F2011-049 (2012) and **Kilias et al.(2013)**. Solid hydrothermal vent samples studied in this M.Sc. thesis are shown in Figs. 5.1, 5.2, 5.3, 5.4, and Table 5.1. Sample NA014-016 (Fig. 5.4) was recovered from an anonymous active vent site at Latitude (36°31.2020N) and Longitude (25° 29.5877 E) at depth 499.7 m.

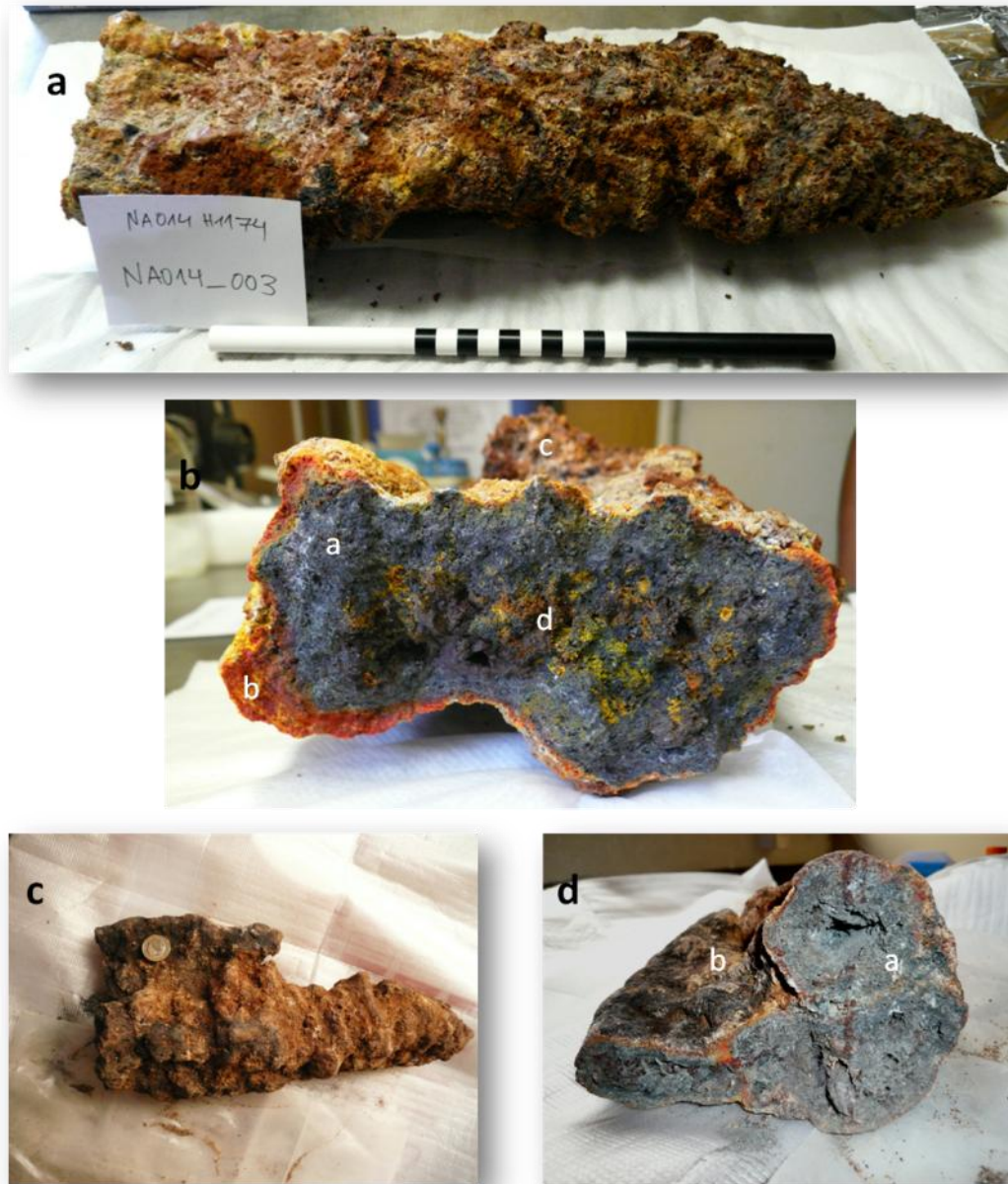


Fig.5.1 Ex-situ photographs of solid hydrothermal vent samples. Politeia Vent Complex. (a) Sulphide-sulphate spire sample NA014-003 and NA014-039, (b) The base of sample NA014-003 revealing four textural zones: a. "Inner sulphide-sulphate core" (ISSC), b. thin orange-yellow outer As-sulphide-dominated layer (OASL), c. orange to brown Fe-(hydrated)-oxyhydroxide-dominated microbial surface Fe crust (SFeC), d. Unidentified dark-violet phases similar to Sb-Zn-S phases in interior porous conduit network (IPCN)(see page 7, Kiliyas et al., 2013), (c) Spire sample NA014-039 and basal cross section (d).

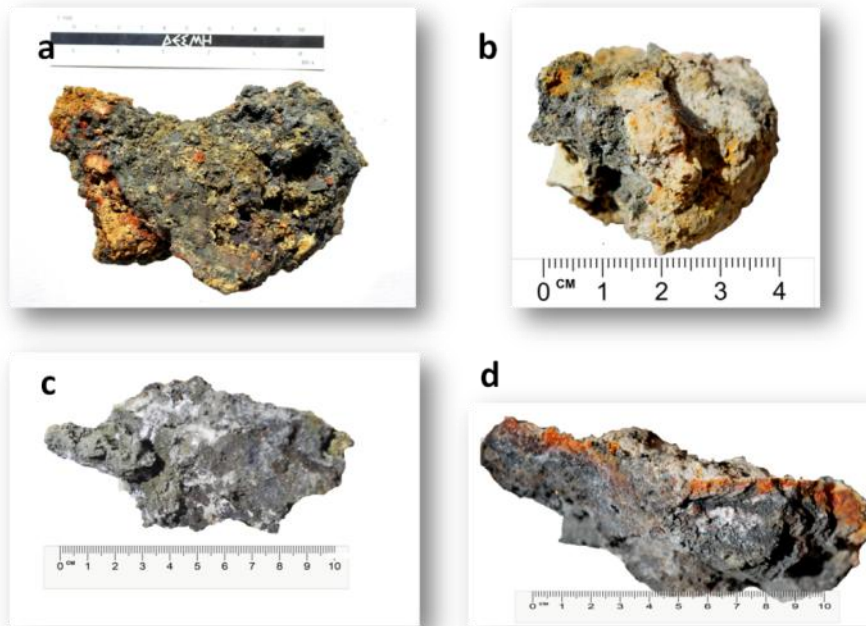


Fig.5.2 Ex-situ photographs of solid hydrothermal vents samples, Champagne vent complex. (a) NA014-007, (b) NA014-027, (c) NA014-028, (d) sample NA014-028. Gray: massive sulphide, white: barite crystals. orange-yellow: As-rich sulphides.

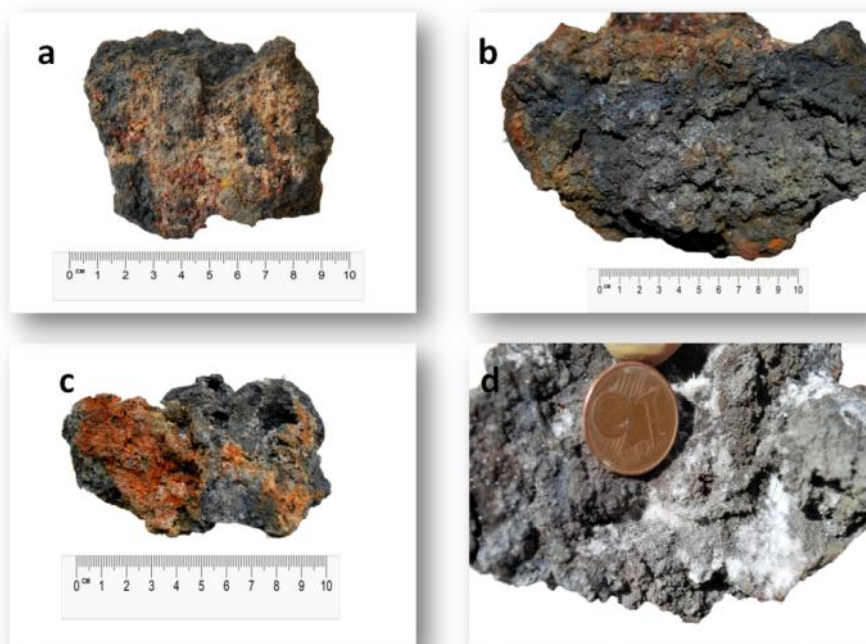


Fig.5.3 Ex-situ photographs of solid hydrothermal vent samples. Hydrothermal mound samples recovered from Diffuser II vent complex: (a), (b), (c) Sample NA014-005. (d) Barite crystals (white) on sulphide substrate (grey) of NA014-005.

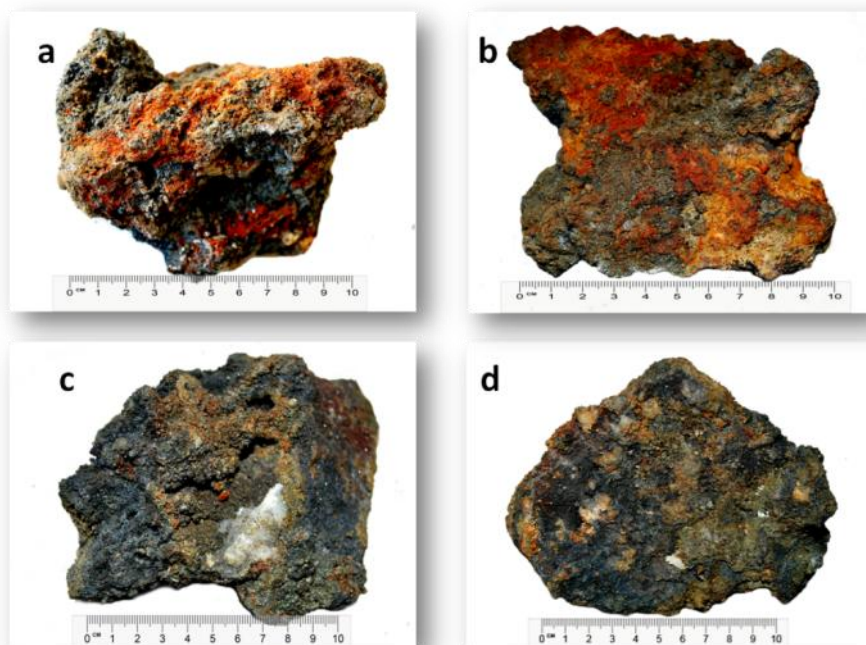


Fig.5.4 Ex-situ photographs of solid hydrothermal vent samples. Sample NA014-016 was recovered from an anonymous active vent site at Latitude ($36^{\circ} 31.2020\text{N}$) and Longitude ($25^{\circ} 29.5877\text{ E}$) at depth 499.7 m.

5.2 Preparation of samples

Polished blocks were prepared from samples NA014-003, NA014-005, NA014-007, NA014-016, NA014-019, NA014-027, NA014-028, NA014-039 for mineralogical characterization in reflected light. In addition three samples (NA014-003crust, NA014-039crust, NA014-016crust) which were obtained with a toothbrush and/or dental tools, were powdered for geochemical analysis (Table 5.1). Twenty four polished thin sections were made from sample NA013-003 in order to study spire mineralogy from the bottom to the top and from the core to the crust (Fig. 5.7, 5.8). Two polished thin sections from the sample NA014-005 and two from the sample NA014-016. In addition three polished blocks were made from each sample NA014-007, NA014-027 and NA014-028, and two polished blocks from the orange-yellow outer layer (OAsL) of NA014-003 (Fig 5.7). Finally small species were extracted with dental tools recovered by the interior porous conduits network (IPCN) (Fig. 5.8), the Fe-(hydrated)-oxyhydroxide-dominated microbial surface Fe-crust (SFc) and the orange-yellow outer As-sulphide-dominated layer (OAsL) (Fig. 5.9) for SEM-EDS analysis. Table 2.1 illustrates the list of samples (red) studied in this M.Sc. thesis.

Samples NA014-003 and NA014-039 which measured , 22 cm long and 14 cm in diameter, and 38 cm long and 10 cm in diameter, respectively, were cut in two mirror halves along their vertical long axis. (Figs. 5.5, 5.6). Their inner structures could then be observed consisting of anastomosing, discontinuous array of narrow (~2 cm diameter) channels delineating original fluid-flow paths, occurring within a porous sponge-like spire interior (diffusers)(Figs. 5.5, 5.6). One half of NA014-003 was stored for future reference and educational activities , whereas the second half was cut in slabs based on a grid, as shown in Figure 5.5; the grid was designed on the basis of thin section dimensions (27mm x 46 mm) (Fig. 5.5). Blocks FG2', FG4', EFG5' and FG6' were cut carefully at the end. Polished thin sections for detailed petrographic and geochemical analyses were made of these slabs, and have been assigned sample numbers as shown in Figure 5.5 (i.e D1,D2,D3,D4,D5,D6,D7,D8,CDE9',E8 ---FG2', FG4', EFG5', FG6, FG4'*, FG6'* (The thin sections FG4'*, FG6'* correspond to the vertical surfaces of sections FG4, FG6 respectively). Similar sampling strategy was applied to sample NA014-039 (Fig. 5.6), (i.e. C2, C3, C4, C5, C6, C7 and AB2', AB4' from the periphery).

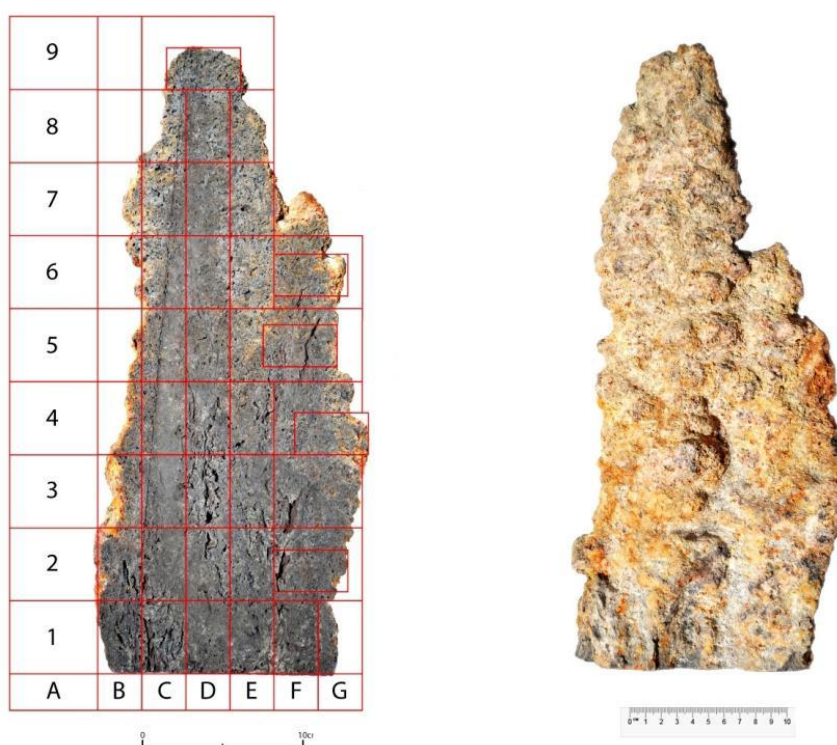


FIG.5.5 (a) Interior cut face of one half of NA014-003. Polished thin sections D1,D2,D3,D4,D5,D6,D7,D8,CDE9',E8,FG2',FG4',EFG5',FG6,FG4'*,FG6'* were made based on a grid sampling strategy explained in the text. (b) View of exterior surface.



Fig.5.6 (a) Interior cut face of one half of NA014-039. Polished thin sections (C2, C3, C4, C5, C6, C7, AB2', AB4') were made based on a grid sampling strategy explained in the text. (b) View of exterior surface.

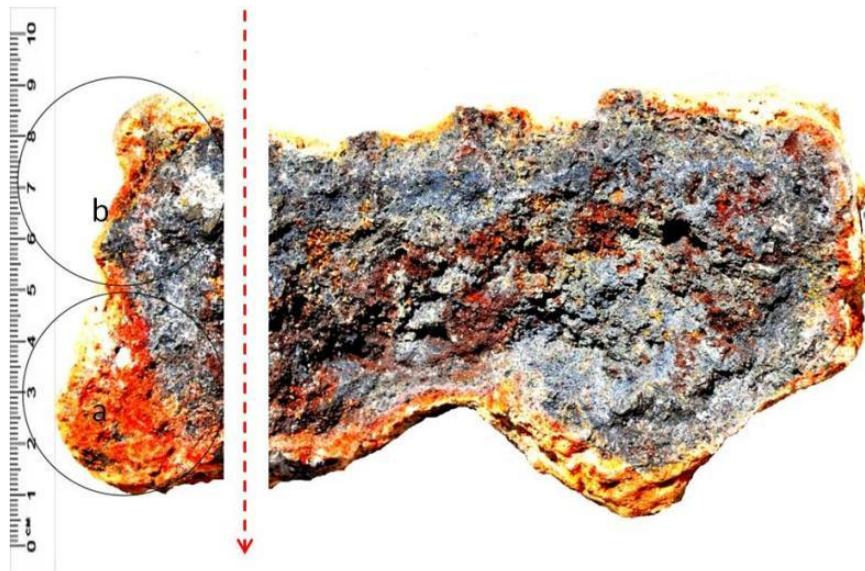


Fig.5.7 The red arrow shows the cross section of orange-yellow slab. Two polished blocks were made (NA014-003-OAsL a, b)



Fig.5.8 Unidentified dark-violet phases similar to Sb-Zn-S are lining interior porous conduit network of (a) Sample NA014-003 (IPCN) –in polished thin section FG3(Fig.2.5) (b) Sample NA014-003 (IPCN) –polished thin section EFG5'(Fig.2.5).



Fig.5.9 (a) Orange-yellow outer As-sulphide-dominated layer (OASL) of Politeia spire 1, (b) small pieces recovered by OASL (c) detail of b in reflected microscope.

Table 5.1. List of samples which be made for mineralogical and geochemical studies. In this Msc thesis were studied the samples in red color.

Samples		Mineralogical analysis			Geochemical analysis
		Polished thin sections	Polished blocks	Pieces	Powders
Politeia Vent Complex	NA014-003 ISSC	D1,D2,D3,D4,D5,D6,D7,D8,CDE9',E8,FG2', FG4', EFG5', FG6, FG4'*, FG6'*	003		003, 005, 007, 016, 027, 028, 039
	NA014-003 OAsL		003a,003b	003-OAsL	003CRUST
	NA014-003 SFeC			003-SFeC	
	NA014-003 IPC			003-IPN	
	NA014-039 ISSC	C2, C3, C4, C5, C6, C7, AB2', AB4'	039		039CRUST
NA014-039 SFeC					
Champagne Vent Complex	NA014-007		007, 007b		
	NA014-027		027, 027b		
	NA014-028		028, 028b		
Anonymous vent	NA014-016	016 a, 016 b	016		016CRUST
	NA014-016 CRUST				
Diffuser II	NA014-005	005a, 005b	005		

5.3 Analytical methods

5.3.1 Chemical analysis

5.3.1.1 Total elemental analysis of vent samples

Six samples (NA014-003CRUST, NA014-039CRUST, NA014-016CRUST, NA014-016, NA014-007, NA014-005) were air-dried and pulverized using an agate mortar and sent to ACME Analytical Laboratories Ltd in Vancouver for elemental analysis. Bulk analyses for major and minor and rare earth elements were performed using a Perkin Elmer ICP-OES and a Perkin Elmer Sciex Elan 9000 ICP-MS following a $\text{LiBO}_2/\text{LiB}_4\text{O}_7$ fusion and HNO_3 digestion of a 0.2 g sample. In addition, a separate 0.5 g split was digested in a HNO_3 : HCl mixture (1:3)-aqua regia- and analysed by ICP-MS for precious and base metals. The bulk (total) sulfur content was determined using a Leco elemental analyzer. Analytical quality control procedures included analysis of 1 duplicate, 2 blank solutions as well as analysis of a series of appropriate reference materials (OREAS45CA, DS8, DOLOMITE-2, SO-18, GS311-1, GS910-4).

5.3.1.2 Sequential extraction (Modified BCR method (Rauret et al., 1999))

Two samples air-dried and pulverized taken from the previous study (NA014-003-ISSC, NA014-039-ISSC) (Kilias et al., 2013) and three samples from this study (NA014-003CRUST, NA014-039CRUST, NA014-016CRUST) were selected for sequential extraction, conducted in the laboratories of Department of Chemistry, N.K.U.A. This methodology was employed based on clustering of elements observed in the initial bulk total analysis of the samples (Kilias et al., 2013). It was expected that further recognition of elemental speciation could be achieved by applying the sequential method to core and crust sub-samples. A four-step sequential extraction (Rauret et al., 1999) was carried out to evaluate As, Ag, Tl, Sb concentrations in the carbonate, Fe-oxides, sulfides and residual extraction steps (Table 5.2). These phases differ in respect with potential availability of elements into the environment and include in the order of decreasing availability: (a) the exchangeable fraction, i.e. metals adsorbed in exchange sites on surfaces of clays and colloids; the metal fraction associated with carbonate minerals and metals specifically adsorbed on surfaces of amorphous precipitates of Fe, Al, Mn oxides/hydroxides and phosphates; (b) the reducible phase comprising metals associated with Mn and Fe oxides through co-precipitation and binding within the oxide structure; (c) the oxidisable phase, i.e. the fraction of metals bound to soil organic matter and metals incorporated in the structure of sulphide minerals. As an internal

check on the procedure, the residue from step (c) was digested in aqua regia. The total amount of metal extracted (i.e. sum of steps (a)+(b) +(c) + residual) was compared with that obtained by aqua regia digestion of a separate 1 g sample of the sediment.

Table 5.2 The sequential chemical extraction scheme used in this study. Modified after (Rauret et al., 1999).

Step	Fraction	Extractant	Conditions
1	Easily extracted- specifically adsorbed and Carbonate phases	CH ₃ COOH (0.11M)	pH=2.85, 22+5C,16 h shaking periodically rinsed with DI
2	Reducible- bound to Fe-Mn oxides	HONH ₂ HCl (0.5M)	pH=2, 22+5C,16 h shaking periodically rinsed with DI
3	Oxidisable- bound to organic matter and Sulfides	H ₂ O ₂ (8.8M) followed by NH ₄ CH ₃ CO ₂ (1M)	pH=2, 22+5C,16 h shaking periodically rinsed with DI
4	Residual	Aqua regia 3:1 HNO ₃ to HCl	85+2C, 2 h rinsed with DI

The detailed procedure of the analytical method is described below:

Step 1-Bound to Carbonates

We added 20 ml of 0.11 mol l⁻¹ acetic acid (CH₃COOH) to 0,4g of sediment in a 100ml centrifuge tube, then we extracted by mechanical shaking for 16 h at 22 ± 5°C (overnight) . No delay should occur between the addition of the extractant solution and the beginning of the shaking. We separated the extract from the solid residue by centrifugation at 3000g for 20 min and decant liquid into a polyethylene container. We stored the residue in a refrigerator at about 4 °C prior to analysis.

Step 2-Bound to Fe-Mn Oxides

We added 10 ml of distilled water into the residue and we shook for 15 min on the end-over-end shaker and centrifuging for 20min at 3000g.We decanted the supernatant and discarded, taking care not to discard any of the solid residue.

We added 20 ml of 0.5 mol l⁻¹ hydroxylammonium chloride (HONH₂ HCl) freshly prepared, to the residue from step 1 in the centrifuge tube. Then we shook, stoppered and extracted by mechanical shaking for 16 h at 22±5°C (overnight). No delay should occur between the addition of the extractant solution and the beginning of the shaking. We separated the extract from the solid residue by centrifugation and decantation as in step 1. Finally we stored the residue in a refrigerator for analysis.

Step 3-Bound to Organic Matter and sulfides

We added 10 ml of distilled water into the residue and we shook for 15 min on the end-over-end shaker and centrifuging for 20 min at 3000g. We decanted the supernatant and discarded, taking care not to discard any of the solid residue. Then we carefully added 10 ml of 8.8 mol l⁻¹ hydrogen peroxide (H₂O₂) to the residue in the centrifuge tube in small aliquots, (1 ml/10 minutes with occasional manual shaking) without cover the vessel and we digested at room temperature for 1 hour more. We continued the digestion for 4 h at 85±2°C in a water bath, by uncovered tube, until reducing of the volume to less than 3 ml. We added 25 ml of 1.0 mol l⁻¹ ammonium acetate, (NH₄CH₃CO₂⁻) to the cool moist residue and shook for 16 h at 22± 5°C (overnight). No delay should occur between the addition of the extractant solution and the beginning of the shaking. We separated the extract from the solid residue by centrifugation and decantation as in step 1. Finally we stored the residue in a refrigerator for analysis.

Step 4-Residual

The residue from the step 3 was digested in aqua regia, (a mixture of acids in a volume ratio of 1:3 (2,25 ml HNO₃ & 6,75 ml HCl), but we added also 1,5 ml H₂O) for 2 h at 85±2°C in a waterbath, by uncovered tube. Then we separated the extract from the solid residue by centrifugation and decantation as in step 1. Finally we stored the residue in a refrigerator for analysis.

The residue from step 3 with aqua regia is compared with that obtained by aqua regia digestion of a separate 0,4g sample of the sediment. The solutions have very high density and it needs to be diluted with deionized water in a volume ratio 1:100 (we also added HNO₃ in a volume ratio 2:100). The solutions were analysed by inductively coupled plasma-mass spectrometry (ICP-MS) at Quality control laboratory for solid fuels, department of analytical laboratories (I.G.M.E-Attiki).

D' Amore et al., (2005) recorded two reviews that report on the basic pitfalls and limitations of sequential extraction in soils (**Salamons et al., 1984; Nirel and Morel, 1990;**

Scheckel et al., 2003). In their critique, **Nirel et al., (1990)** claim validation of extraction schemes and the classes of “species” extracted have not been done. The comparisons of sequential extractions with thermodynamic models and direct instrumental analyses are lacking. **Salamons et al., (1984)** assert that extraction efficiencies vary according to the solid to reagent ratio and the length of contact time between the two. The results are influenced of the drying of the particle size and whether a sample has been ground or left intact. Also re-adsorption of the trace element into other compartments can take place before solid-extract separation, while precipitation can occur during extraction or storage of the extract before elemental analysis. Despite the difficulties, sequential extraction method is relatively easy to apply, but they are plagued with a number of problems detailed in the literature.

5.3.2 Mineralogical analysis

5.3.2.1 Optical microscopy & Scanning electron microscopy

Seven samples (NA014-003, NA014-005, NA014-007, NA014-016, NA014-027, NA014-028, NA014-039) were selected for mineralogical analysis. Polished thin sections and polished blocks were made in the labs of I.G.M.E, Attiki.

Optical microscopy and Scanning Electron Microscopy-Energy Dispersive Spectrometry (SEM-EDS) techniques were used for mineral identification and textural interpretation. The polished thin sections were also investigated with the optical microscope in transmitted and reflected light housed in the Department of Geology and Geoenvironment at the N.K.U.A. SEM was used mainly to assist with mineral identification when such identification was uncertain by petrographic techniques. Scanning Electron Microscopy-Energy Dispersive Spectrometry (SEM-EDS) investigation of carbon-coated free surfaces and polished (in epoxy resin) solid samples was performed using a Jeol JSM-5600 SEM equipped with an Oxford EDS. The conditions of analysis were: Accelerating Voltage: 20 kV, Beam Current: 0,5 nA, Livetime: 50 sec ,Beam Diameter: < 2 µm. A combination of Powder XRD (PXRD) and SEM/EDS analyses was applied to clarify the mineralogical history and composition of the ISSC.

5.3.3 Synchrotron Radiation analysis: Phase Contrast Imaging and Micro-spectroscopy

The Synchrotron Radiation (SR) study was conducted at the ANKA facility, Karlsruhe Institute of Technology, Germany) by members of the Kolumbo Study Group (see **Kilias et al., 2013**) Athanasios Godelitsas, Platon Gamaletsos, Theo J. Mertzimekis, Joerg Goettlicher, and Ralph Steininger, and the analytical methodology is copied here.

The advent of very bright third generation synchrotron facilities has led to incredible advances in microscopy techniques. This includes the analysis of trace elements in minerals with high accuracy and spatial resolution (SXRF). Spectroscopic methods are used to study chemical bonding in minerals and crystals, but also for solving structural problems or to determine cation distributions ((XAS, XAFS /EXAFS, XANES). Recently, the combination of μ -XRF with spatially resolved XAS became an important tool for speciation in environmental and geological materials and for the study of processes in chemical species transformation.

5.3.3.1 Synchrotron radiation X-Ray fluorescence analysis (SR- μ -XRF)

X-Ray fluorescence (XRF) spectrometry had an important impact as one of the first commercially available instrumental techniques for elemental analysis (**Van Grieken et al., 2002**). The Fe-sulfide PXRD amorphous phases of ISSC were characterized by X-ray absorption fine structure (XAFS) spectroscopy at the SUL-X beam line of ANKA Synchrotron facility (KIT, Germany).

5.3.3.2 Micro-X-ray Absorption Fine Structure (XAFS) spectroscopy

To confirm the chemical and to determine the structural character of the Sb-precipitates, a Synchrotron-based spectroscopic investigation was performed on the ISSC material of politeia spire-2 (NA014-039). The Fe-sulfide PXRD amorphous phases of ISSC were characterized by X-ray absorption fine structure (XAFS) spectroscopy at the SUL-X beam line of ANKA Synchrotron facility (KIT, Germany). XAFS spectra of sample ISSC were obtained from fine-grained material pressed with cellulose to pellets. Elemental Sb, Stibnite ($\text{Sb}^{3+}_2\text{O}_3$) and Tripuhyite ($\text{Fe}^{3+}\text{Sb}^{5+}\text{O}_4$), were used as reference materials of various Sb species. The spectra were processed using Athena software (**Ravel et al., 2005**).

6. Results

6.1 Mineralogy and mineral chemistry

Seven samples (NA014-003, NA014-005, NA014-007, NA014-016, NA014-027, NA01-028, NA014-039) were used for mineralogical and textural characterization; the samples originated from four different hydrothermal fields (Politeia vent complex, Champagne vent complex, Diffuser II vent complex, active vent site at Latitude(36° 31.2020N) and Longitude (25° 29.5877E) named here “Anonymous Vent” (AV)). Optical microscopy using transmitted and reflected light, and Scanning Electron Microscopy-Energy Dispersive Spectrometry (SEM-EDS) techniques were used for mineral identification and textural interpretation. Five probe-grade standard-sized (27 x 46 mm) polished thin sections and five polished blocks have been studied (Table 5.1-in red). Observations have been made regarding sulphide mineral occurrence, mineralogy and textural relationships between the sulphide minerals relative to the surrounding sulphate, silicate and oxide minerals. This information helps deciphering the paragenesis of the sulfide minerals.

6.1.1 Politeia Vent Complex

According to **Kilias et al. (2013)**, the Politeia spire-1 and spire-2 structures (NA014-003, NA014-039) studied here, constitute carbonaceous sulphide-sulphate diffuser chimneys which consist for the most part (> 90%) of a lithified dark-gray “inner sulphide-sulphate core” (ISSC). The ISSC is mantled by a thin outer rind composed of a multicolored “outer Asulphide layer” (OAsL) (1-3 cm wide) which in turn is covered by a gelatinous orange to brown Fe microbial mat designated as “surface Fe-rich crust” (SFeC) (Figs. 5.1b). The interior conduits are lined by barite and gypsum overgrown by dark violet metallic aggregates (IPC) (Fig. 5.8).

Studied sample numbers are shown in Table 5.1, and their relative location on the spires in Figure 5.5.

6.1.1.1. Mineralogy of the “Inner Sulphide-Sulphate Core” (ISSC)

Optical observations in reflected and transmitted light, and SEM-EDS analysis, assisted by XRD investigation (**Kilias et al., 2013 and this study**) revealed four sulphide phases within a barite matrix (BaSO_4), namely pyrite (FeS_2), sphalerite (ZnS) and galena (PbS) and unidentified Pb-Sb sulphosalt phases; in addition, the examination of the polished thin

sections revealed that the samples are highly porous (Fig. 6.1 a, b). The description of the phases is given below:

Barite (BaSO_4) occurs as blades, acicular clusters, fibrous crystals and rarely as dendritic crystals (Fig. 6.1); also, barite laths and rosettes form the substrate for disseminated sulphides of disseminated sphalerite (grey) (Fig. 6.1c) and mainly colloform banded pyrite (Fig. 6.1e,f). Moreover, barite occurs as rosettes and plumose aggregates intergrown with complex Sb-Pb-sulfosalts (Fig. 6.1d).

Pyrite in the ISCC displays complex textures, but can generally be grouped into three types:

Pyrite 1 includes compact, peloid-like (Figs. 6.2c, e) and stromatolite-like laminated pyrite varieties. The latter occurs: (1) as oncoïd-like (**sensu Cavalazzi et al., 2007**) concentric lamination, which may be internally zoned (Fig. 6.2d), (2) as composite intergrowth or overgrowth textures (Fig. 6.4f), (3) as non-isopachous planar wavy to irregular lamination (Fig. 6.2f) or (4) concentrically banded, radial, spheroidal masses of pyrite/marcasite (Fig. 6.2 h) (**see also Fig. 123 in Ramdohr, 1980**). Moreover, intricate closely-packed aggregates of rounded and bulbous, oncoïd-like laminated pyrite/marcasite that resemble microscopic cauliflowers, were also observed (**sensu Lazar et al., 2011**) (Fig. 6.2a). Some of the largest oncoïd-like structures display (micro)stromatolite-like laterally linked domical microcolumnar structure (**sensu Allwood et al., 2006**) (Fig. 6.2 b).

In this study, we use the term “peloid” based on the definition given by Chafetz (1986), who described marine peloids as, “...elliptical to spherical bodies ..., generally 20–60 μm in diameter, composed of a fine-grained nucleus which composed of fossil bacterial clumps and are often surrounded by rims of calcite crystallites”. Similar microtexture was observed in sphalerite microglobules from Bleiberg (Austria) (**Kucha et al., 2005**).

Pyrite 2 forms massive anhedral porous, spongy rims around pyrite 1; these rims are up to 25 μm thick (Figs. 6.2 f 6.3 b, 6.3d), and they can locally be discontinuous (Fig. 6.2).

Pyrite 3 forms euhedral (idiomorphic) cubic crystals from about 100 μm to 200 μm across, occurring as isolated euhedra (Fig. 6.3a) clusters of euhedral crystals, or bands of euhedral crystals.

Sphalerite (ZnS) is mostly anhedral and intergrown with barite (Fig. 6.3 c, h) and pyrite (Fig. 6.3 c); some sphalerite grains have inclusions of galena (PbS) (Fig. 6.3e). Though difficult to observe occasional internal reflections have been seen in sphalerite (dark grey

phase), exhibiting a wide range of colors, from pale yellow-orange to dark red, and are variably translucent to opaque. These differences reflect variable Fe contents.

Galena (PbS) is white subhedral to euhedral and typically less than a few tens of μm in size. Galena occurring as inclusions in sphalerite grains (Fig.6.3e), or as isolated galena at grain contacts of highly porous Fe-oxyhydroxide (Fig.6.2g ,6.3g). Also galena intergrown with Pb-Sb sulphosalts (Figs 6.3f, 6.4d).

Unidentified Pb-Sb sulphosalts reveal a distinct anisotropy (bluish) (Fig. 6.4 a) and a weak pleochroism (blue-green tint) (Fig.6.4.b), optically resembling boulangerite ($\text{Pb}_5\text{Sb}_4\text{S}_{11}$).

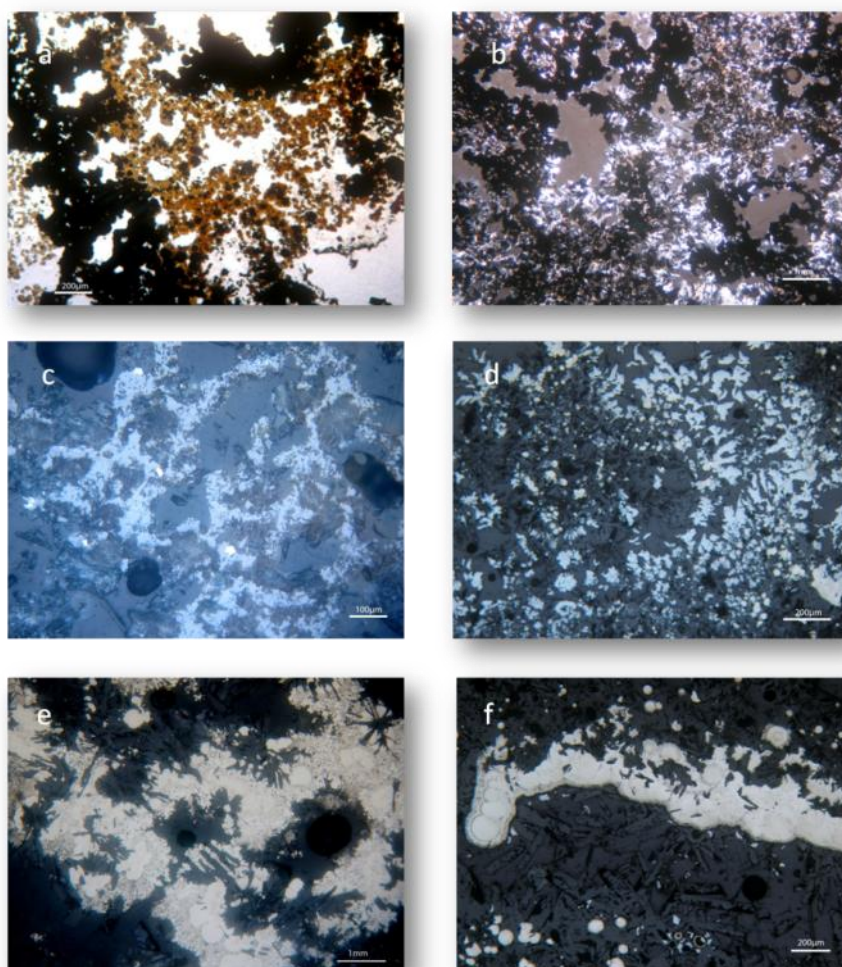


Fig.6.1 Photomicrographs of commonly seen textures in the inner sulphide-sulphate core (ISSC). (a) Sample NA014-003, polished thin section D2: transmitted light photomicrograph (TLP). Porous nature of the ISSC composed of disseminated Fe-sulphide microglobules (black) mantled by sphalerite (honey-brown) and patches of massive pyrite (black). Barite forms the groundmass. (b) D2: TLP. Fe sulfides (black) and barite (light white) set in a porous matrix (brown grey) (c) Sample NA014-039, polished thin section AB4: Reflected light photomicrograph (RLP). Typical texture of

disseminated sphalerite (grey) in a barite (dark grey) matrix. (d) AB4: RLP. Disseminated skeletal Pb-Sb sulfosalts intergrown with pyrite (yellow) in a barite matrix (dark grey). (e) AB4: RLP. RLP of white to light grey pyrite spherical to ovoid structures (microglobules) of various sizes, occurring as single or dense massive clusters (e), and /or colloform banded planar layers (f) in a porous barite (Ba) matrix (darker gray).

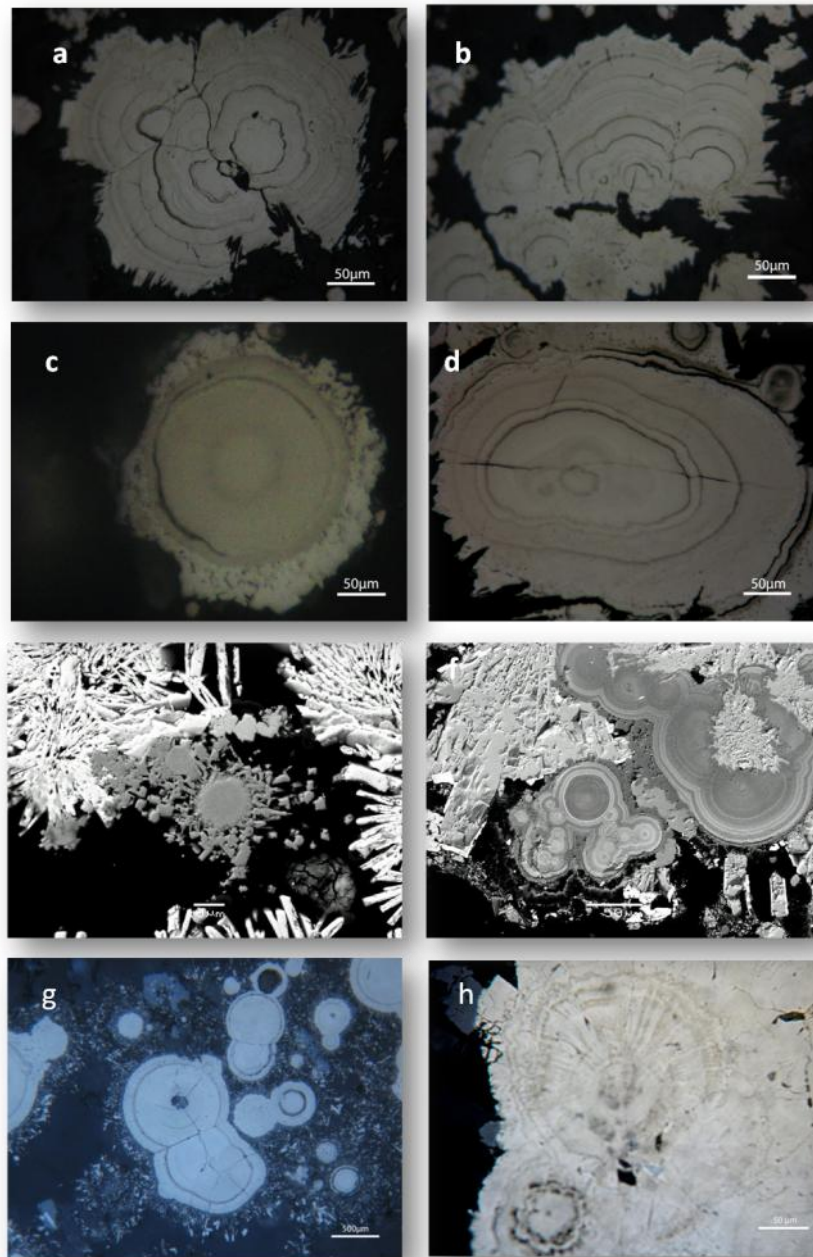


Fig.6.2 Textures of pyrite/marcasite from the ISSC as observed in optical microscopy and backscattered electron images. (a) Sample NA014, polished thin section EFG5: RLP of intricate closely-packed aggregates of rounded and bulbous, oncoid-like (sensu Cavalazzi et al., 2007) laminated pyrite/marcasite that resemble microscopic cauliflowers (laminites). (b) EFG5: RLP of finely laminated pyrite-marcasite fabric; the shape of the lamination reveals growth structure: laterally linked low-relief planar to domical (micro)stromatolitic morphology (Lazar et al., 2012;

Alwood et al., 2006). (c) Sample NA014-039, polished thin section AB4: SEM-BSE image showing composite pyrite-Fe-oxyhydroxide-galena microglobule interpreted as a peloid (sensu Chafetz, 1986; see also Fig. 4D in Kucha et al., 2005); the light gray core is composed by pyrite (confirmed by EDS) granules peripherally altered to porous /amorphous Fe-oxyhydroxide and surrounded by anhedral galena (PbS) rim. (d) Sample NA014-003, EFG5: RLP of pyrite/marcasite structure with oncoid-like concentric laminations (Cavalazzi et al., 2007) (e) Sample NA014-003, D5: SEM –BSE image of pyrite/marcasite structure consisting of compact spheres surrounded by granular dentate and porous rims. (f) EFG5: SEM-BSE image of pyrite/marcasite with fine concentrically laminated microstromatolite-like structure with “barren” As-rich porous rim, overgrowing, and/or set in, barite matrix, showing oscillatory and chemical zoning; zones “bright” in BSE are enriched in Sb and/or Pb, As and Si (see Fig.3.6); note that laminated structure. (g) Sample NA014-039, AB4: RLP image showing pyrite concentric sphere surrounded by an amorphous Fe-oxyhydroxide (confirmed by SEM) with inclusions of PbS (h) Sample NA014-003-D2 : RLP of clusters of Fe-sulphide concentrically laminated spheres mantled by amorphous Fe-oxyhydroxide-galena rims (confirmed by SEM) (h) D2 : RLP showing concentrically banded, radial, spheroidal masses of iron sulphide (see Fig.123, Ramdohr, 1980).

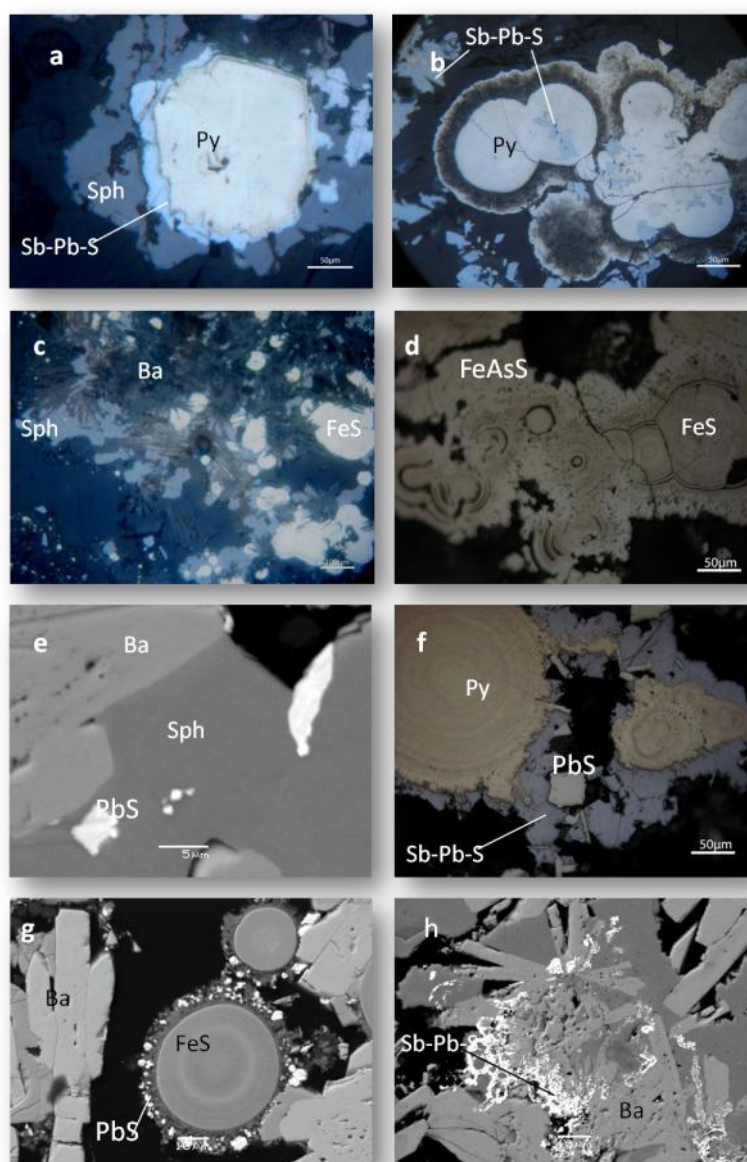


Fig 6.3 Inner sulphide-sulphate core (ISSC) mineral phases. (a) Sample NA014-003, polished thin section D2: Reflected light photomicrograph(RLP) of an idiomorphic crystal of pyrite/marcasite(Py) mantled by Sb-Pb-sulfosalts (Sb-Pb-S), then later sphalerite (Sph). (b) Sample NA014-039, AB4: RLP of anhedral Sb-Pb-sulfosalt inclusions in concentrically laminated pyrite (Py) overgrown by thin porous As-pyrite, mantled by barite laths with scattered Sb-Pb-sulfosalts. (c) Sample NA014-003, EFG5: RLP of clusters of pyrite/marcasite spheres/hemispheres/ and barite laths/rossettes mantled by sphalerite. (d) Sample NA014-003, EFG5: RLP of intricate colloform banding of pyrite 1 (FeS) mantled by a layer of spongy. Porous pyrite overgrowths contain As (up to 1.84 wt %), and may be classified as another younger generation pyrite (generation 2). (e) Sample NA014-039, AB4: SEM backscatter image showing galena (PbS) inclusions in sphalerite (Sph) intergrown with concentrically laminated Sb-Pb-rich pyrite spheroid(corfirmedby SEM(EDS)). (f) EFG5: RLP of finely concentrically laminated spheroids, and colloform masses, of pyrite/marcasite (Py) mantled by anhedral to subhedral intergrowths of Sb-Pb-sulfosalts and galena. (g) AB4: SEM backscatter image of finely concentrically laminated pyrite/marcasite sphere surrounded by highly porous Fe-oxyhydroxide, with inclusions of galena. (h) Sample NA014-003, D5: SEM backscatter image of dendritic Sb-Pb sulphosalts (Sb-Pb-S, white) and sphalerite (dark grey) intergrown with barite laths (light gray).

Antimony in the ISSC

Antimony forms either autonomous antimoniferous sulphosalt phases, or is selectively partitioned in pyrite/marcasite.

The antimoniferous phases constitute unidentified Sb-Pb sulfosalts, and exhibit the following modes of occurrence: (1) smooth thin μm -scale non-isopachous fine-grained laminae, and/or more coarsely crystalline dentate masses, that rim oncoïd-like concentrically laminated and chemically zoned pyrite/marcasite, or single euhedral pyrite crystals (Figs. 6.3a; 6.4d,f,g, 6.5), (2) random fine- to coarse-crystalline inclusions in single or dense masses of concentrically laminated, and oncoïd-like, pyrite spheroids/microglobules (Fig. 6.3.b); (3) dendritic masses intergrown with sphalerite and barite(Fig. 6.3h), or random fine-grained inclusions in anhedral sphalerite (Fig. 6.4c); (4) disseminated rhombohedral, anhedral and skeletal grains filling void space of pyrite/marcasite-barite substrate(Fig. 6.4e,h).

Antimony occurs in concentrically laminated pyrite microglobules (pyrite 1) (Fig 6.6). SEM-EDS data show that these concentrically laminated pyrite 1 microglobules have μm -scale compositional variations along the laminae, representing growth zones which are characterized by different Sb and Pb, trace element compositions. Zones "bright" in BSE are enriched in Sb (up to 9.08 wt %), Pb (up to 11.53 wt %) in sample NA-014-003 D5 (Fig. 6.6) (Kiliyas et al., 2013b), or Sb (up to 10 wt %) and Pb (up to 18.13 wt%), in sample NA-014-003-EFG5 (Fig. 6.7). Zones "dark grey" in BSE are trace element-poor (Sb up to 2.13 wt%, Pb and As are not detected). Porous pyrite overgrowths contain As (up to 1.84 wt%), and is classified as another younger pyrite generation (pyrite 2) (Fig.6.6). The abundances of Sb and

Pb vary inversely with Fe and to S (Fig. 6.6), suggesting that Sb and Pb occupy the Fe and S sites in the pyrite (Kilias et al., 2013b).

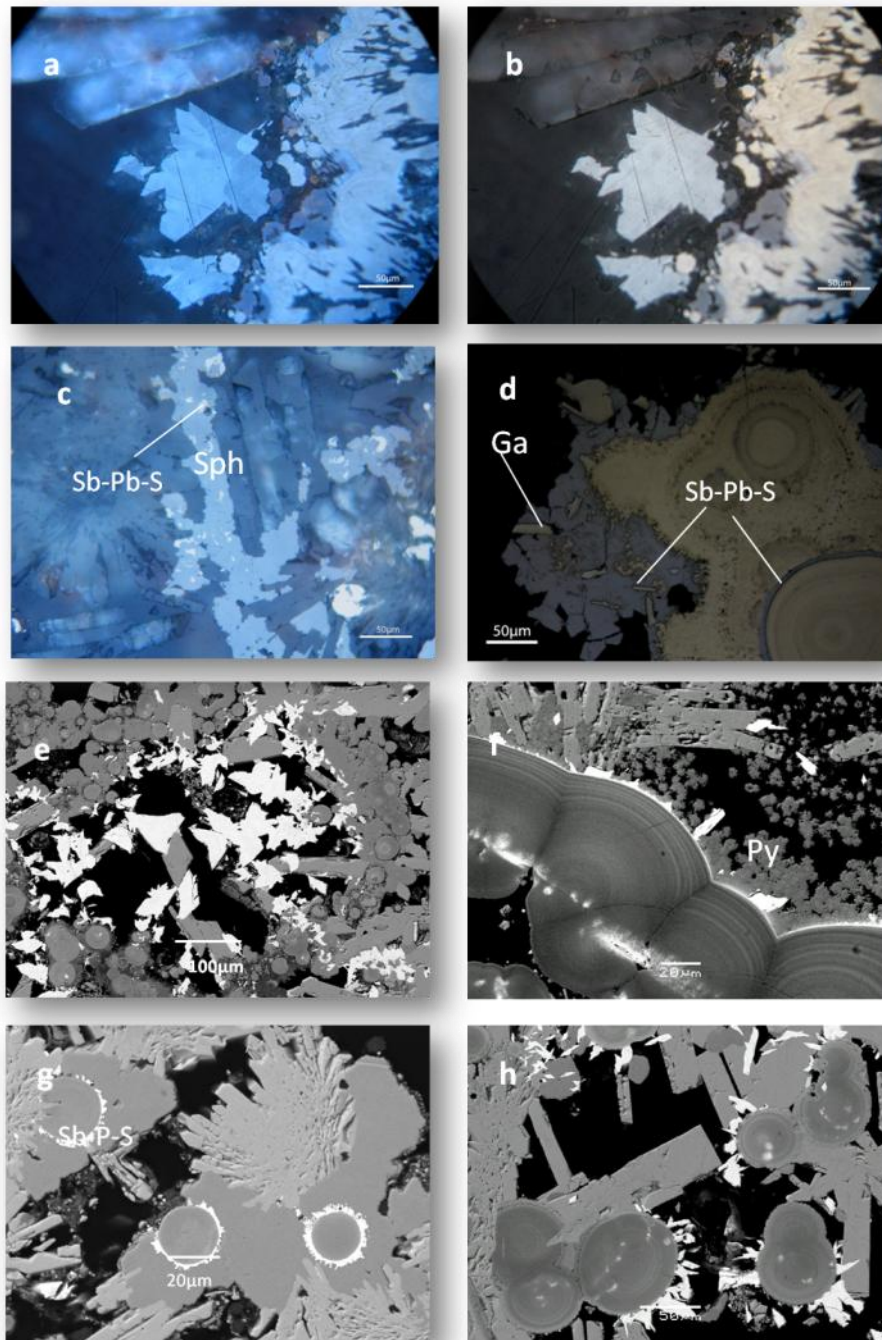


Fig.6.4 Occurrence of Pb-Sb sulphosalt phases.(a) Sample NA014-003, polished thin section D2: Cross-polarized reflected light photomicrograph (CPRLP) showing strong anisotropy of unidentified Pb-Sb sulphosalt phase. Laths towards the upper left side are barite. (b) D2: Reflected light photomicrograph (RLP) in plane polarized light showing strong pleochroism of Pb-Sb sulphosalt shown in (a). (c) Sample NA014-039-AB4: RLP of inclusions of Pb-Sb sulphosalts (Sb-Pb-S) in sphalerite (Sph) in a barite matrix. (d) Sample NA014-003, EFG5: RLP showing two generations of

Pb-Sb sulphosalts: (i) thin rim surrounding pyrite/marcasite peloid; (ii) anhedral to subhedral Pb-Sb sulphosalts intergrown with euhedral galena (Ga) overgrowing and postdating peloidal/microstromatolitic pyrite/marcasite. (e) AB4: SEM backscatter image of rhombohedral, anhedral and skeletal Pb-Sb sulphosalts (white) filling void space of a substrate of disseminated pyrite/marcasite microglobules intergrown with barite laths. (f) EFG5: SEM backscatter image of microstromatolite-like planar to domical pyrite/marcasite laminites (Allwood et al., 2006; Lazar et al., 2011) with intricate fine ultra-local lamination and linked domical pseudocolumnar shape, surrounded by a serrated Pb-Sb sulphosalt rim (EDS analysis: Sb: 30.10 wt% and Pb: 39.6wt%) in barite matrix, (g) Sample NA014-039-AB4: SEM backscatter image of a pyrite and Pb-Sb sulphosalts feature. Random concentrically laminated, zoned Sb-rich pyrite spheres (microglobules) rimmed by dentate Sb-Pb sulphosalts (white) in massive pyrite; the latter is intergrown with or overgrown by barite laths. (h) AB4: Detail of (e).

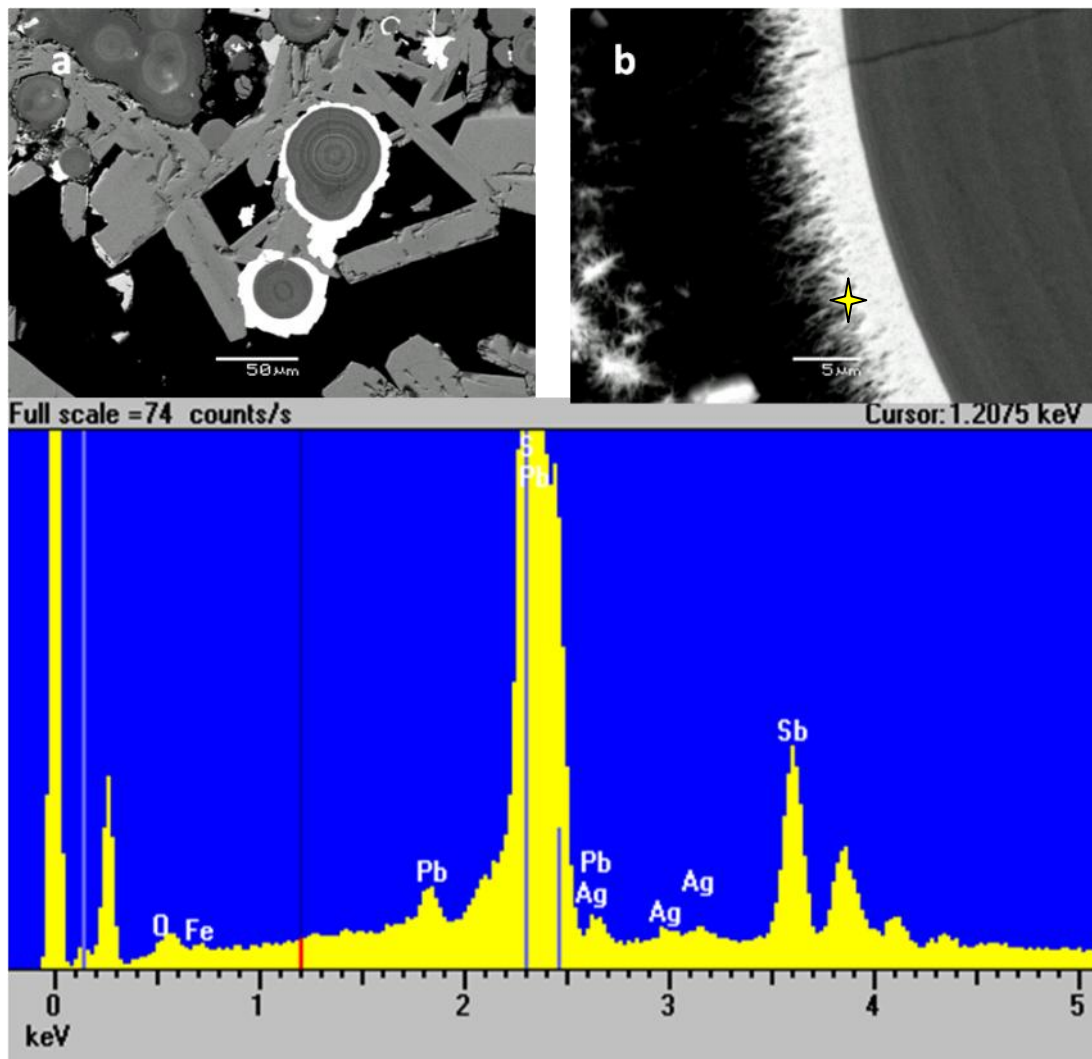


Fig.6.5 Politeia vent 1, sample 003, polished thin section EFG5. (a) Backscattered electron (BSE) image of finely concentrically laminated spheroids mantled by anhedral to subhedral intergrowths of Sb-Pb-sulphosalts. (b) Point of analysis (in yellow) on μm -scale intermingle filament-like texture of sulphosalt phase. (c) SEM-EDS spectrum of the Sb-Pb-sulphosalt phase.

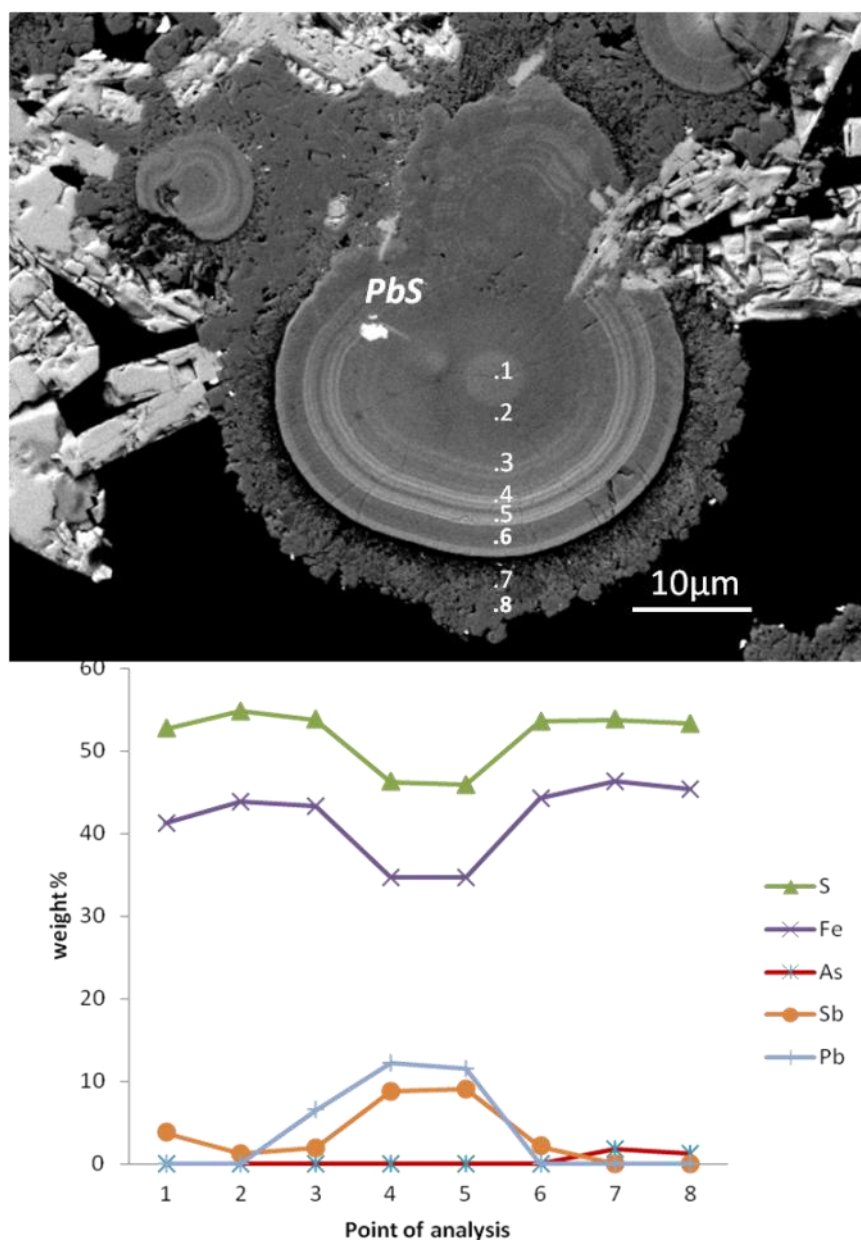


Fig. 6.6 Sample NA014-003, polished thin section D5: (a) Backscattered electron (BSE) image, and EDS spot analyses of concentrically laminated trace-metal (Sb, Pb) rich pyrite oncoid (generation 1) with embedded galena (white), overgrown by thin porous spongy pyrite (generation 2). (b) Element profile across the pyrite oncoid, by EDS spot analyses (Numbers on x-axis refer to analysis points). Pyrite shows chemical growth zoning defined by sharp Sb and Pb variations in the pyrite composition of fine light laminae; pyrite from some laminae may be enriched in Sb up to 9.08 wt% and Pb up to 11.53 wt% (Kilias et al., 2013b). Portions of the microglobules that appear as massive in BSE, i.e. compact cores are trace element-poor (Sb up to 2.13wt%, As and Pb are not detected) Porous pyrite overgrowths contain As (up to 1.84 wt%), and may be classified as another younger generation pyrite (generation 2).

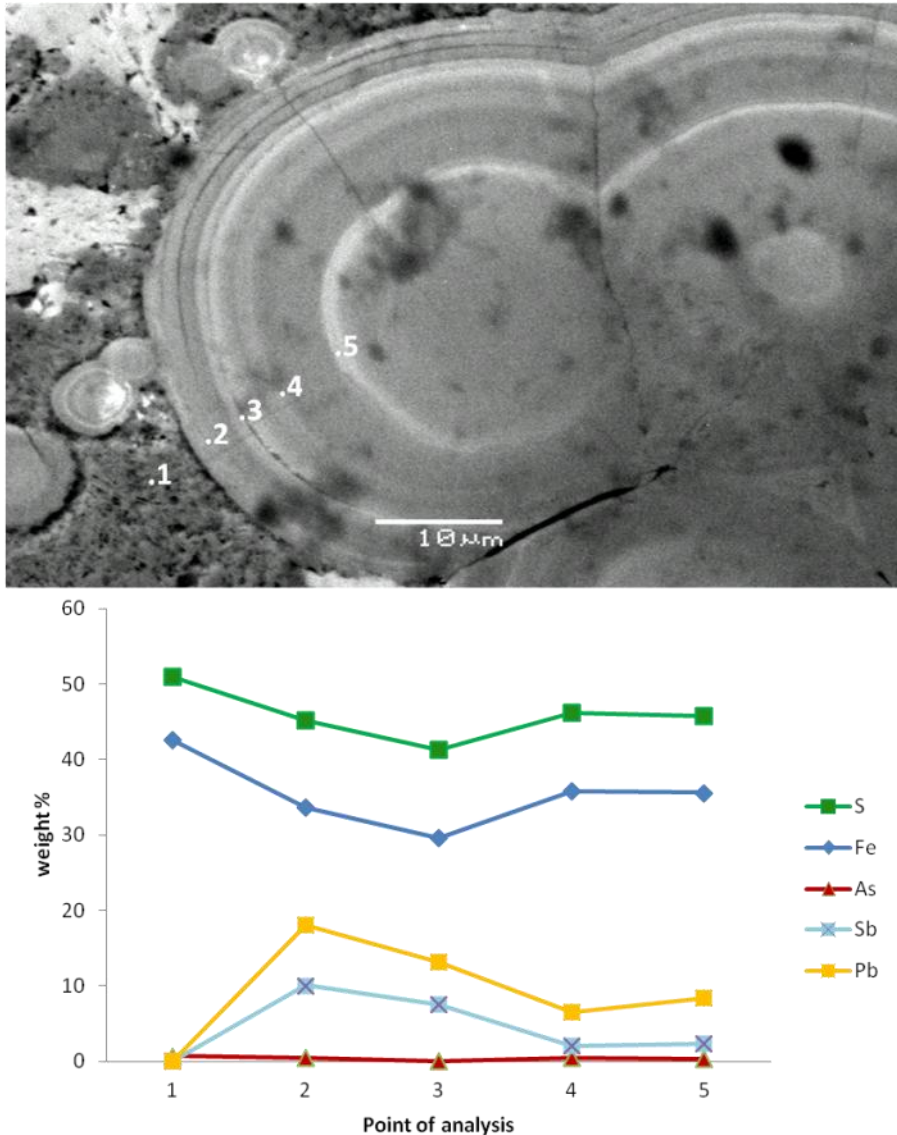


Fig.6.7 Sample NA014-003, polished thin section EFG5: (a) Backscattered electron (BSE) image of concentrically laminated pyrite oncoid (pyrite 1), overgrown by thin porous spongy pyrite (pyrite 2). (b) Element profile (EDS spot analyses) across the spheroid (Numbers on x-axis refer to analysis points). Pyrite shows chemical growth zoning defined by sharp Sb and Pb variations in the pyrite composition of fine light lamination; pyrite/marcasite from some laminae may be enriched in Sb up to 10 wt%, Pb up to 18.13 wt% and As up to 0.48 wt% (point 2). Porous pyrite overgrowths contain As (up to 0.68wt%) (point 1), and is classified as younger generation (pyrite 2).

Subsequent use of synchrotron radiation based μ -XRF elemental mapping, applied to describe the partitioning and distribution of Sb within the pyrite/marcasite phase (Kilias et al., 2013b). Figure 6.8 shows synchrotron radiation μ -XRF elemental distribution maps for Ba, Fe, Zn, As and Sb in an area dominated by concentrically laminated pyrite 1 (light yellow) set in a barite matrix. The first image in upper left is a reflected light microphotograph of

ISSC (NA014-039) showing colloform banding of pyrite/marcasite phase. Ba is inhomogeneously distributed within the field of view whereas Fe, Zn, As and Sb show linear distributions. Zn and Fe partly positively correlate, except for an isometric area (lower left) where Fe is present but Zn is not. As and Sb are positively correlated in a linear structure parallel to the Fe and Zn distribution with some spots of elevated concentrations. These correlations may suggest that Sb occurs either as possible replacement of Sb^{3+} for Fe in the pyrite 1 structure) and/or independent Sb(-As)- sulfosalt phases (Kilias et al 2013b).

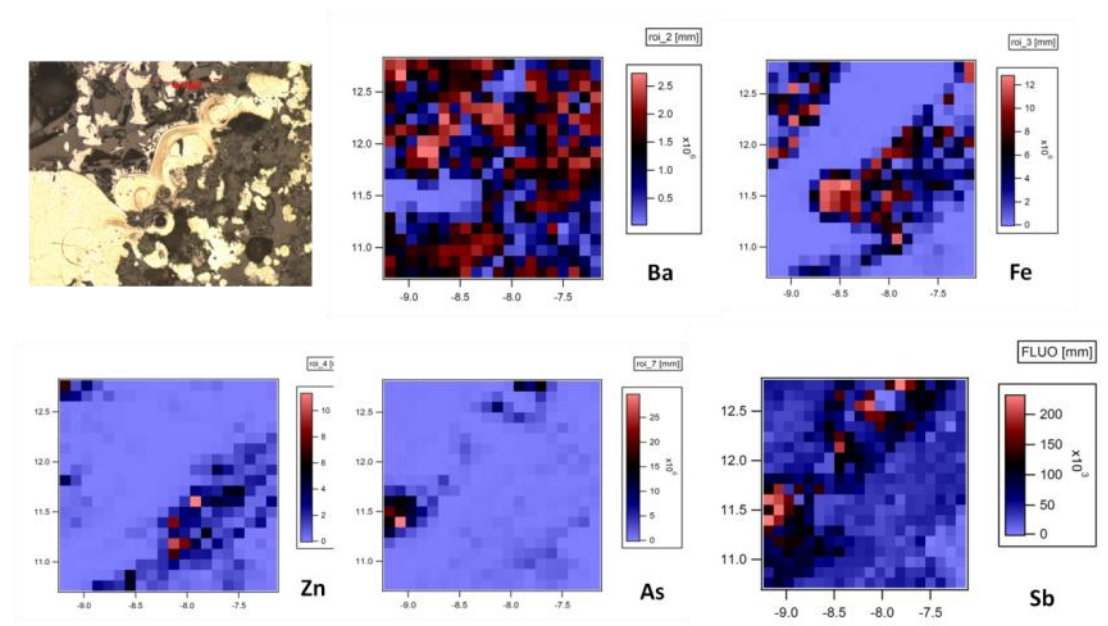


Fig.6.8 Synchrotron radiation μ -XRF elemental distribution maps for Ba, Fe, Zn, As and Sb in an area dominated by layer of finely banded Fe-sulfide (light yellow), set in a barite matrix. The first image is a reflected light microphotograph of the Politeia spire vent-2 (NA014-039). Ba is in homogeneously distributed within the field of view whereas Fe, Zn, As and Sb show linear distributions. Zn and Fe partly correlate, except an isometric area where Fe is present but Zn not. As and Sb are correlated in a linear structure parallel to the Fe and Zn distribution with some spots of elevated concentrations. These correlations may suggest that Sb occurs either as possible replacement of Sb^{3+} for Fe in the pyrite layered structure (and concurrent replacement of As for S^{2-}) and/or independent Sb(-As)- sulfosalt phases (Kilias et al., 2013b)

Speciation of Antimony in Fe-sulfide

Figure 6.9a shows the normalized Sb L3 XANES spectrum recorded from the ISSC material compared to selected reference antimony spectra, and Figure 6.9b shows derivatives of the normalized Sb L3 XANES spectra of the sample (black) compared to the selected reference antimony spectra: the spectra of elemental Sb (blue), $Sb^{3+} 2O_3$ (green) and tripuhyite ($Fe^{3+}Sb^{5+}O_4$) (red). Note that Sb_2O_3 is not pure and seems to contain some Sb^{5+} (see the peak in its derivative at about 4143.6 eV) where the Sb^{5+} reference (tripuhyite)

peak has its maximum. Strange is the position of the second derivative peak of the sample spectrum which plots significantly before the Sb^{3+} peak (Kilias et al., 2013b). The μ -XAFS spectra at LIII-edge for Sb, in amorphous Fe-sulfides from active shallow-submarine hydrothermal vents, applied to confirming the preferential partitioning of Sb within the pyrite/marcasite phase, and the possible dominance of the relatively more toxic trivalent (or lower valence) species (Sb^{3+}) rather than pentavalent species (Sb^{5+}) forms, respectively.

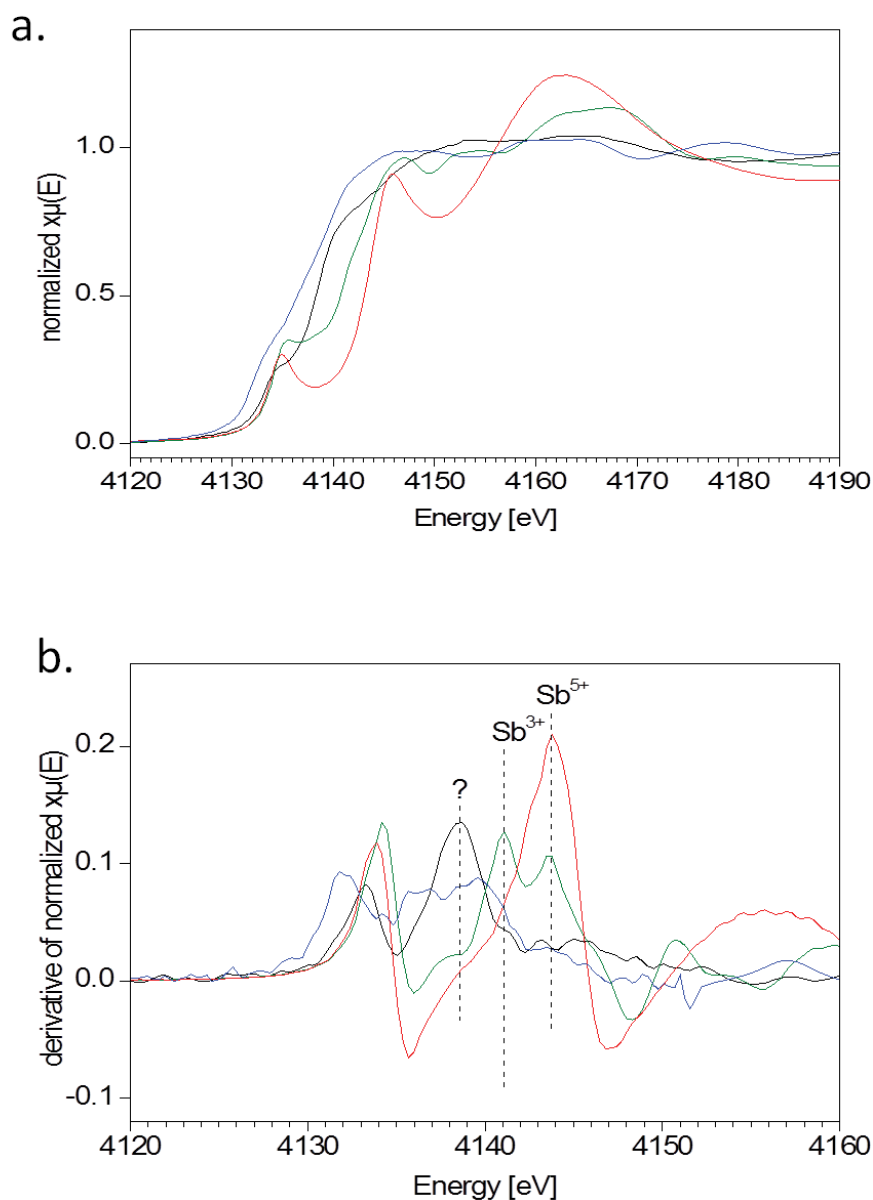


Fig.6.9 (a) Normalized (edge jump of 1) Sb L3 XANES spectra of the sample (black) compared to the spectra of elemental Sb (blue), Sb^{3+}O_3 (green) and Tripuhyite ($\text{Fe}^{3+}\text{Sb}^{5+}\text{O}_4$) (red). Note that Sb_2O_3 is not pure and seems to contain some Sb^{5+} which may have shifted the position of the Sb_2O_3 flank to

a higher energy position than for pure Sb_2O_3 . (b) Derivatives of the normalized Sb L3 XANES spectra of the sample (black) compared to the spectra of elemental Sb (blue), $\text{Sb}^{3+} \text{O}_3$ (green) and tripuyhite ($\text{Fe}^{3+}\text{Sb}^{5+}\text{O}_4$) (red). Note that Sb_2O_3 is not pure and seems to contain some Sb^{5+} (see the peak in its derivative at about 4143.6 eV) where the Sb^{5+} reference (tripuyhite) peak has its maximum. Strange is the position of the second derivative peak of the sample spectrum which plots significantly before the Sb^{3+} peak (Kilias et al., 2013b).

6.1.1.2. Mineralogy of the “Outer As-sulphide Layer” (OAsL)

Optical microscopy revealed typical colors of As-rich sulphide minerals (i.e. orpiment, realgar), in the outer As-sulphide layer OAsL (Fig. 6.10a) (Kilias et al., 2013a). SEM-BSE micrographs of OAsL depict that amorphous orpiment (As_2S_3)-type (characterized by XAFS)(Kilias et al., 2013a) phase occurs as clustered microspheres and globular aggregates of various sizes (1-10 mm), and straight, curved and branching filaments with ringed grooves overlying layer of barite blades (Fig. 6.10 b, c, d).

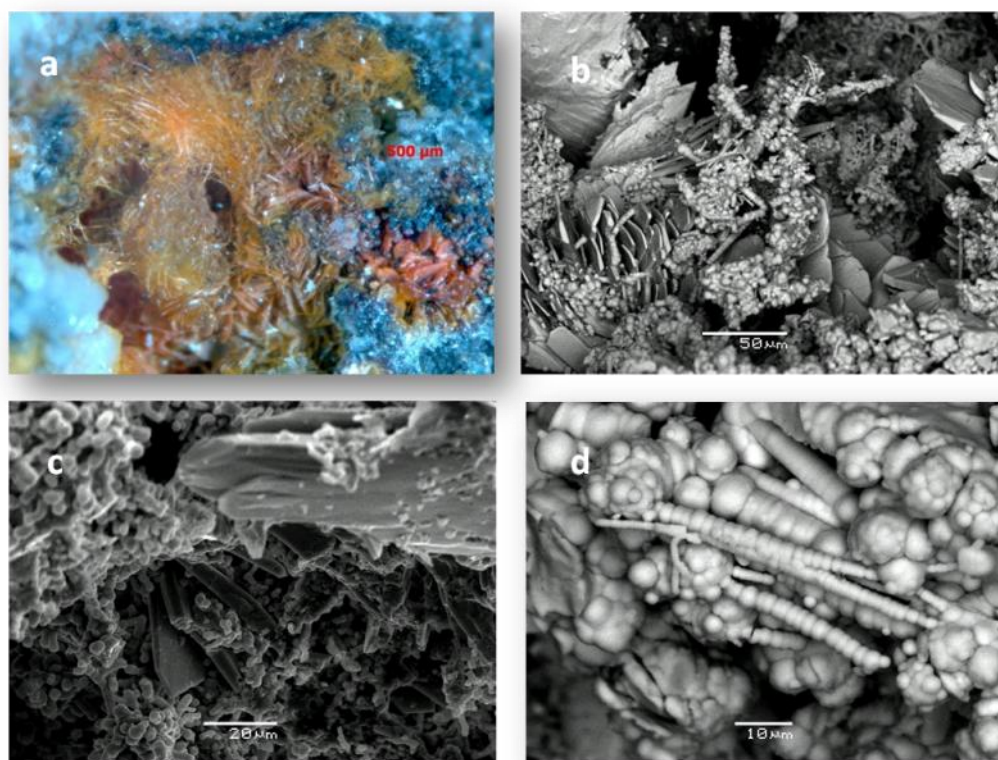


Fig.6.10 (a) Photomicrograph taken in reflected light, of the outer As-sulphide layer (OAsL) of NA014-003: filamentous As-rich sulphides with typical colors of red and yellow; filament compositions approximate orpiment (As_2S_3) (characterized by XAFS) (Kilias et al., 2013). (b)(c)(d) SEM-BSE micrographs of hydrothermal precipitates with fragile morphologies: Overview of amorphous orpiment (As_2S_3)-type phase morphologies, including clustered microspheres and globular aggregates of various sizes (1-10 mm), and straight, curved and branching filaments with ringed grooves overlying layer of barite blades.

Antimony in the OAsL

Antimony in OAsL is selectively partitioned in orpiment (As_2S_3)-type As-sulphide phases. SEM-EDS study of OAsL (NA014-003 OAsL) revealed that colloform aggregates of orpiment (As_2S_3)-type As-sulphide phase contains significant amounts of Sb, along growth zones which appear “bright” in BSE; these zones are highly enriched in Sb up to 16 wt %)(Fig. 6.11).

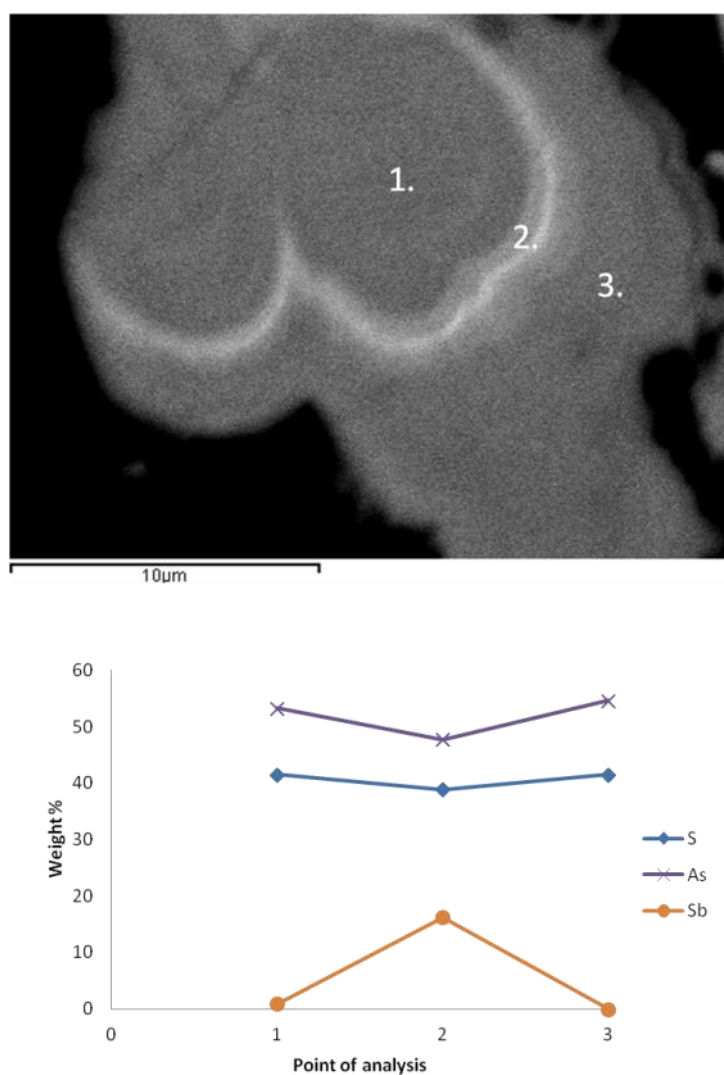


Fig.6.11 (a) BSE image of colloform laminated orpiment (As_2S_3)-type As-sulphide phase (NA014-003 OAsL). (b) Element profile across the colloform orpiment showing significant enrichment of in light laminae in Sb (up to 16wt%) (point 2).

6.1.1.3. Mineralogy of the “Surface Fe-rich Crust” (SFeC)

Antimony in the SFeC

According to **Kilias et al., (2013)** the SFeC is dominated by amorphous ferrihydrite-type (characterized by XAFS) Fe-(hydrated)-oxyhydroxides, occurring as laterally extensive slime-like material, forming an intimate extension of straight and/or curved filamentous, coccoidal, rod-shaped, and long straight stick structures (Fig. 6.12a). SEM-EDS study of surface Fe-rich crust (NA014-039 SFeC), revealed that amorphous ferrihydrite type (characterized by XAFS), Fe-(hydrated)-oxyhydroxides contain significant amounts of Sb (Fig. 6.13).

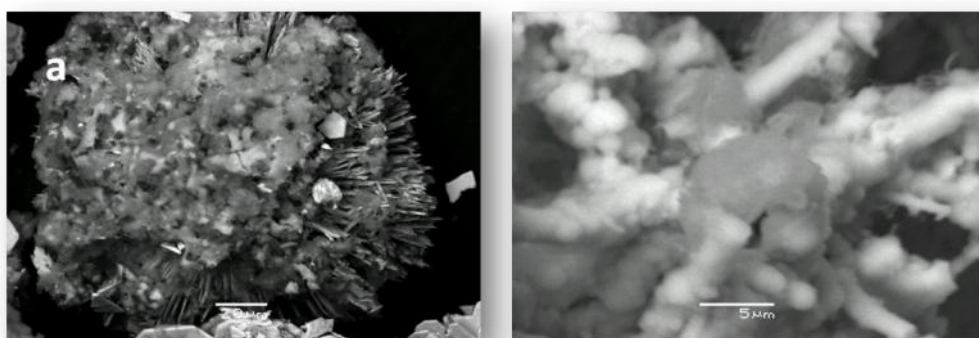


Fig.6.12 SEM images of Fe microbial mat designated as “surface Fe-rich crust ” (SFeC). (a) (b) Amorphous Ferrihydrite-type (Characterized by XAFS) Fe-(hydrated)-oxyhydroxides occurring as laterally extensive slime-like material, forming an intimate extension of straight and/or curved filamentous, coccoidal, rod-shaped, and long straight stick structures (Kilias et al., 2013).

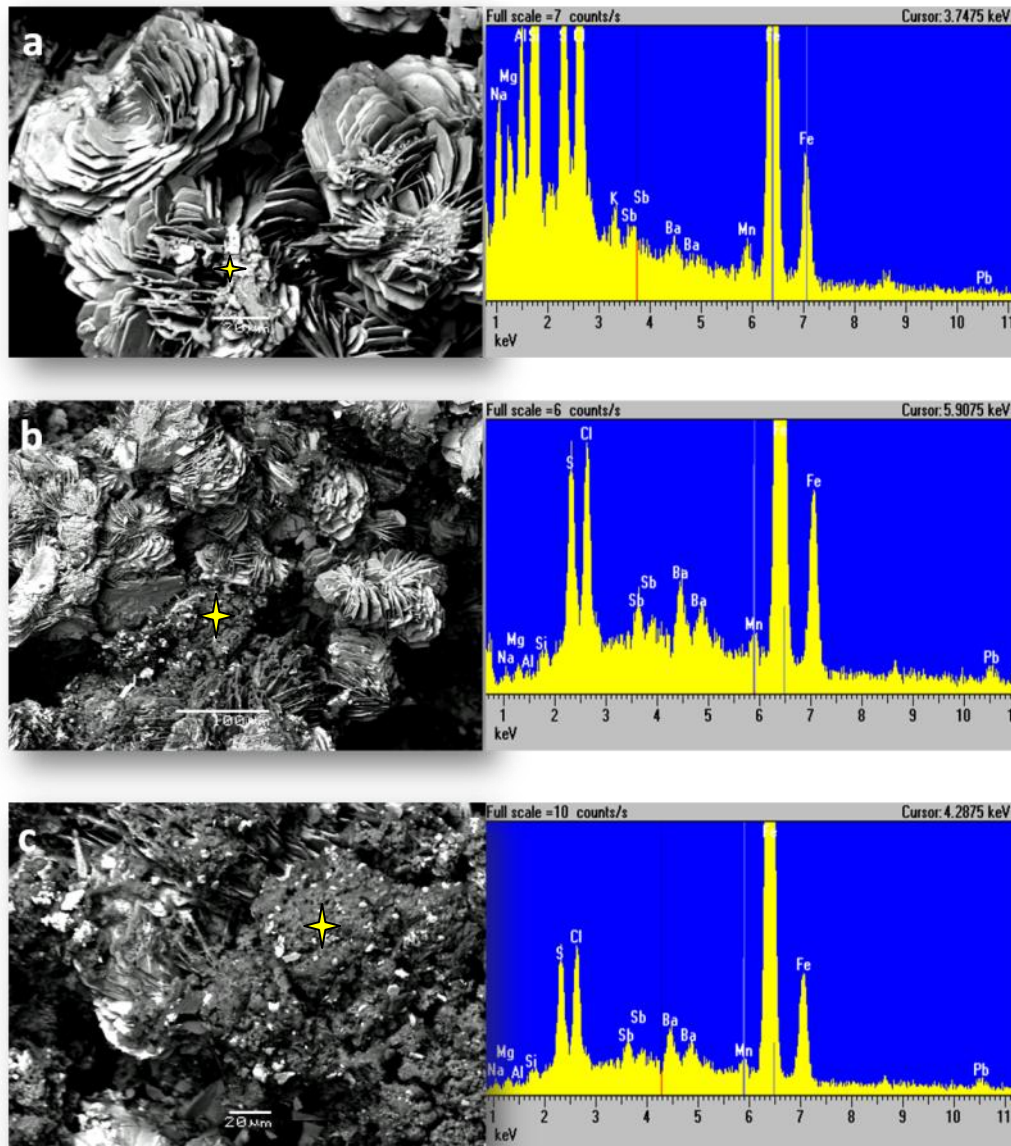


Fig.6.13 (a)(b)(c) SEM-EDS elemental analysis collected from ferrihydrite-type Fe-(hydrated)-oxyhydroxides (NA014-0039 SFeC) gluing and overlying layer of barite blades and roses, indicates Sb content (The asterisks indicate the analysis point).

6.1.1.4. Mineralogy of the “Interior Porous Conduit Network” (IPCN)

Antimony in the IPCN

According to SEM-EDS the interior porous conduits are lined by barite and gypsum overgrown by dark violet metallic aggregates of unidentified PXRD-amorphous Sb-Zn-S phases (Kilias et al., 2013a). In figure 4.16a, EDS spectra show earthy mush of Sb-Zn-S phases in barite substrate. Possible biogenic morphologies include curved and twisted

hairlike filaments entwined with each other forming dense arrays and colonizing barite crystal faces (Fig. 6.14b). Based on Ivarsson et al. (2013) these structures may represent fungi hyphae based on some criteria.

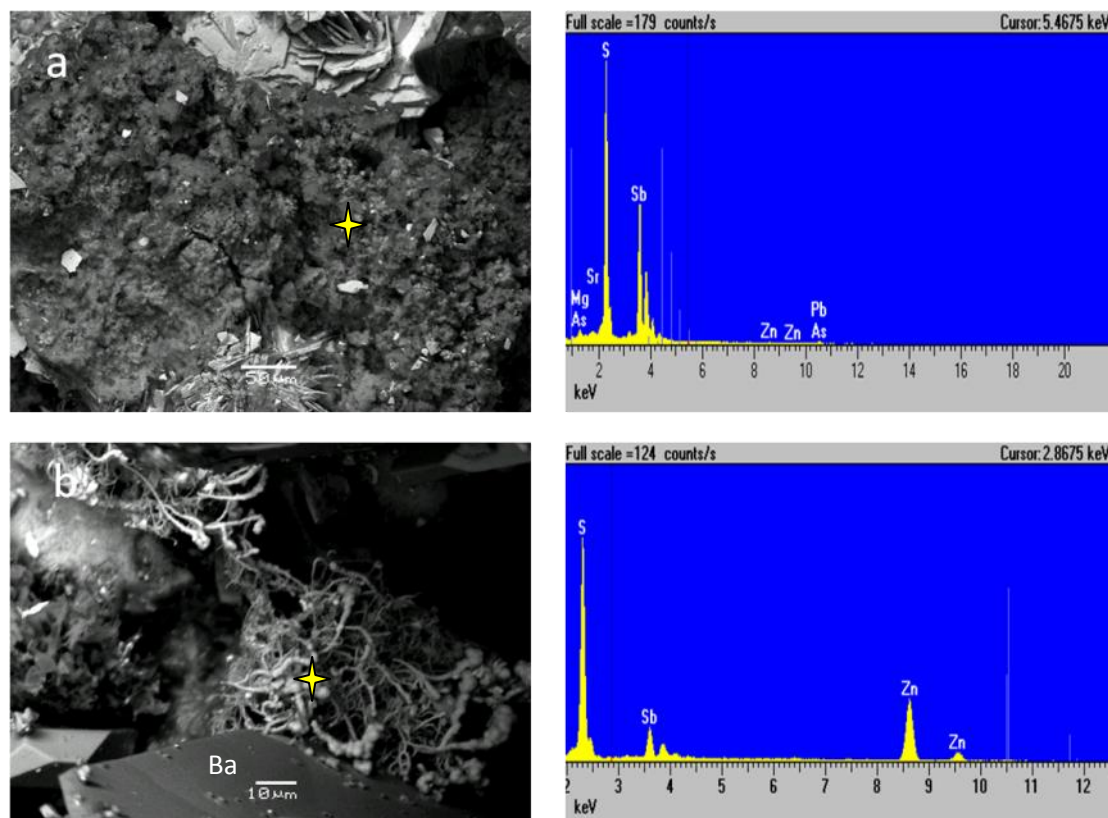


Fig.6.14 EDS spectra show the presence of Zn and Sb. (The asterisks indicate the analysis point). (a) earthy mush of Sb-Zn-S phases in barite substrate, (b) Overview of Sb-Zn-S phase, possible biogenic, morphologies including curved and twisted hair like filaments entwined with each other forming dense arrays and colonizing barite crystal face (ba). A large variation in additional accumulation of oblate or imperfect aggregated microspheres developed on the surface of filaments (Kilias et al., 2013a).

6.1.2 Champagne Vent Complex

According to Kilias et al. (2013a) the external surface of the “Champagne” vent contains botryoidal aggregates of pyrite associated with euhedral gypsum and barite, and local aggregates of twinned chalcopyrite (CuFeS_2) crystals. The polished blocks NA014-027 and NA014-028 are presented here as examples. Observations in reflected and transmitted light and in SEM-EDS revealed five sulphide phases within a barite matrix (BaSO_4), namely pyrite (FeS_2), marcasite(FeS_2),chalcopyrite (CuFeS_2), sphalerite (ZnS) and galena (PbS) and an

unidentified Pb-Sb sulphosalt phase, assisted also by XRD (Kilias et al., 2013 and this study). The description of the phases is given below:

Barite (BaSO_4) occurs as blades, acicular clusters, fibrous crystals and rarely as dendritic crystals and forms the substrate for disseminated sulphides of colloform banded pyrite (Fig 6.15a, b).

Pyrite occurs as colloform banded masses of amorphous trace-metal rich pyrite (Sb is concentrated in the core) mantled by barite blades (Fig.6.15a), colloform banded planar layers commonly intergrowth with sphalerite (dark grey) (Fig. 6.16e) and also in association with chalcopyrite (CuFeS_2), and inclusions of Pb-Sb sulphosalts (Fig. 6.15f). Also pyrite texture reveals a laterally linked low-relief planar to domical (micro) stromatolitic morphology (Fig.6.15b) (Lazar et al., 2012; Alwood et al., 2006).

Marcasite is euhedral and reveals a strong anisotropy (bright bluish) (Fig. 6.15 c), and a weak pleochroism (yellowish-white) (Fig. 6.15d).

Sphalerite is mostly anhedral and intergrowth with pyrite colloform banded planar layers. (Fig.6.15e)

Chalcopyrite has a brassy to golden yellow color and occurs as inclusion in marcasite (6.15d) and intergrown with pyrite/marcasite and Pb-Sb sulphosalts (Fig.6.15 f).

Galena was observed by optical microscopy, but we didn't take any images.

Unidentified Pb-Sb sulphosalts are characterized by a distinct anisotropy (bluish) and a weak pleochroism (blue-green tint) optically resembling boulangerite ($\text{Pb}_5\text{Sb}_4\text{S}_{11}$) and intergrown with pyrite and chalcopyrite (Fig 6.15f).

Antimony in the pyrite

Antimony is mostly concentrated in the core relative to rim. (Fig.6.15a). Elemental profile across the pyrite show chemical growth zoning defined by Cu variations(Fig.6.16) (This picture is redrawn without the Fe and S ,because by this way the variation in As and Cu is shown better).

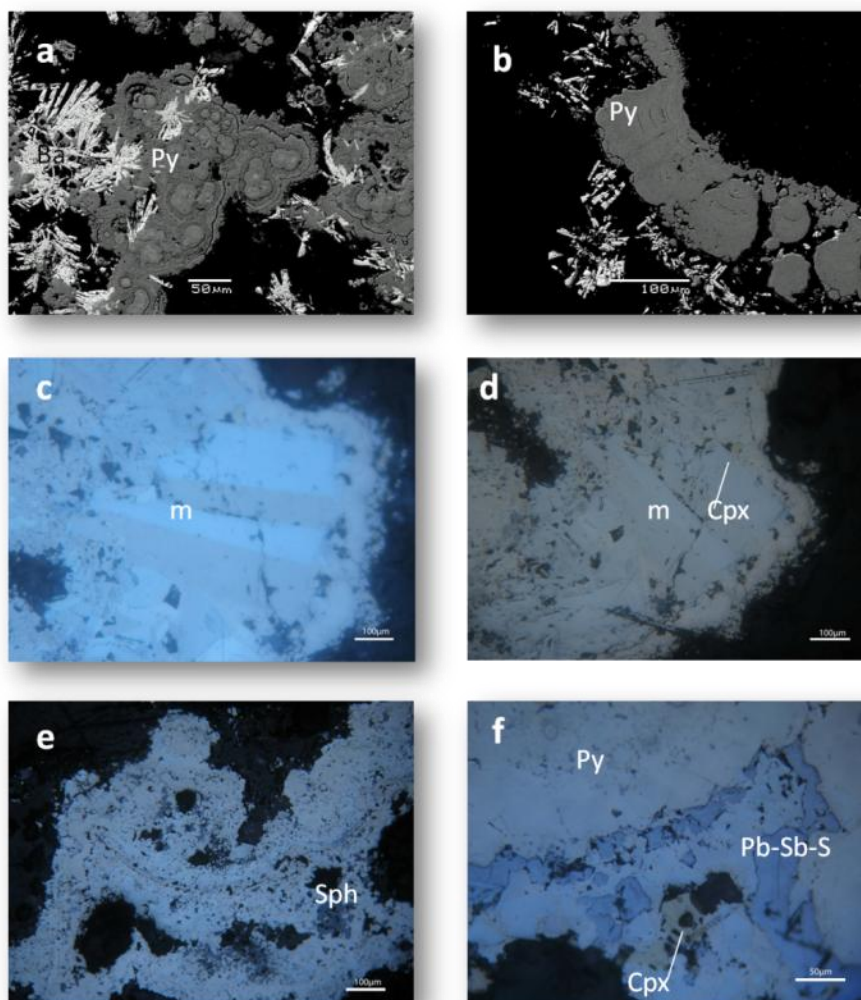


Fig.6.15 Photomicrographs of metallic phases. Sample NA014-028: (a) SEM-EDS photomicrograph shows colloform banded masses of amorphous trace-metal rich pyrite manded by barite blades. Spectrum diagrams show that core, “bright” zones in BSE, is enriched in Sb (up to 11 wt%), and/or Pb, As and Si. (b) Sample NA014-027:SEM-EDS photomicrograph shows laterally linked low-relief planar to domical (micro)stromatolitic pyrite morphology (Lazar et al., 2012; Alwood et al., 2006). (c) Cross-polarized RLP showing marcasite anisotropy, and plane polarized RPL showing marcasite pleochroism with inclusions of Cpx (d). (e) RLP of pyrite colloform banded planar layers commonly intergrowth with sphalerite (dark grey). (f) Intergrowths of pyrite/marcasite, chalcopyrite and Pb-Sb sulphosalts.

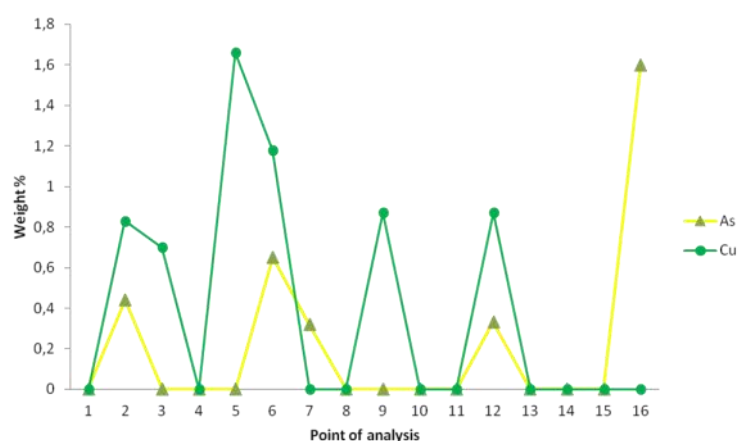
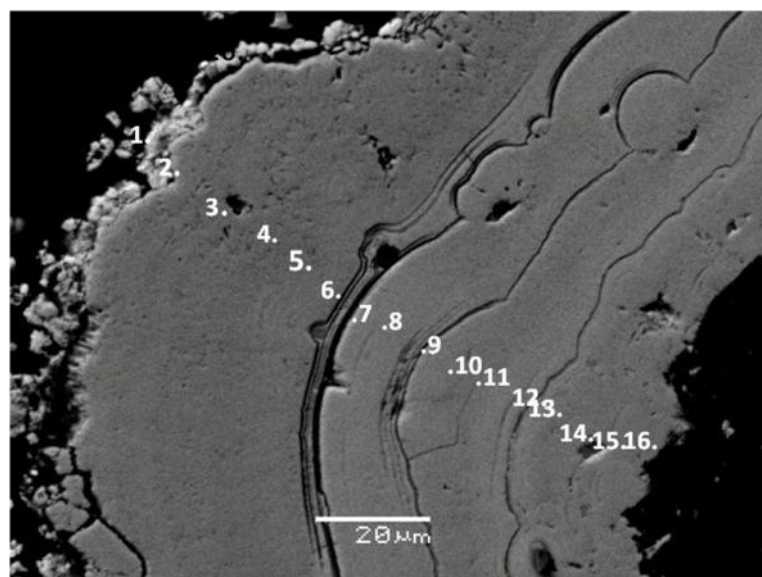


Fig.6.16 (a) BSE image of intricate colloform banding of pyrite polished section NA014-027). (b) Elemental profile across the pyrite show chemical growth zoning defined by Cu and As variations. Sb is not be detected! (This picture is redrawn without the Fe and S ,because by this way the variation in As and Cu is shown better).

6.1.3 Active sulphide-sulphate mounds from Diffuser II complex

Observations in reflected and transmitted light revealed four sulphide phases within a sulphate matrix (barite), which pyrite (FeS_2), sphalerite (ZnS), galena (PbS) and an unidentified Pb-Sb sulphosalt phase. The description of the phases is given below:

Barite (BaSO_4) occurs as blades, acicular clusters, fibrous crystals and rarely as dendritic crystals and forming a substrate for disseminated sulphides of mainly colloform banded pyrite-marcasite (py-m) (Fig.6.17a,b,d,e).

Pyrite mainly include small concentric spheres and colloform masses, commonly intergrowth with barite (Fig. 6.17 a, b) and spherical aggregates (Fig.6.17f). We observed different generations of pyrite: Colloform banded pyrite 1 intergrowth with barite overgrown by thin porous spongy pyrite 2 (Fig. 6.17b) and porous spongy pyrite (generation 2) overgrown by eudral pyrite (generation 3) (Fig, 6.17c). Also in Fig. 6.17 e) idiomorphic crystals of pyrite (generation 3) intergrowth with barite

Sphalerite (ZnS) reveals a massive sulphide formation intergrowth with pyrite/marcasite (Fig.3.18d).

Galena has not be observed in reflected light microscope.

Pb-Sb sulphosalt phase presents a weak reflection pleochroism and a distinct anisotropy. The unidentified Sb-Pb sulfosalts, and exhibit the following modes of occurrence: (1), spherules of pyrite, with concentric lamina mantled by a serrated Sb-Pb sulphosalts bright rim, in barite matrix (Figs. 6.18 a,b,c), and (2) inclusions of Sb-Pb sulphosalts in pyrite intergrown with sphalerite (Fig. 6.18 d).

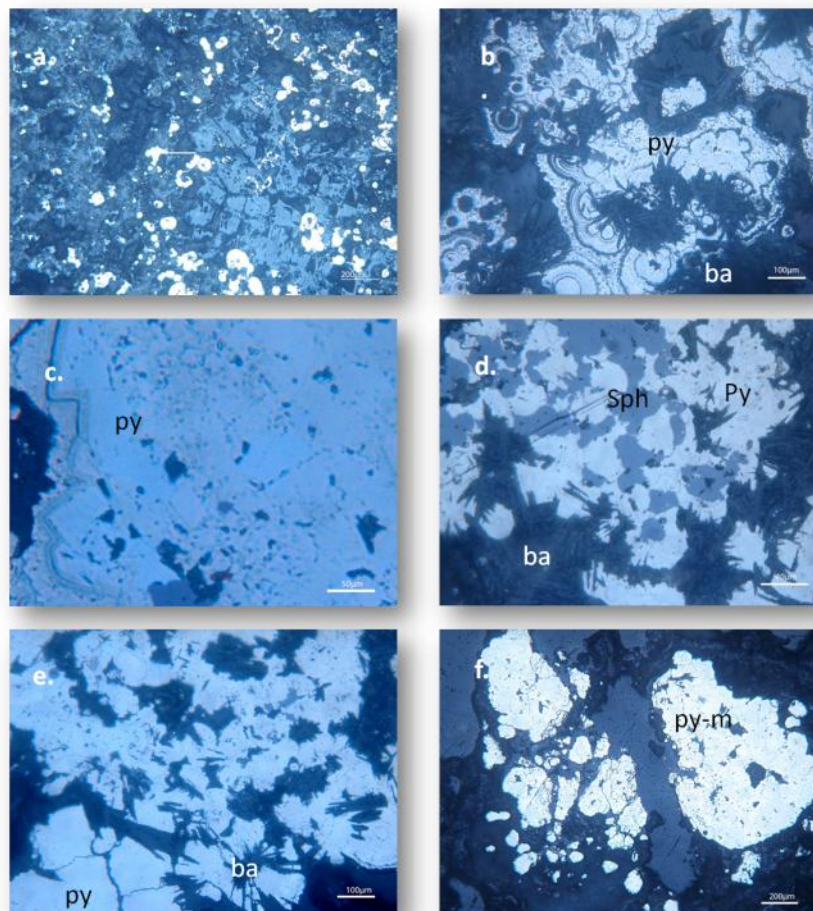


Fig.6.17 Photomicrographs taken in reflected light of metallic phases. Sample NA014-005, polished block: (a) Barite laths and rosettes forming a substrate for disseminated sulphides of mainly colloform banded pyrite-marcasite (py-m) (b) Colloform banded pyrite intergrowth with barite overgrown by thin porous spongy pyrite (generation 2). (c) Porous spongy pyrite (generation 2) overgrown by eudral pyrite (generation 3) (d) Pyrite-sphalerite-barite intergrowth. (e) Idiomorphic crystals of pyrite intergrowth with barite (f) Spherical aggregates of Pyrite-Marcasite.

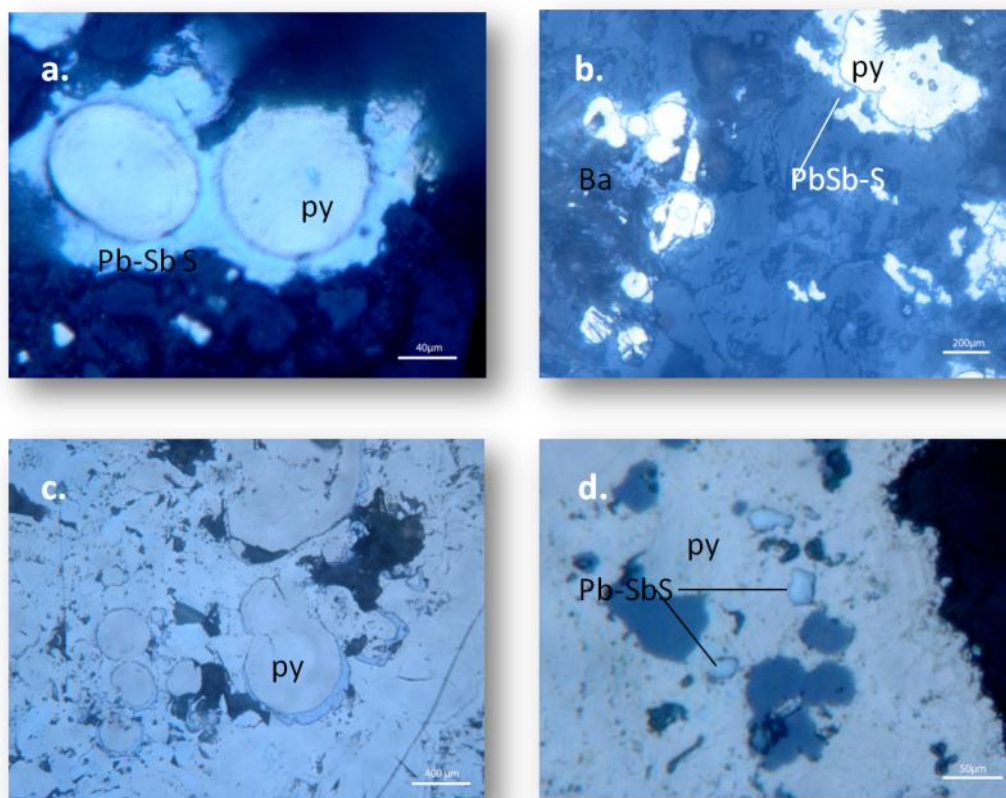


Fig.6.18 Photomicrographs, taken in reflected light of Pb-Sb sulphosalt phases (Sample NA014-005, polished block: (a),(b) Spherules of pyrite, with concentric lamina, rimmed by a serrated Sb-Pb sulfosalts bright rim, in barite matrix (c) Random concentrically laminated, zoned Sb-rich pyrite spheres (microglobles) rimmed by dentate Sb-Pb sulphosalts (white) in massive pyrite; the latter is intergrown with or overgrown by barite laths. (d) Inclusions of Sb-Pb sulphosalts in pyrite intergrown with sphalerite.

6.1.4 Anonymous Vent (AV)

Observations in reflected and transmitted light revealed four sulphide phases within a sulphate matrix (barite), which pyrite (FeS_2), sphalerite (ZnS) and galena (PbS). The description of the phases is given below:

Barite (BaSO_4) occurs as blades, acicular clusters, fibrous crystals and rarely as dendritic crystals (Fig.6.19c,d,e,f). Barite laths and rosettes forming a substrate for colloform masses of pyrite.

Pyrite (FeS_2) reveals some colloform banded masses of amorphous trace-metal rich pyrites in barite substrate (Fig.6.19d) and colloform banded masses of amorphous pyrite rimmed by a white lamination of galena (Fig.6.19b,e). The “bright” cores in BSE are enriched in Sb. Also we observed metastable stages of colloidal pyrite to euhedral pyrite: Concentrically laminated Sb-rich pyrite spheroids (pyrite 1) overgrown by microcrystalline masses (pyrite 3) (dark grey) in barite substrate (Fig.6.19c,f).

Galena (PbS) is nearly always associated with pyrite, either as inclusion in colloform masses of pyrite (Fig.6.19a), either as a thin layer mantling the pyrite spheroids (Fig.6.19b,e)) or isolated galena at grain contacts (Fig.6.19 c). Most galena grains are white subhedral to euhedral and typically less than a few tens of μm in size.

Sphalerite (ZnS) has not be detected by SEM.

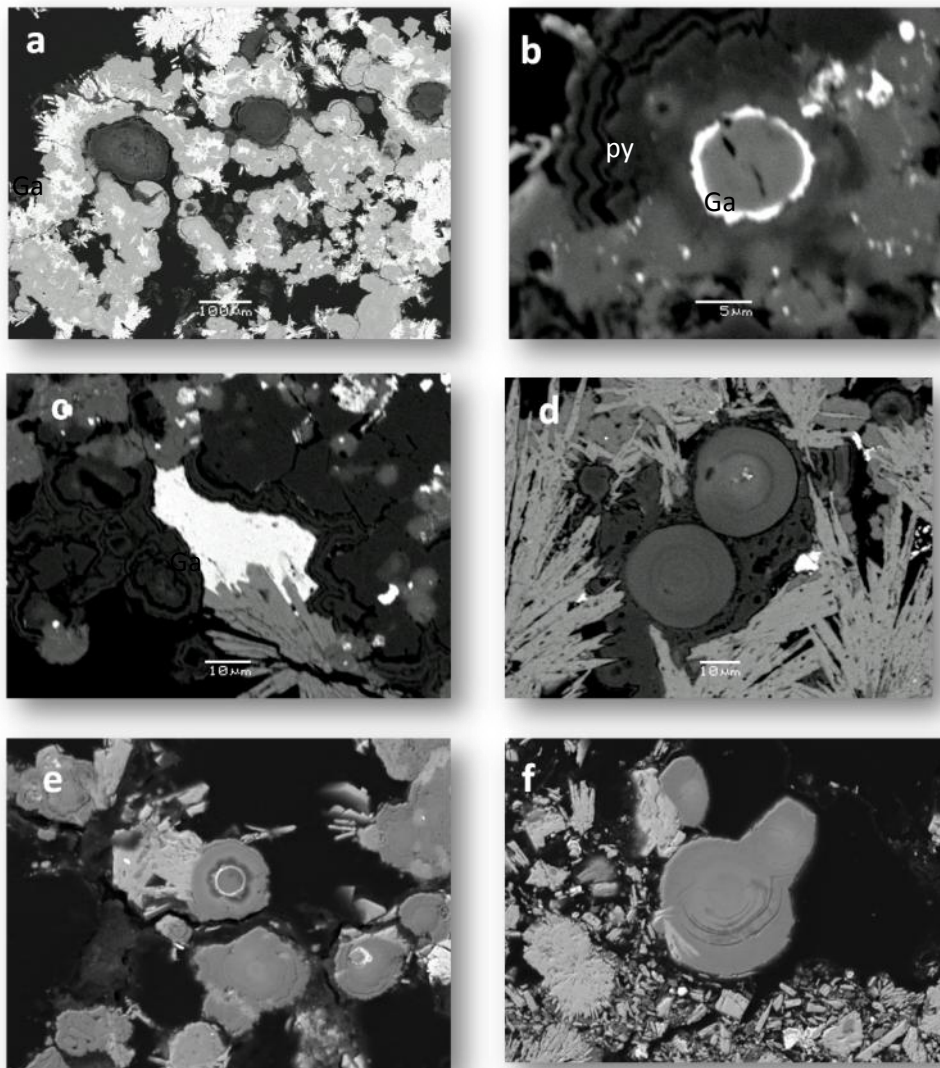


Fig.6.19 SEM backscatter images of anonymous vent (NA014-016) mineral phases.(a) Inclusions of galena in colloform banded masses of pyrite (b) Colloform banded masses of amorphous pyrite rimmed by a white lamination of galena .Antimony is mostly concentrated in the core (light grey) relative to rim (confirming by SEM).Dark grey zones showing oscillatory zoning. (c) Concentrically laminated Sb-rich pyrite spheroids overgrown by microcrystalline masses (pyrite 3) (dark grey), intergrowth with galena (white) (d) Colloform banded masses of amorphous trace-metal rich pyrites in barite substrate. The “bright” cores in BSE are enriched in Sb (e) Colloform banded masses mantled by a white lamination of galena (PbS) (f) Pyrite spheroid (generation 1) overgrown by microcrystalline masses of pyrite (generation 3) in barite substrate.

Antimony in Anonymous Vent

SEM-EDS data show that colloform banded trace element- rich zoned pyrite show oscillatory zoning; zones “bright” in BSE are enriched in Sb (up to 11 wt%), and/or Pb, As and Si (Fig.6.20).Preliminary SR μ -XRF elemental maps confirmed that Sb is mostly concentrated in the core relative to rim (Kilias et al., 2013b)(Figs. 6.20, 6.21) and show that Pb may be concentrated in thin layer of galena (PbS) mantling the pyrite spheroids (Kilias et al., 2013b) (Fig. 6.21).

SEM-EDS spectrum showing significantly high amount of Sb, Pb, Cu, Zn in core of colloform pyrite(Fig.6.22). Also in figure 6.23 an element profile across the colloform pyrite spheroid shows chemical growth zoning defined by Pb-Sb variations in the pyrite composition (up to 14wt% and 6wt% respectively) mantled by galena (up to 3 wt% Sb) and overgrown by microcrystalline masses of pyrite with inclusions of galena (Sb is not detected) (generation 2). Also its detected Ag and Cu into pyrite spheroid (up to 1.5-2 wt%).

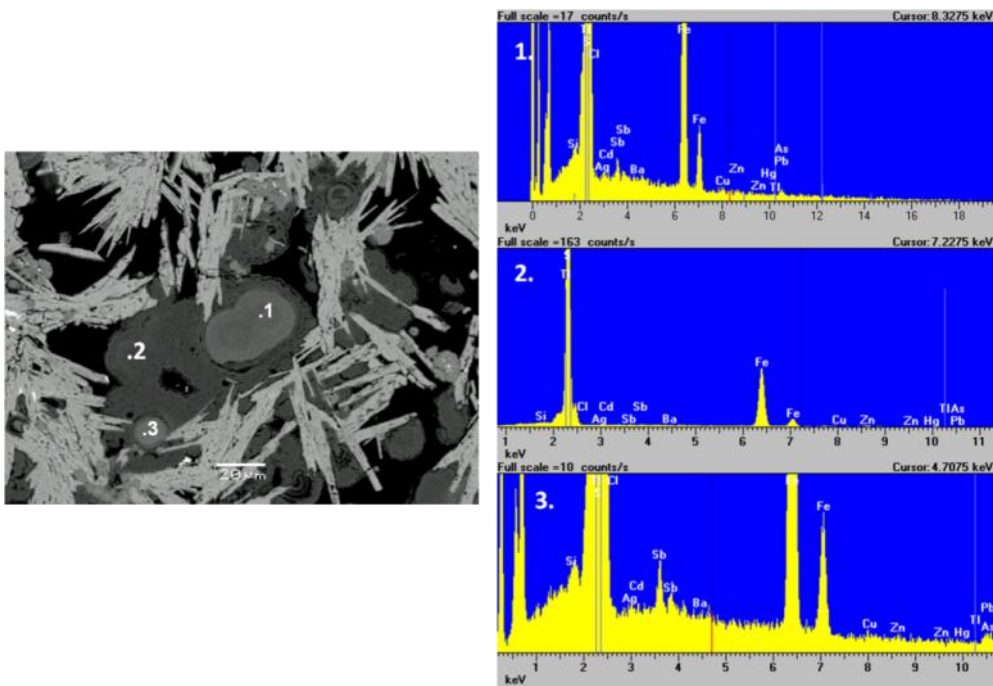


Fig.6.20 (a) SEM-EDS photomicrograph shows colloform banded masses of amorphous trace-metal rich pyrite mantled by barite blades. (b) Spectrum diagrams show that core, "bright" zones in BSE, is enriched in Sb (up to 11 wt%), and/or Pb, As and Si (spectrum 1,3)

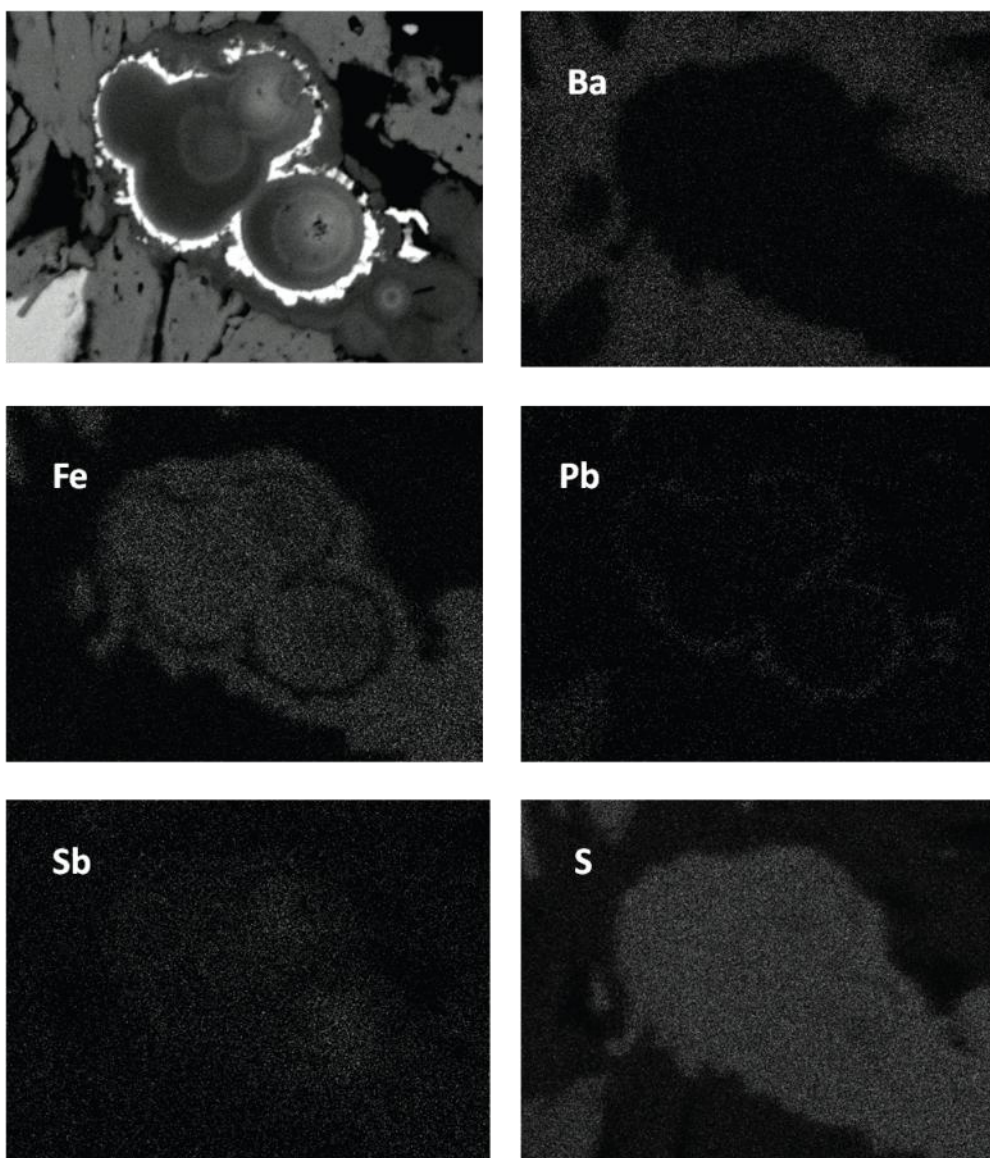


Fig.6.21 SEM-EDS elemental maps for Ba, Fe, Pb, Sb and S show that Pb may be concentrated in thin layer of galena (PbS) mantling the pyrite spheroids (Kilias et al., 2013 b).

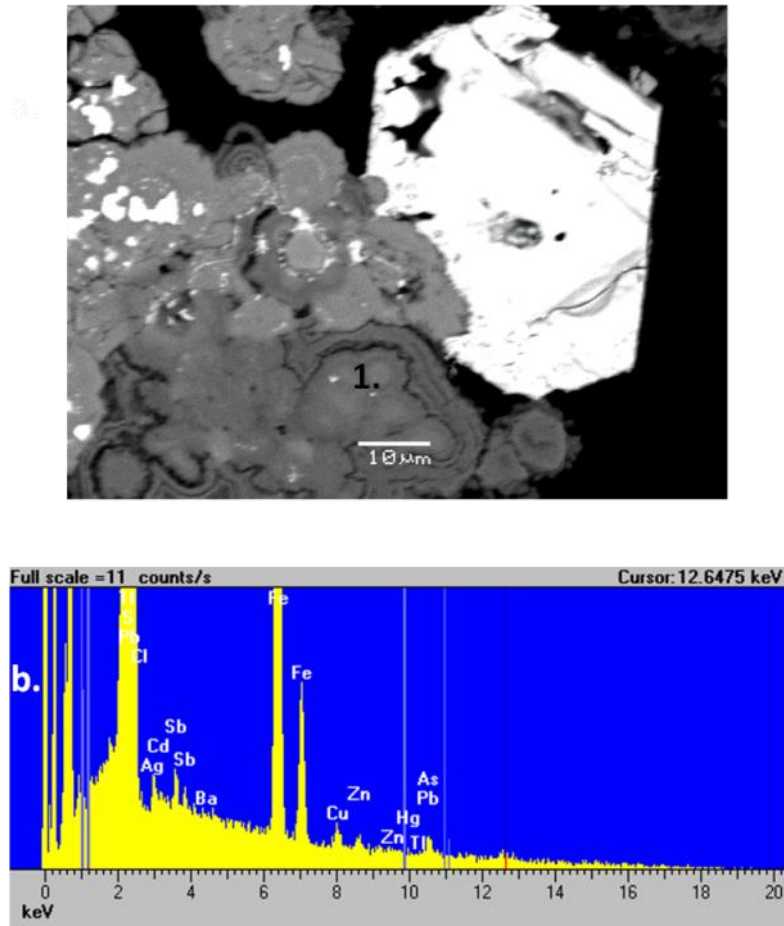


Fig.6.22 Anonymous Vent (AV) sample NA014-016 (ISSC): (a) BSE image of colloform overgrowths with trace metals-rich cores (light grey) interpreted as colony of pyrite in association with galena (b)SEM-EDS spectrum showing significantly high amount of Sb, Pb, Cu, Zn in core of colloform pyrite.

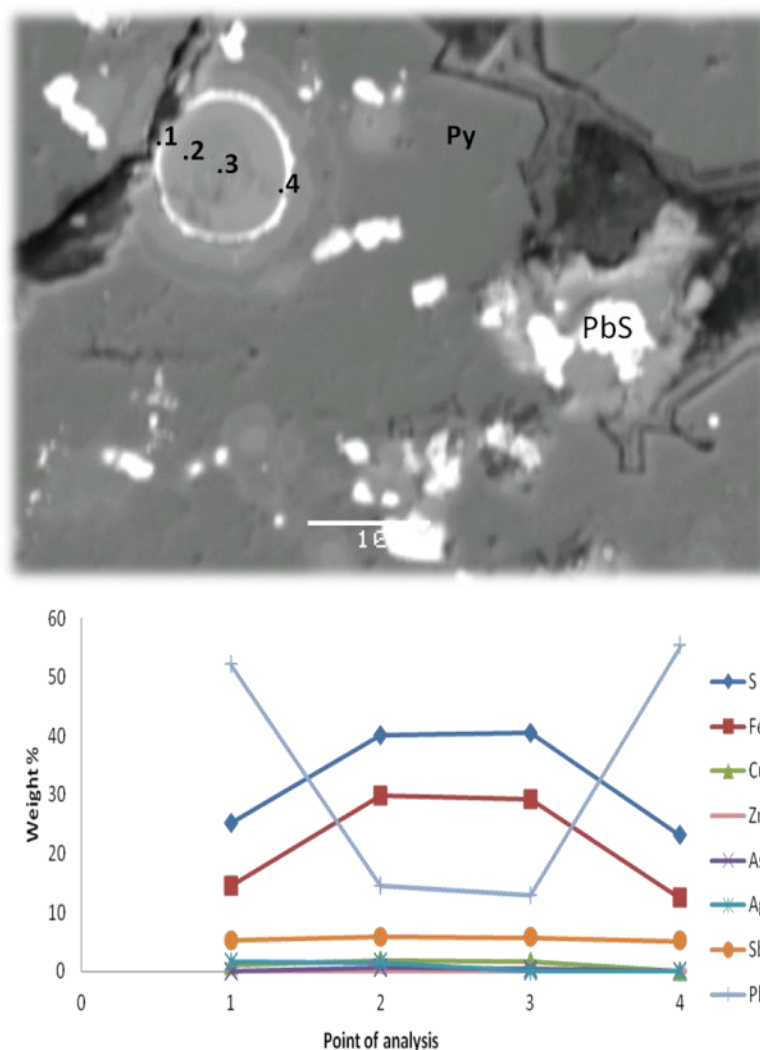


Fig.6.23 Anonymous Vent (NA014-016): (a) Backscattered electron (BSE) image of concentrically laminated trace-metal (Sb, Pb) rich pyrite spheroid (generation 1) overgrown by thin white lamination of galena and overgrown by microcrystalline masses of pyrite (generation 2) with white inclusions of galena (3 wt% Sb). (b) Element profile across the pyrite spheroid. (Numbers on x-axis refer to analysis points). Pyrite shows chemical growth zoning defined by Pb-Sb variations in the pyrite composition (up to 14wt% and 6wt% respectively) mantled by galena (up to 3 wt% Sb). Also its detected Ag and Cu into pyrite spheroid (up to 1.5-2 wt%).

6.2 Bulk Geochemistry of the Kolumbo chimneys

6.2.1 Major and trace elements

The results of chemical analyses of six samples analysed during the present research presented are in Tables 6.1, 6.2. The samples were analysed in order to examine differences in the bulk chemistry of the outer crust and the inner part of the chimneys. Specifically, crust

samples from Politeia and Poet's Candle as well as composite samples from Politeia, Diffuser II and Poet's Candle were analysed. Sulfur, Fe, Ba, Si, Pb, Zn, Sr are major elements (concentrations >1 wt%) in the samples occurring mainly in crystalline pyrite, barite, galena and sphalerite, as well as K-Mg-Al-silicate, and/or Al-K-Fe-sulphate, phases.

Average base metal and maximum concentration for all the mineralized samples are 0.142 wt% Cu (max: 0.40 wt %, n=13), 0.44 wt% Zn (max: 1.78 wt%, n=9) and 1.922 wt% Pb (max: 5.57 wt%). Maximum concentrations of Cu were measured in "Champagne", "Difusser II" and "Poet's candle" (0.19 wt%, 0.14 wt% , 0.40 wt% respectively). Combined Zn + Cu + Pb for these samples is on average less than are 6.15 wt%, which is relatively low comparing with other seafloor sulphide deposits (Hannington et al., 2005) and that maybe indicate relatively low vent fluid temperatures at Kolumbo. Trace elements usually associated with high-temperature hydrothermal activity, such as Se and Mo, are below their detection limit.

However, the average and maximum concentrations of Tl (1000 mg kg^{-1}) and Sb (8010 mg kg^{-1}) are the highest reported from modern seafloor hydrothermal systems (Kilias et al., 2013 supplementary Fig.S4). According to Kilias et al., (2013), Sb, Pb, Au, and Ag present high positive correlation coefficients (similarity level=79.2).

Table 6.1. Major elements content (wt % except Ba in ppm) of hydrothermal vent samples from the Kolumbo deposits

	MDL	NA014-003 CRUST	NA014-039 CRUST	NA014-016 CRUST	NA014-016	NA014-007	NA014-005
SiO ₂	0.01	3.15	0.92	0.23	0.06	3.89	0.19
Al ₂ O ₃	0.01	0.28	0.18	0.06	0.03	1.52	0.05
Fe ₂ O ₃	0.04	6.39	1.83	29.49	43.73	22.41	30.41
MgO	0.01	0.12	0.4	0.09	0.05	0.28	0.08
CaO	0.01	0.29	0.61	0.27	0.04	0.17	1.36
Na ₂ O	0.01	0.8	2.37	0.58	0.19	1.18	0.61
K ₂ O	0.01	0.11	0.09	0.02	<0.01	0.12	0.04
TiO ₂	0.01	<0.01	<0.01	<0.01	<0.01	0.03	<0.01
P ₂ O ₅	0.01	<0.01	0.02	<0.01	<0.01	<0.01	0.02
MnO	0.01	<0.01	0.27	0.01	0.01	<0.01	0.01
Cr ₂ O ₃	0.002	0.003	0.003	0.003	0.005	<0.002	0.003
TOT/C	0.02	0.07	0.18	0.06	0.03	0.08	0.03
TOT/S	0.02	17.25	13.12	30.14	38.2	25.31	31.04
LOI		7.8	4.9	21.4	24.8	27.3	18.9
Ba	1	>50000	>50000	>50000	>50000	>50000	>50000

Table 6.2. Minor elements content (in ppm) of hydrothermal vent samples from the Kolumbo deposits.

	MDL	NA014-003CRUST	NA014-039CRUST	NA014-016CRUST	NA014-016	NA014-007	NA014-005
Pb	0.1	>10000	6630	>10000	3662	19700	42500
Zn	1	>10000	2217	>10000	17800	3900	1210
Sb	0.1	>2000	1820	>2000	5680	8010	4650
Hg	0.01	>50	>50	>50	>50	>50	>50
Sr	0.5	23278	38061	26246	6057	10513	18476
As	0.5	2077	785.3	3108	3549	1451	2455
Tl	0.1	930	64.4	418.1	172.3	381.3	469.3
Ag	0.1	93.6	74.9	>100	>100	>100	>100
Cu	0.1	52.7	54.2	3077	4029	909.7	1349
Cd	0.1	49.2	11.4	227.9	466.3	133.7	101.3
Mo	0.1	9.5	17.8	39.7	15.9	86	22.2
Rb	0.1	3.7	1.5	0.5	<0.1	2.3	1.2
Ni	0.1	2.6	0.4	4.6	4.7	12.9	2.1
Zr	0.1	2.4	2.4	1.1	0.3	18.4	0.7
Au	0.0005	1757	0.7571	11473	15573	1653	11688
W	0.5	1	0.8	<0.5	<0.5	1.1	<0.5
Se	0.5	0.7	<0.5	4.1	4.3	13.3	<0.5
Cs	0.1	0.6	<0.1	0.1	<0.1	0.3	<0.1
Ta	0.1	0.6	0.3	0.1	0.2	1.7	0.3
Ga	0.5	0.5	<0.5	6.3	17.7	8.2	2.1
Nb	0.1	0.4	0.2	<0.1	<0.1	1.6	<0.1
U	0.1	0.4	0.9	0.5	<0.1	2.3	<0.1
Y	0.1	0.4	1	<0.1	<0.1	2.2	0.2
Hf	0.1	0.2	0.4	<0.1	<0.1	1.2	0.7
V	8	<8	40	<8	<8	12	<8
Ni	20	<20	<20	<20	<20	<20	27
Sc	1	<1	<1	<1	<1	<1	<1
Be	1	<1	1	2	<1	<1	<1
Sn	1	<1	<1	1	4	<1	<1
Co	0.2	<0.2	0.6	<0.2	<0.2	1	<0.2
Th	0.2	<0.2	<0.2	<0.2	<0.2	1.5	<0.2
Bi	0.1	<0.1	<0.1	<0.1	<0.1	3.1	0.1

6.2.2 Rare earth elements geochemistry

REEs in the sulfides mainly originate from the hydrothermal fluids and thus express their patterns (Tao et al., 2011) The REE geochemistry of metalliferous sulfides is generally

considered as an indicator for the source and evolution processes of hydrothermal fluids (**Tao et al., 2011**). The REE contents analysis results and characteristic parameters for 13 subsamples from chimneys are shown in Table 6.3, 6.4. As shown in Table 6.3, different types of hydrothermal deposits samples have large difference in REE contents. REE content (Σ REE) of hydrothermal sulphides of Kolumbo (HVA) have a range from 6.34 and 16.71 ppm higher than those of hydrothermal sulphides of southwest Indian Ridge (1.01 ppm) (SWIR) and of black smokers samples of Brothers Volcanoes (1.91ppm) (Kermadic Volcanic arc); and lower than Hydrothermal manganese crusts from Palinuro seamounts (36.262 ppm)(back arc basin in the Tyrrhenian Sea). Σ REE generally increase in profiles across the chimney wall from the dense interior portions to the loose outer ones, reflecting the different mixing proportions of the hydrothermal fluid with seawater (**Zeng et al., 2001**). Chondrite-normalized REE patterns show significant positive Eu anomalies and LREE enrichment, inheriting the characteristics of hydrothermal fluids and suggesting that the REE in sulphides maybe mainly derived from hydrothermal fluids (**Cao et al., 2012**).

The REE Chondrite-normalized distribution patterns for 13 subamples of Kolumbo chimneys are presented in Figs. 6.24, 6.25, 6.26, 6.27. Nearly all the analyzed chimney samples contain clear positive chondrite normalized Eu anomalies, i.e. Politeia vent field (Fig. 6.25), Diffuser II (Fig. 6.27) and Poet's candle (Fig. 6.28), except for those from Champagne active mounds (Fig.6.26) which contain negative Eu anomaly .In figure 6.28 its obvious a binary plot of $(\text{Ce}/\text{Ce}^*)_{\text{SN}}$ against $(\text{Pr}/\text{Pr}^*)_{\text{SN}}$ to distinguish between anomalous Ce_{SN} and La_{SN} behavior for the samples of the Kolumbo chimneys (**Bau and Dulski, 1996**). Ce depletion in relation to the other REEs , supports anoxic depositional conditions. Sedimentary Ce levels are generally expected to increase under oxidizing conditions because, unlike most REEs, Ce^{3+} is oxidized to Ce^{4+} and coprecipitated in association with iron oxyhydro (oxides). Most analyzed Kolumbo samples contain no positive Ce anomalies, except for 4 samples having negative Ce anomalies. This trend in Ce anomalies indicates that the samples formed in low oxygen suboxic to anoxic conditions (**Planavsky, et al., 2009, Tao et al., 2011, Bau et al., 2013**).

Table 6.3. REE concentrations in ppm (mg kg^{-1}) and chondrite normalized properties of REE enrichments and REE fractionation ratios of hydrothermal vent samples from the Kolumbo deposits analysed and seafloor hydrothermal deposits from various tectonic settings : Brothers Volcano (de Ronde et al., 2005); Tyrrhenian Sea Palinuro (Eckhardt et al., 2008), Galapagos rift (Tao et al., 2011).

Elements (ppm)	MDL															Brothers	Palinuro	Galapagos rift
		NA014-003CRUST	NA014-039CRUST	NA014-016CRUST	NA014-016	NA014-007	NA014-005	NA014-003-ISSC	NA014-003-OAsL	NA014-003-SFeC	NA014-027	NA014-028	NA014-039-ISSC	NA014-039-SFeC				
La	0.1	7.2	6.2	3.4	1.8	6.8	4.3	3.9	5.4	5.4	5.9	4.1	4,0	6.1	0.5	6.64	0.2	
Ce	0.1	3.4	4.8	2.3	0.6	5.9	1.1	1.9	1.8	3.7	5.4	2.6	1,0	5.3	0.39	14.94	0.449	
Pr	0.02	0.3	0.37	0.22	0.12	0.47	0.12	0.13	0.08	0.23	0.43	0.16	0.06	0.3	0.062	1.714	0.049	
Nd	0.3	0.7	0.8	0.3	0.3	1.6	0.3	0.7	0.3	0.3	0.6	0.6	0.3	0.7	0.31	6.231	0.17	
Sm	0.05	0.45	0.52	0.25	0.07	0.23	0.58	0.13	0.05	0.51	0.45	0.05	0.08	0.23	0.04	1.197	0.034	
Eu	0.02	1.58	2	1.72	2.86	0.02	3.19	0.18	0.02	0.02	0.02	0.02	0.02	0.02	0.29	0.47	0.009	
Gd	0.05	1.61	1.24	0.76	0.66	1.18	1.77	0.81	3.04	1.82	1.35	1.51	0.56	2.86	0.043	1.464	0.026	
Tb	0.01	0.04	0.05	0.03	0.03	0.07	0.04	0.02	0.05	0.04	0.06	0.05	0.02	0.08	0.03	0.201	0.004	
Dy	0.05	0.05	0.05	0.05	0.05	0.05	0.05	0.05	0.21	0.05	0.17	0.05	0.05	0.05	0.075	1.273	0.025	
Ho	0.02	0.03	0.05	0.02	0.02	0.04	0.02	0.1	0.14	0.21	0.16	0.15	0.06	0.28	0.03	0.253	0.005	
Er	0.03	0.03	0.03	0.03	0.03	0.14	0.03	0.17	0.24	0.47	0.33	0.31	0.12	0.48	0.047	0.783	0.017	
Tm	0.01	0.04	0.03	0.01	0.01	0.04	0.02	0.01	0.01	0.02	0.02	0.02	0.01	0.02	0.03	0.18	0.003	
Yb	0.05	0.05	0.08	0.05	0.05	0.14	0.03	0.05	0.06	0.06	0.26	0.14	0.05	0.22	0.04	0.766	0.015	
Lu	0.01	0.01	0.01	0.01	0.01	0.03	0.01	0.01	0.01	0.03	0.02	0.01	0.01	0.02	0.03	0.1366	0.004	
ΣLREE		13.63	14.69	8.19	5.75	15.02	9.59	6.94	7.65	10.16	12.8	7.53	5.46	12.65	1.592	31.2	0.91	
ΣHREE		1.86	1.54	0.96	0.86	1.69	1.97	1.22	3.76	2.7	2.37	2.24	0.88	4.01	0.32	5.06	0.099	
ΣREE		15.49	16.23	9.15	6.61	16.71	11.56	8.16	11.41	12.86	15.17	9.77	6.34	16.66	1.917	36.26	1.01	
$[\text{Ce}/\text{Ce}^*]_{\text{NASC}}$		0.313	0.504	0.45	0.212	0.535	0.172	0.309	0.226	0.464	0.605	0.409	0.167	0.57	0.403	1.026	1.059	
$[\text{Eu}/\text{Eu}^*]_{\text{NASC}}$		7.578	11	17	38.97	0	13.39	19.00	0.064	0.084	0.109	0.127	0.31	0.064	34.03	1.722	1.454	

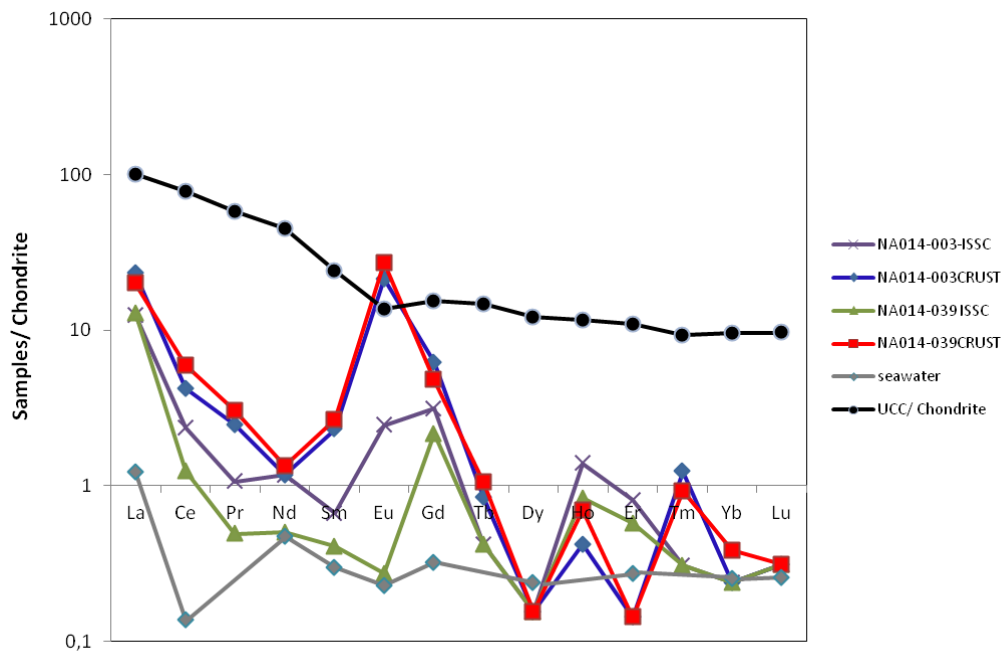


Fig.6.24 Chondrite-normalized REE patterns for representative samples of Politeia Vent Field (NA014-003 ISSC, NA014-003 CRUST, NA014-039 ISSC, NA014-039 CRUST, NA014-016 CRUST), compared to Upper Continental Crust (UCC)(black) and seawater (Tanaka. et al., 1990)

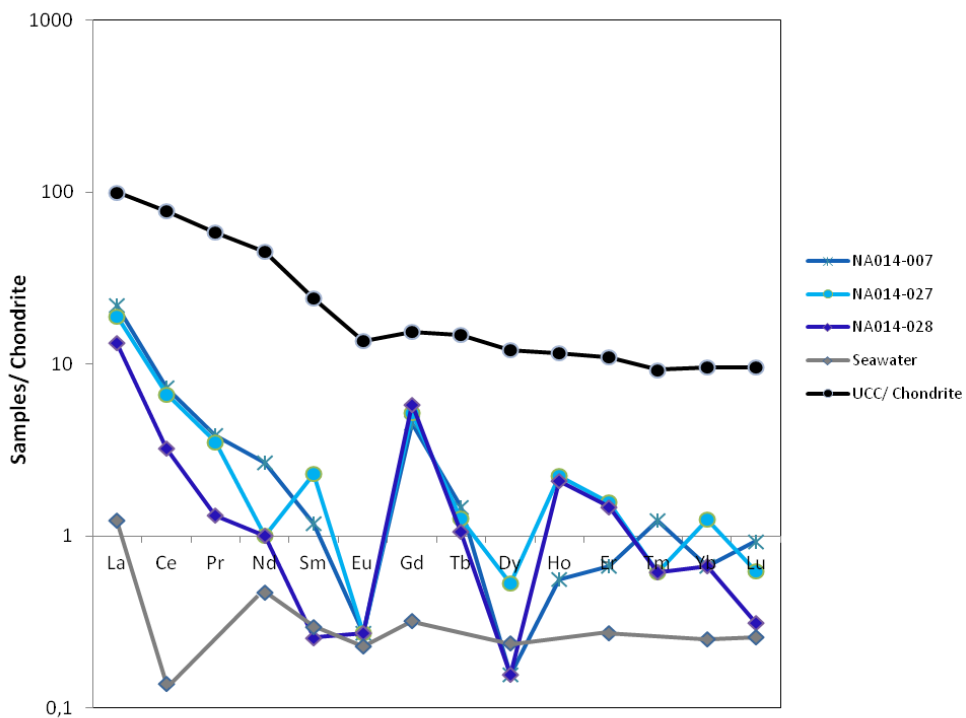


Fig.6.25 REE abundance patterns normalized to chondrite for Champagne's samples (NA014-007,NA014-027,NA014-028), the Upper Continental Crust (UCC)(-in black) and seawater (Tanaka. et al., 1990)

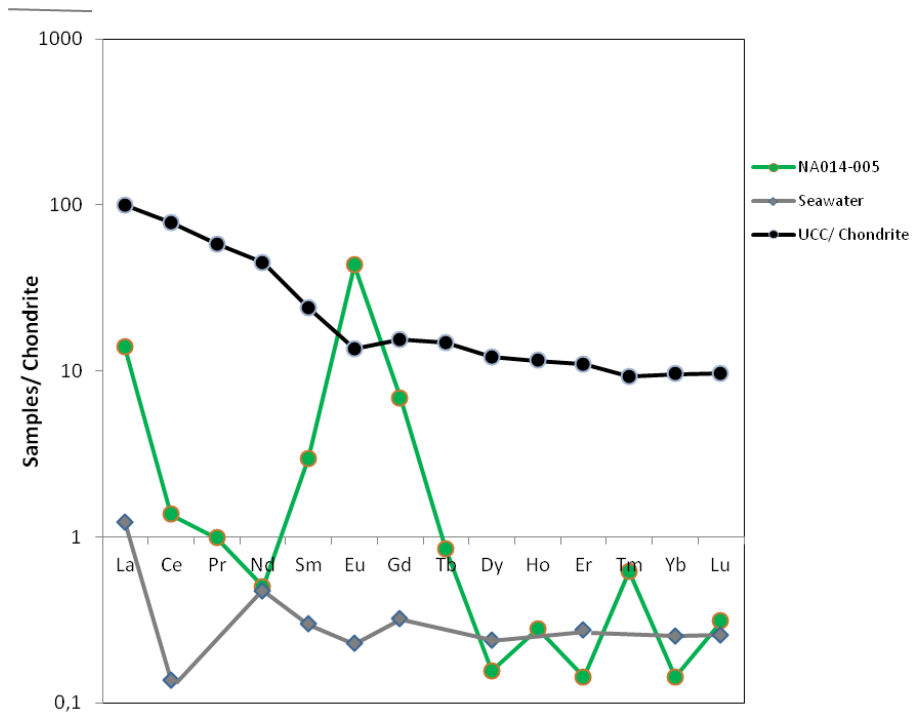


Fig.6.26 REE abundance patterns normalized to chondrite for Diffuser's sample (005) and the Upper Continental Crust (UCC)(-in black) and seawater(Tanaka. et al., 1990).

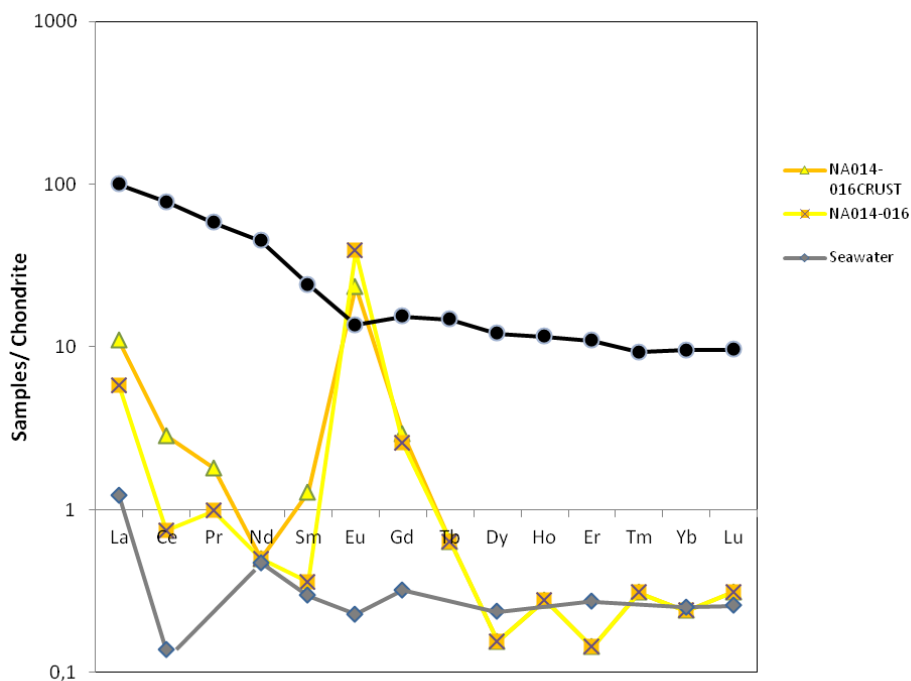


Fig.6.27 REE abundance patterns normalized to chondrite for AV sample (NA014-016) and the Upper Continental Crust (UCC) (-in black) and seawater (Tanaka. et al., 1990)

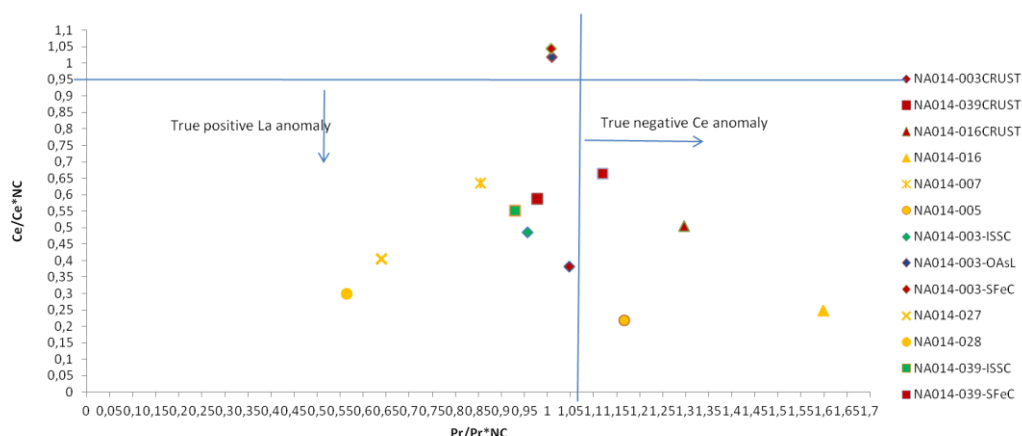


Fig.6.28 Binary plot of $(Ce/Ce^*)_{SN}$ against $(Pr/Pr^*)_{SN}$ to distinguish between anomalous Ce_{SN} and La_{SN} behavior for the Samples of the Kolumbo chimneys (after Bau and Dulski, 1996).

6.2.3 Partitioning of elements in extractable phases

Data quality control, based on calculation of elemental recoveries by summing concentrations in all steps and comparing them to the aqua regia dissolution results, indicated that further quantitative interpretation of the results would not be valid. However, results are presented and discussed on a qualitative basis by comparing the relative extractability of Tl, As and Sb in the sequential extraction steps. The results for the 5 analysed samples are illustrated in Figure 3.30.

The fractionation of the three examined elements varies in the different extraction steps. Arsenic and especially Sb (Figure 3.30) present the highest extractability in the final step i.e. the residual phase, while Tl seems to be more easily mobilized and presents higher extractable proportions in the first extraction step. Arsenic displays higher extractability than the other two elements in the reducible phase fraction probably indicating the higher affinity of this metalloid to Fe-oxides and hydroxyoxides. Comparing the crust and the core of the samples in Fig.5b it is obvious that the concentration (%) of Sb and As in crust is higher than in core, which is expected because samples designated as "crust" contain higher amounts of Fe-oxides compared to those designated as ISSC. The highest extractability in the residual step is clearly observed for Sb. This is in agreement with the mineralogical study which indicated that Sb is abundant in the solid sulphide phases of the chimneys. However, the presence of Sb in the reducible phase fraction, especially of the sulphide 'crust' samples, indicates that part of this metalloid is fixed by the Fe-oxyhydroxide phases. This is also confirmed by the SEM-EDS study of the Politeia 'crust' sample.

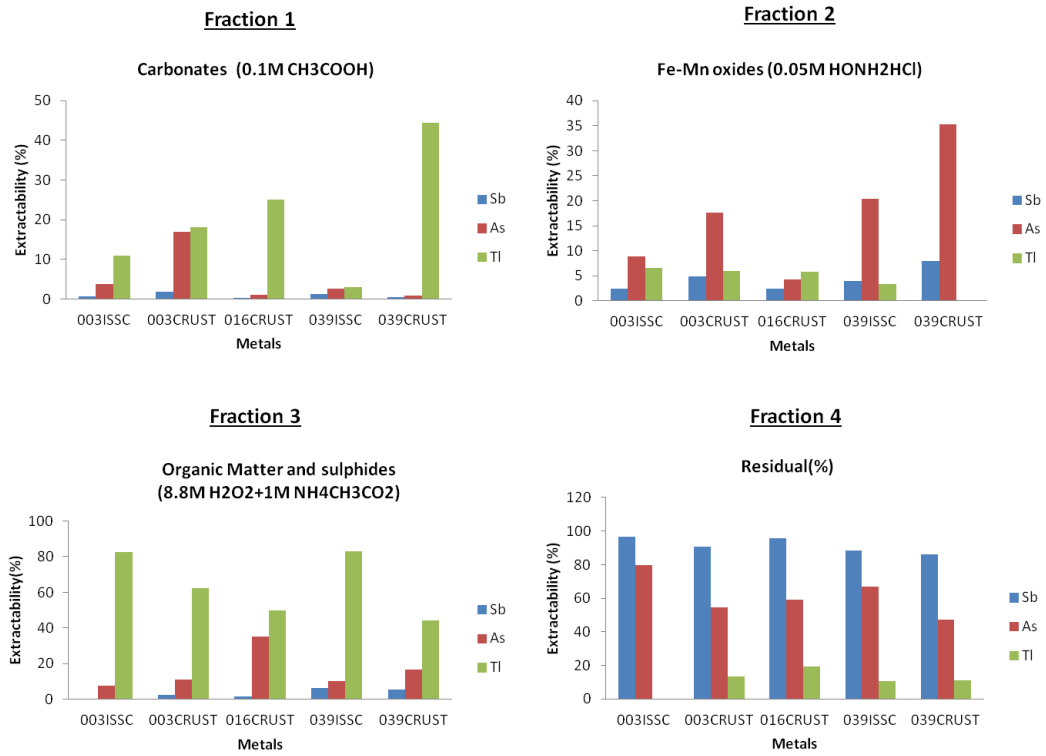


Fig.6.29 Extractability order of the studied elements in each extraction stage of the BCR sequential extraction procedure and residual phase for 5 samples.

7. Discussion

7.1 The Kolumbo polymetallic seafloor hydrothermal chimneys

Vent structures, style of venting, mineral zoning and growth history

The studied Politeia samples constitute parts of diffusely venting polymetallic structures which show extensive growth in the absence of well-defined throughgoing open conduits character of black smokers (see **Tivey et al., 2007**). Consequently, flow within Politeia chimneys occurs through an anastomosing, discontinuous network of narrow, tortuous flow channels and a highly permeable, sponge-like matrix of sulfide, sulphosalt and sulphate. Also the studied Champagne, Diffuser II and Anonymous Vent (AV) samples constitute parts of smooth-sided sulphide sulphate mounds with no spire structures, commonly discharge streams of bubbles, mainly CO₂, from small holes and cracks on their sides and bases (**Kilias et al., 2013a**).

Fine-scale chemically zoned minerals (Figs. 6.6, 6.7, 6.11, 6.16, 6.23) and selective partitioning of trace metals (i.e. Sb, Pb, As) in successive generations of mineral phases, i.e. pyrite types 1-3 (There is lack of zoning in pyrite 2 and 3)(Figs.6.6, 6.7,6.8) in the various broad scale mineralogical zones (i.e. Politeia, ISSC, OAsL, SFeC, IPNC)(Fig.5.1b)(**Kilias et al., 2013a**) reveal a complex growth history for the Kolumbo chimneys and numerous processes which may involve: (i) highly localized fluid compositions, (ii) extensive replacement of earlier formed minerals, (iii) episodic ingress of seawater, (iv) flange development or parasitic chimneys, (v) numerous precipitation events, and, (vi) sustained, broad-scale outflow of warm fluids from the walls through a porous and permeable matrix (**Kristall et al., 2006**).

Geochemical microenvironments

The observed micrometer-scale zonation of mineral phases with variations in trace elements within a larger mineralogical zones (ISSC, OAsL, SFeC, IPNC) (Fig.5.1) in diffuser chimneys of Politeia samples and sulphide-sulphate mounds indicate different chemical microenvironments (**Kristall et al., 2011**). Some examples of mineral zoning of Kolumbo hydrothermal vent samples are:

- Chemical growth zones of pyrite 1 defined by high Sb and Pb composition of fine light in BSE laminae (Sb up to 9.08 wt% and Pb 11.53 wt%)and dark in BSE laminae (Sb up to 2.13wt%, As and Pb are not detected). Arsenic enrichment (As up to 1.84 wt%) in pyrite 2.(Antimony is not detected in pyrite 2 and 3) (Fig.6.6).

- Enrichment of light in BSE laminae in Sb (up to 16wt %) in colloform orpiment (As_2S_3) of OAsL (Fig.6.11). Antimony is not detected in dark in BSE laminae.
- Chemical growth zoning defined by Cu enrichment (up to 1.66 wt%) in colloform banded pyrite of Champagne (Fig.6.16). Antimony is not detected.
- Chemical growth zoning defined by Sb-Pb enrichment in the pyrite composition along light BSE zones (up to 6wt% and 14wt% respectively) and Ag and Cu into pyrite (up to 1.5-2 wt%) of anonymous vent .

The various enrichment or depletions of trace elements in the sulphide mineral phases indicate variable conditions of temperature, redox, or mixing, offer a means to better identify physical and chemical microenvironments within diffusely venting (e.g., **Butler and Nesbitt, 1999; Kristall et al., 2006; 2011**). Distinct chemical microenvironments within sulphides structures and within different mineralogical zones provide a basis for detailed reconstruction of the variable physico-chemical conditions of deposition in the chimneys portions, which may not be immediately apparent from the bulk mineralogy (e.g. **Kristall et al., 2011**).

According to **Kristall et al., (2011)** the description of microenvironments within chimneys may contribute to improved understanding of geomicrobiological processes at seafloor hydrothermal vents. The range of possible microbial habitants that develop within chimney structures during their growth may includes strong redox and temperature gradients.

7.2 Source of antimony

It has generally been assumed that only Sb^{3+} complexes are important for antimony transport in hydrothermal systems. However a recent study investigated the nature of Sb (V) complexes in alkaline sulfide–chloride brines at temperatures from 25 °C to 300°C at Psat, using in situ X-ray absorption fine structure (EXAFS) spectroscopy and suggested that under alkaline conditions Sb^{5+} sulfide complexes may be stable under conditions as reducing as those found in hydrothermal ore solutions (**Sherman et al., 2000**). In case of the Kolumbo hydrothermal system, it is believed that mixed hydroxy-chloride complexes $\text{Sb}(\text{OH})_3\text{Cl}^-$ may control Sb^{3+} transport, because the highest vent temperature that was measured in 2010 was 210°C at acidic conditions (pH~5) and according to thermodynamic calculations by **Prokovski et al. (2006)**, Sb^{3+} speciation in hydrothermal fluids is represented by $\text{Sb}(\text{OH})_3$ and

$\text{Sb}(\text{OH})_3\text{Cl}^-$ existing in comparable amounts at moderate temperatures below 300°C and acidic conditions ($\text{pH}>3$).

The occurrence of Pb-Sb sulphosalts and Sb-rich colloform pyrite/marcasite in close association with hydrothermal minerals (barite) at Kolumbo active seafloor hydrothermal site suggests they are genetically linked to hydrothermal antimony input (**Dekov et al., 2013**). The studied samples except for extreme Sb enrichment (Fig. 3.9) also show epithermal suite geochemical association and enrichment (Au, As, Sb, Hg, Ag, Tl, Ag) (**Kilias et al., 2013a**). The latter is characteristic of subaerial epithermal and Carlin-type continental deposits and has recently been suggested to result from their similar volatile behaviour in subduction systems (**Saunders et al., 2012**). Therefore, it can be ascertained from the data available that Sb, and other metals (i.e. Pb, Zn, Fe, etc) were introduced from below by ascending fluids. For the reason that antimony in Kolumbo is of hydrothermal origin, similarly high concentrations would also be expected in other hydrothermal solids along the active and extinct geothermal systems of the Hellenic Volcanic Arc; however, with the exception of Milos Fe-rich hydrothermal sediments which contain up to 2,000 ppm (**Tao et al., 2013**) similar enrichments have not been found (**Varnavas et al., 2005**). Therefore, the types of rocks that were leached by the hydrothermal fluids on their way to the seafloor may be important.

The extreme enrichment of hydrothermal fluids in Sb, as well as high enrichment in Fe, Zn, Cu, As, Pb, Sb, Au, Ag, Tl, Hg and Ba, may suggest leaching of an underlying polymetallic Carlin-type carbonate-hosted mineralization. This is in harmony with the geological setting and geodynamic evolution of Santorini-Kolumbo volcanic field, as well as geochemical characteristics of Kolumbo mineralization which share similarities with the pertinent characteristics of Carlin-type carbonate hosted mineralization in Nevada (**Kilias et al., 2013; Muntean et al., 2011**): (i) Geodynamic setting corresponding to a change from compression to extension and renewed magmatism; (ii) association with old, reactivated basement rift structures, and occurrence in carbonate-bearing rocks within or adjacent to structures in the lower plate of a regional thrust, (iii) Similar ore paragenesis and ore signature is Au–Tl–As–Hg–Sb–Ag and base metals (Zn, Pb); (iv) ore fluids ranged from ~180 to 240 C and were CO₂-bearing (<4 mol %) and acidic; (v) Formation depth <3 km.

7.3 Antimony fixation in seafloor hydrothermal solid phases

The observed metal enrichments (Figs. 6.6, 6.7, 6.11, 6.13, 6.14, 6.18, 6.20, 6.22, 6.23) also have implications for toxic Sb, as well as, other toxic metals (i.e. Pb, Tl, As, Hg)

transport and biogeochemical cycling in seafloor hydrothermal systems, and underscores the importance of submarine volcanic and hydrothermal activity as sources of toxic metals in the oceans (Kilias et al., 2013a). Antimony fixation in solid phases at submarine hydrothermal vents is essential for reducing the high hydrothermal flux of this toxic element to seawater and is an important part of geochemical Sb-cycle (Dekov et al., 2013). Antimony was detected in all four mineral zones of the Politeia vents (ISCC, OAsL, SFeC, IPCN) and in core and crust of Anonymous Vent (AV) and this was confirmed by the sequential extraction method (Fig 6.29) applied in this thesis demonstrated the selective enrichment of Sb in sulphide phases of the ISSC (e.g pyrite/marcasite, and sulphosalts), sulphide phase of the OAsL (Orpiment type) ,Fe-oxyhydroxide phases of the SFeC and Sb-Zn-S phases of IPCN and in sulphide phase of Anonymous Vent (AV), in accordance with our mineralogical findings (Fig. 6.6,6.7, 6.11, 6.14, 6.23). Also the antimony forms either autonomous antimoniferous sulphosalt phases, or is selectively partitioned in pyrite/marcasite of Champagne samples (Fig.6.15) and of Diffuser II (Fig. 6.18).

Deciphering the mechanisms of trace metal incorporation, as well as origin and significance of growth/oscillatory zoning, is a very important issue because it has implications for the recovery of metals (i.e. Sb, Au) during mineral processing, and the release of toxic amounts in the environment (i.e. ocean waters); moreover, because of the spatial scale at which microbes function, delineation of different chemical microenvironments within chimneys may contribute to improved understanding of geomicrobiological processes at seafloor hydrothermal vents (Kristall et al., 2011).

This study has demonstrated that antimony and pyrite are tightly related (Figs. 6.6, 6.7, 6.8, 6.23). The combination of synchrotron radiation based μ -XRF elemental mapping, and μ -XAFS spectra at LIII-edge for Sb, confirmed the preferential partitioning of Sb within the Fe-sulphide phase from the ISSC (Kilias et al., 2013). In the samples analyzed here, most of the Sb is present in two different textural positions: (1) invisible Sb (i.e. Sb in solid solution and/or submicroscopic inclusions (nanoparticles) incorporated mostly in concentrically laminated pyrite/marcasite grains; in this case Sb measures up to 8%, and Pb up to 13%, and As up to 0.68 (In Fig. 6.6 As is not detected in pyrite 1), are finely distributed in the grains (Figs. 6.6, 6.7, 6.23)(The negative correlation between S and F, and Sb and Pb, respectively, shown in Figs, 6.6, 6.7 suggests that Sb and Pb may occur in the form of solid solution replacing Fe and S),and, (2) compact Sb-Pb-sulfosalt phases clearly visible in optical microscopy and SEM-EDS (Figs. 6.4 6.5, 6.18). We interpret these findings as suggesting two distinct occurrences of Sb (and Pb) in the Kolumbo chimneys: primary Antimony occurs

either as possible replacement of Sb^{3+} for Fe in the pyrite of ISSC material and secondary Sb hosted in separate Sb-Pb phases. It is known that pyrites may accommodate Sb-ions and Sb-sulphosalt nanoparticles (**Deditius et al., 2011**), but there are no particular studies on the nature of Sb in amorphous Fe-sulfides from recent seafloor hydrothermal fields, unless stibnite is formed.

7.4 Rare earth element distributions

Chondrite normalized REE_N distribution patterns are uniformly light-REE (La–Nd) enriched and show a large positive Eu-anomaly (Figs. 6.24, 6.25, 6.26, 6.27). ΣLREE and ΣHREE contents vary overall from 5.75 to 15.02 ppm, and 0.86 to 4.01 ppm, respectively. Several causes can lead to Eu anomalies, such as hydrothermal fluid overprint, weathering processes, and Ba interference related to ICP-MS analytical techniques (e.g. **Xu et al., 2013**). The Eu anomalies in this study do not seem to be an artifact of Ba interference on Eu because no significant correlation exists between Ba and Eu/Eu^* values. Positive Eu anomalies are typically found in acidic, reducing hydrothermal fluids having temperatures of $>250\text{ }^\circ\text{C}$ (**Bau, 1991**). Massive sulfide ores from the Changba Sedex Pb–Zn deposit (**Xu et al., 2013**) and the Neves-Corvo VMS Cu–Sn (**Relvas et al., 2006**) deposit which show positive Eu anomalies, are believed to have been derived from hydrothermal fluid venting. Stockwork mineralization from the Brunswick No. 12 VMS deposit lacks a negative Ce anomaly and in this respect is similar to reduced modern seafloor hydrothermal vent fluids (**Peter and Goodfellow, 1996**). **Consequently, REE characteristics such as positive Eu anomalies, and lack of seawater REE signature and strong negative Ce anomaly, and a light-REE enrichment, show that Kolumbo solid precipitates are derived from seafloor venting of evolved hydrothermal fluids.**

Moreover, a light-REE enrichment and positive Eu anomaly reflect enhanced mobility of the light-REEs and Eu owing to the predominance of REE chloride complexes in chloride-rich hydrothermal fluids. Local processes, including sub-surface fluid mixing and/or boiling and mineral deposition and remobilization, may also affect REE concentrations of seafloor hydrothermal fluids. However, REE_N distributions of seafloor vent fluids are primarily affected by key aspects of fluid composition (e.g., pH, ligand concentration) that affect REE speciation and mobility during fluid–rock interaction at depth, denoting evolved hydrothermal fluids.

7.5 Genetic model of Sb mineralization and cycling within the Kolumbo chimneys

The NE-SW Christiana-Santorini-Kolumbo (CSK) volcano-tectonic zone provides pathways for subduction-generated magmas to reach the surface of Kolumbo and have been conduits of fluids driven by the high thermal regime (**Nomikou et al., 2012**). These fluids rich in trace elements (As, Au, Ag, Sb, Pb, Tl, Hg, Cu, Zn, Pb) played a key role in the formation of Sb-rich hydrothermal deposits of Kolumbo seafloor studied here. Trivalent antimony form (Sb^{3+}) is by far the dominant oxidation state in volcanic and magmatic-hydrothermal fluids with increasing temperature and depth (**Spycher and Reed, 1989**). In our genetic model (Figs.7.1, 7.2, 7.3,7.4) of the Kolumbo hydrothermal system, mixed hydroxy-chloride complexes ($\text{Sb}(\text{OH})_3\text{Cl}$) control antimony Sb^{3+} transport in saline high-temperature ore fluids at acidic conditions($\text{pH}\sim 5.5$) (see 7.2)(**Prokovski et al.,2006**).

Deposition model

First precipitated episode: Antimony in the ISSC (Fig. 7.1)

Antimony has been dutifully connected with lead (Pb) in every studied sample. Lead belongs to the trace element suite found in pyrite that are typically concentrated by organic matter and during sedimentation and diagenesis of organic-rich sediments in euxinic (sulphur rich) environments (**Large et al., 2009 and references therein**); it forms strong organometallic bonds, which lead to their capture from hydrothermal fluid onto organic matter, on and immediately below the seafloor. The strong positive correlations between Pb and Sb in our dataset of early concentrically laminated pyrite 1 (Figs. 6.6, 6.7), coupled by: (i) High organic matter contents in chimney samples of 3.86% to 5.91% (avg.: 5.30) measured as total organic carbon (TOC)(**Kilias et al., 2013a**) and high biomass of surface-attached microbial mats on the Kolumbo diffuser chimneys (**Kilias et al., 2013a**), (ii) fine laminations and oncolites of pyrite 1(Fig. 6.6, 6.7) indicating organic material-rich marine environment (**Křibek et al., 2007**); and (iii) anoxic depositional environment for pyrite as evidenced by REE data (Figs. 6.24-6.27), strongly suggest that Sb was also initially concentrated by similar organic processes in the Kolumbo chimneys. Moreover, high trace Sb and Pb laminated pyrite is reminiscent of pyrite known to form in suboxic to anoxic environments (i.e. black shales) (**Agangi et al., 2013**).

During hydrothermal diagenesis/maturation, and growth of hydrothermal concentrically laminated pyrite 1, Sb, and Pb, and probably many other trace elements, i.e. Ag Zn, were likely partitioned from the organic matter into the pyrite (**Large et al., 2009**). We speculate that the concentration of Pb in the pyrite is important in controlling the

uptake of Sb into the structure of the pyrite (**Large et al., 2009**). Our data confirmed the preferential partitioning of Sb within the pyrite and the possible dominance of trivalent species Sb^{3+} (Figs. 6.8, 6.9) rather than pentavalent species Sb^{5+} forms, and shows a systematic Sb evolution following the pyrite evolution, i.e. pyrite 1 to pyrite 3 (see Figs. 6.3a, 6.6, 6.7,). Three main stages are recognized.

Stage 1: Early hydrothermal precipitation. It is very likely that the Sb is hydrothermally emitted as the reduced Sb^{3+} form, and initially bonded with organic matter, hence concentrated by organic processes. Subsequently these organo-Sb(Pb) entities may have reacted abiotically with sulfide and/or Fe^{2+} to form Sb^{3+} (Pb)-rich pyrite. At this stage, trace Sb (Pb±As) are “invisible” being locked in pyrite either as (i) nano-scale particles, or (ii) solid solutions within the pyrite structure.

Stage 2: Hydrothermal diagenesis/maturation. This leads to recrystallization of most pyrite 1, and deposition of new overgrown pyrite 2 (Figs. 6.6, 6.7). Some of the Pb, Sb As (and possibly Zn and other trace metals) are released from pyrite 1 during recrystallization to form discrete mineral phases such as galena, sphalerite, and Sb-Pb sulfosalts (Fig. 6.3a, 6.3f). This process of “cleaning” or “refining” the pyrite leads to different trace element ratios between stages 1 and 2 pyrites (Fig. 6.6, 6.7).

Stage 3: Hydrothermal fluid flow late during chimney formation leads to further recrystallization of previous pyrite 1 and 2 types, and: (i) growth of pyrite 3 which is commonly coarse grained, euhedral, and trace element poor (Fig. 6.3a), and, (ii) Pb-Sb sulphosalt overgrowths.

The change in trace element composition of the later hydrothermal pyrites 2 and 3, compared to pyrite 1, is probably due to a number of factors (i) The ability of trace elements to substitute for Fe^{+2} and S^{2-} in the pyrite structure (ii) Metal availability and solubility in the hydrothermal fluid (**Large et al., 2009**). The trace element patterns discussed here and their similarity to Carlin-style deposits, indicate common processes have occurred during pyrite formation (**Large et al., 2009**).

At Kolumbo Pb and Sb are nil in porous spongy pyrite 2 (Figs. 6.6, 6.7), or idiomorphic pyrite 3 (Fig. 6.3a, 6.23). This indicates that the concentrically laminated grains liberated Sb and Pb during hydrothermal diagenesis to form galena, and as yet unidentified Pb-Sb sulfosalt phases (**Ulrich et al., 2011**). From this it appears that postdepositional

overgrowths pyrite 2 and 3 were formed mostly by in situ dissolution and reprecipitation of the pyrite 1 in an environment that was dominated by hydrothermal fluids (**Ulrich et al., 2011**). In contrast to the elements that were mobilized from pyrite 1, As is comparable between pyrite 1 and 2 (Fig. 6.7). As noted by **Huston et al. (1995)**, **Large et al. (2007)**, and others, this element is held strongly by the pyrite, due to the non stoichiometric substitution of Fe by As. The tendency for a trace element depletion in late pyrite compares well with that reported for several ancient massive sulfide deposits (e.g., Yaman-Kasy and Saf'yanovka, South Urals; **Maslennikov et al., 2009**), sediment-hosted Au–As deposits (e.g., Sukhoi Log, Eastern Siberia; **Large et al., 2007**) and Carlin-type deposits (North America; **Large et al., 2009**). In such cases, the trace element depletion of late crystalline pyrite relative to early colloform or framboidal pyrite was explained by the higher temperature and slower growth of the late crystalline pyrite, which allows the trace elements to be partitioned into separate sulphide phases rather than incorporated into pyrite in solid solution or as very small (<5 µm) inclusions (**Large et al., 2009**).

Second precipitated episode: Antimony in the OAsL (Fig. 7.2).

Under different physical and chemical conditions colloform orpiment precipitates. The occurrence of orpiment in close association with hydrothermal minerals (sulphates-barite) at active seafloor hydrothermal sites suggests they are genetically linked to hydrothermal As input. According to **Dekov et al., (2013)** orpiment is stable at low-temperature ($T < 100\text{ }^{\circ}\text{C}$) seafloor hydrothermal conditions, in a wide pH range and orpiment with 0.05 wt% Sb was reported from Kaia Natai Seamount, PNG. According to SEM-EDS antimony in OAsL is selectively partitioned in colloform orpiment (As_2S_3)-type As-sulphide phases, which contains significant amounts of Sb (up to 16wt%), along growth zones which appear “bright” in BSE (Fig.6.11).

Third precipitated episode: Antimony in the SFeC (Fig.7.3).

Under different physical and chemical conditions volcanic CO_2 -rich fluids vented onto Kolumbo's crater seabed contain high concentrations of trace metals (i.e. Fe, Cu, Zn, As, Sb, Hg) (**Carey et al., 2013**; **Kilias et al., 2013a**). Ferrihydrite precipitates from the oxidation of Fe^{2+} to Fe^{3+} and rapid hydrolysis of Fe^{3+} (**Kilias et al., 2013**). The precipitation of these biogenic Fe^{3+} oxides provides a mechanism for the immobilization of Sb^{5+} (**Mitsunobu et al., 2013**) through coprecipitation or physical envelopment as well as providing a reactive surface with an adsorptive affinity for anions (i.e. PO_4^{3-}) and cations (i.e. Zn^{2+} , As^{5+} , Co^{2+} , U^{6+}).

Fourth precipitated episode: Antimony in the IPNC (Fig.7.4).

Under different physical and chemical conditions, Sb form distinct unidentified PXRD-amorphous Sb-Zn-S phases. According to their mode of precipitation they may be biogenic or inorganic. Filamentous Sb-Zn-S phases show typical features of fungi and, therefore, we consider that it represents completely mineralized fungal hyphae. According to **Dekov et al., (2013)**, Sb-Zn-S phases assume that an Sb-Zn containing hydrothermal fluid moving through the cracks of the seafloor basement has killed the fungal colonies living in the sub-seafloor. The fungal/microbial organic matter may have served as a geochemical trap for hydrothermal Sb which reacted with S possibly provided through S-bearing magmatic volatiles, or reduced from seawater sulphate, and mineralized fungal/microbial structures as Sb-Zn sulphosalts. The most important implication of this process of fungal and/or microbial Sb-Zn-S is that this is a mechanism of bio-sequestration of hydrothermal Sb in solid phases at seafloor hydrothermal sites, not reported before.

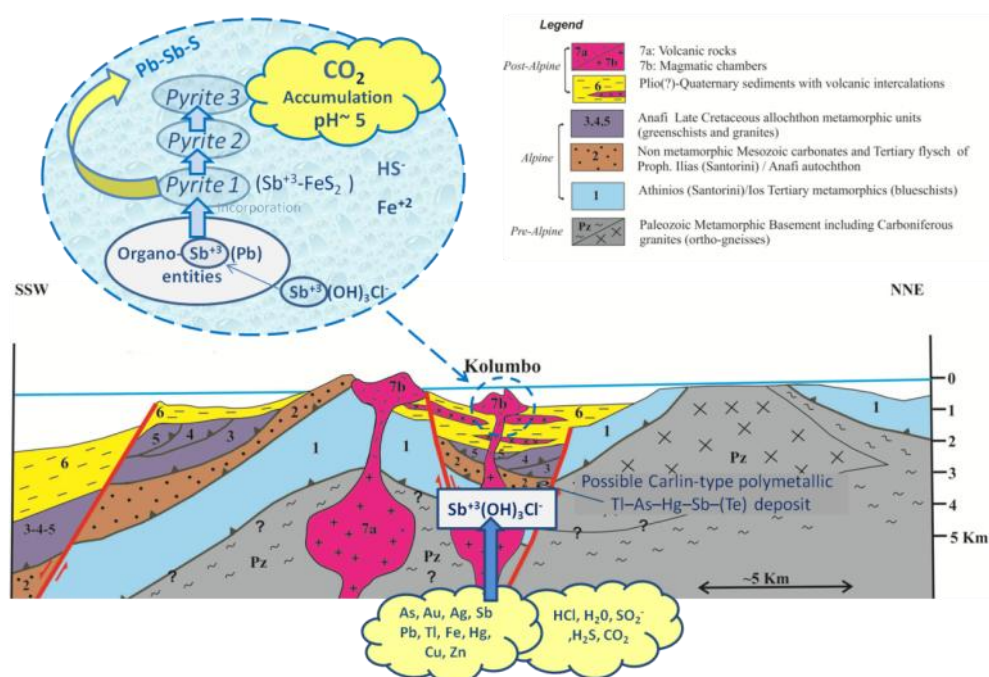


Fig.7.1 Deposition model: First precipitated episode: Antimony in ISSC of Politeia Chimneys. The faults (-in red) of Kolumbo hydrothermal system have been conduits of fluids driven by the high thermal regime (Nomikou et al., 2012). The extreme enrichment of hydrothermal fluids in Sb, as well as high enrichment in Fe, Zn, Cu, As, Pb, Sb, Au, Ag, Tl, Hg and Ba, may suggest leaching of an underlying possible polymetallic Carlin-type carbonate-hosted mineralization (2) (Muntean et al., 2011). Mixed hydroxy-chloride complexes $Sb(OH)_3Cl^-$ control Sb^{3+} transport in saline high-temperature ore fluids at acidic conditions ($pH \sim 5$) (Prokovski et al., 2006). **Stage 1:** Early hydrothermal precipitation. It is very likely that the Sb is hydrothermally emitted as the reduced Sb^{3+} form and initially extracted from the hydrothermal fluids by organic processes in the form of organo-Sb(Pb) entities. The latter may react abiotically with sulphide (HS^-) and/or Fe^{2+} to form Sb(Pb)-rich pyrite. At this stage, trace Sb (Pb±As) are “invisible” being locked in pyrite either as (i) nano-scale particles, or (ii) solid solutions within the pyrite structure. **Stage 2:** Hydrothermal diagenesis/maturation. This leads to recrystallization of most pyrite 1, and deposition of new

overgrown pyrite 2. Some of the Pb, Sb, As are released from pyrite 1 during recrystallization to form discrete mineral phases such as galena, sphalerite, and Pb-Sb sulphosalts. **Stage 3:** Hydrothermal fluid flow late during chimney formation leads to further recrystallization of previous pyrite 1 and 2 types, and: (i) growth of pyrite 3 which is commonly coarse grained, euhedral, and trace element poor and, (ii) Pb-Sb sulphosalt overgrowths. (Modified after Kilias et al., 2013).

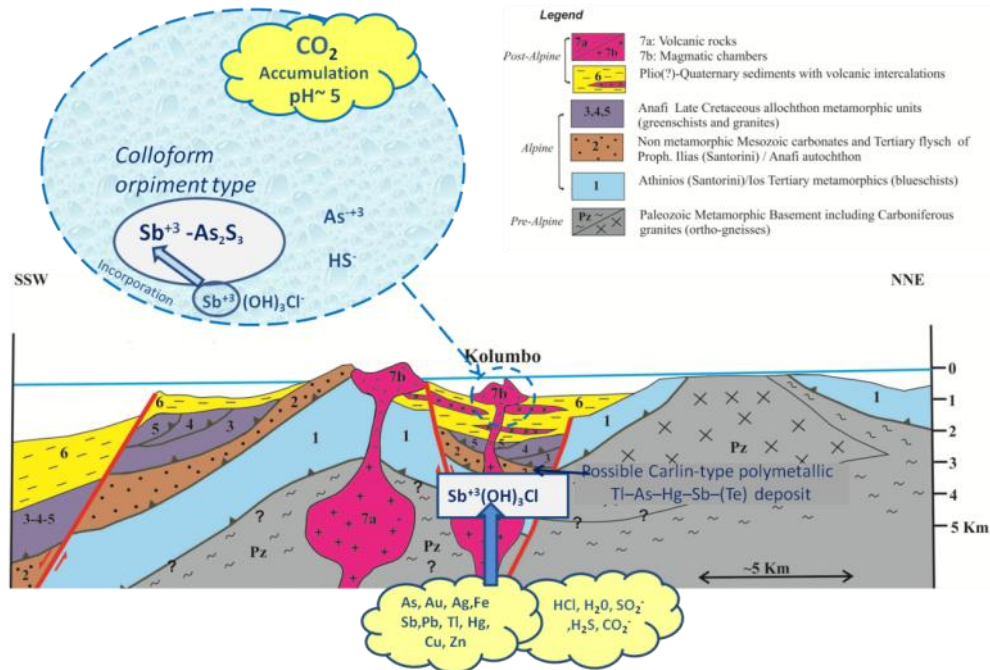


Fig.7.2 Deposition model. Second precipitated episode: Antimony in OASL of politia chimneys. Under different physical and chemical conditions colloform orpiment precipitates. Trace Sb is “invisible” being locked in colloform orpiment (As₂S₃)-type As-sulphide phases.

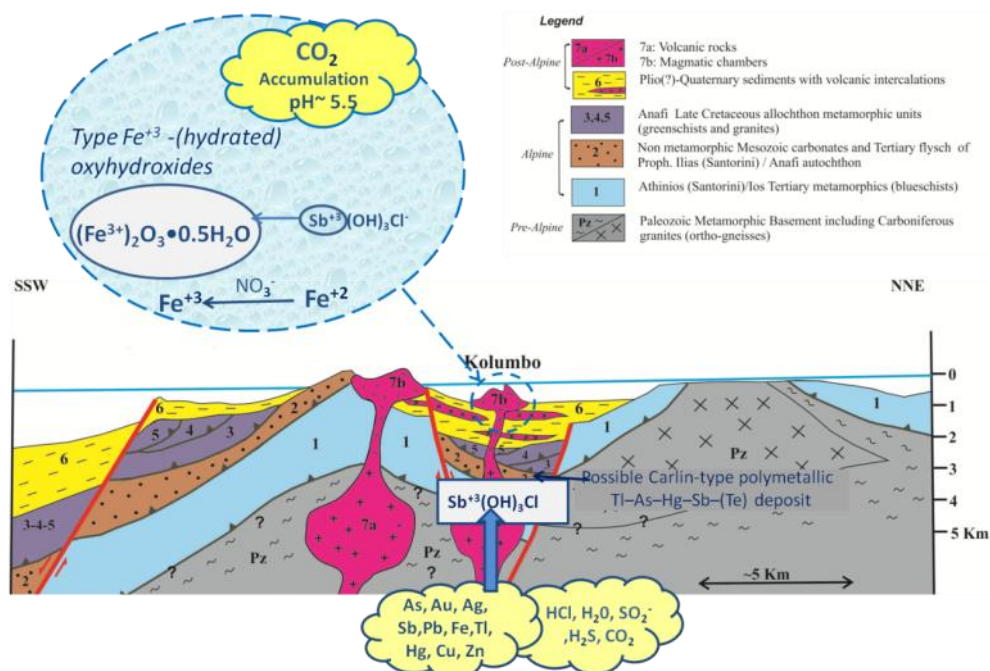


Fig.7.3 Deposition model. Third precipitated episode: Antimony in SFeC of politeia chimneys. Under different physical and chemical conditions volcanic CO₂-rich fluids vented onto Kolumbo's crater seabed contain high concentrations of trace metals (i.e. Fe, Cu, Zn, As, Sb, Hg) (Carey et al., 2013; Kiliias et al., 2013a). Ferrihydrite precipitates from the oxidation of Fe²⁺ to Fe³⁺ and rapid hydrolysis of Fe³⁺ (Kiliias et al., 2013). The precipitation of these biogenic Fe³⁺ (hydrated) oxyhydroxides provides a mechanism for the immobilization of Sb (Mitsunobu et al., 2013) through providing a reactive surface with an adsorptive affinity for Sb.

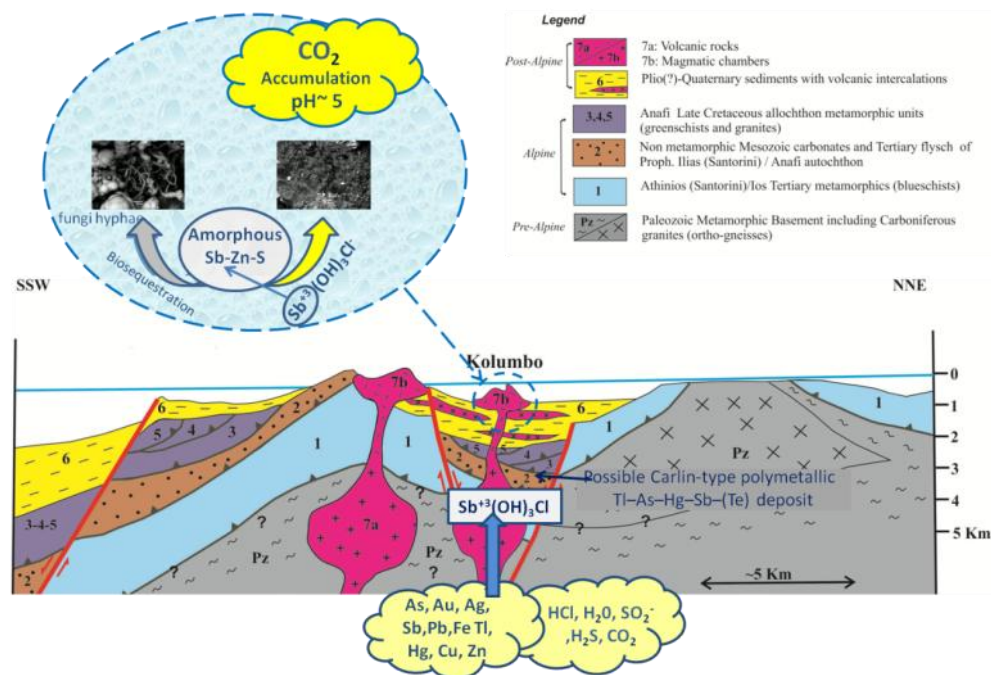


Fig.7.4 Deposition model: Fourth precipitated episode: Antimony in IPNC of politeia chimneys. Under different physical and chemical conditions, Sb form distinct unidentified PXRD-amorphous Sb-Zn-S phases. According to their mode of precipitation they may be biogenic or inorganic. The fungal/microbial organic matter may have served as a geochemical trap for hydrothermal Sb which reacted with S possibly provided through S-bearing magmatic volatiles, or reduced from seawater sulphate, and mineralized fungal/microbial structures as Sb-Zn sulphosalts. The most important implication of this process of fungal and/or microbial Sb-Zn-S is that this is a mechanism of bio-sequestration of hydrothermal Sb in solid phases at seafloor hydrothermal sites, not reported before.

7.6 Environmental considerations

Enrichments of polymetallic hydrothermal chimneys in Sb and Tl (Hg, As, Au, Ag, Zn, Fe), among the biggest ever reported from the world' oceans, have been discovered in the

hydrothermal vent field located on the floor of the density-stratified acidic (pH~ 5) crater of the Kolumbo shallow-submarine arc-volcano, near Santorini (**Kilias et al., 2013a**). These results indicate that volcanic CO₂-rich fluids venting onto Kolumbo's shallow (<2 km water depth) crater seabed cause local seawater acidification, and contain high concentrations of bioessential trace metals (i.e. Fe, Cu, Zn) and trace metal and metalloid emergent global pollutants such as Sb, as well as As, Tl, and Hg. The observed metal enrichment have significant implications for toxic metal (i.e. Tl, Sb, As, Hg) transport and biogeochemical cycling in seafloor hydrothermal systems, and underscores the importance of Kolumbo's submarine volcanic and geothermal activity as a potential source of toxic metals to: (1) microbial metabolism, (2) marine phytoplankton cell growth and marine food webs, and, (3) in areas exploited by fishing such that Kolumbo ~12 miles NE of Santorini. It is not known how common the type of polymetallic Sb-rich deposit studied here may be in the submarine volcanoes of the Kolumbo line, along the CSK tectonic line (**Nomikou et al., 2012**).

It is critical for such hazard assessment having measurements of these toxic trace metals on seabed, and of course sea column, solid materials. Therefore the results of our mineralogical and geochemical study on antimony fixation in solid phases at Kolumbo's submarine hydrothermal vents are essential, because these minerals and especially pyrite/marcasite are proved crucial for reducing the high hydrothermal flux of this notorious environmental toxin to seawater near a fishing area; moreover, these results are proved an important part of the yet unclear and environmental data poor geoenvironmental and biogeochemical Sb-cycle.

Given the significant role that the Christianna-Santorini-Kolumbo (CSK) tectonic line plays for the region's morphology, volcanism, hydrothermal activity, and seismicity, the hazardous release of potentially toxic metals into the water column may be tied to the earthquake cycle in that highly touristic Santorini island. This notion may be supported by the fine-scale Sb zoning observed in concentrically laminated pyrite/marcasite (see Fig. 6.6). The destiny of these potentially toxic metals once they enter the water column is unknown.

Previous studies have shown that poorly crystalline ferrihydrite is one of the important sorbents for Sb in natural oxic soils and sediments, and that the transformation of ferrihydrite significantly influences the mobility of the Sb (**see Mitsunobu et al., 2013, and references therein**). Moreover, Sb transfers into more thermodynamically stable solids from the metastable ferrihydrite with aging (**Mitsunobu et al., 2013**). It follows that, the Sb associated with ferrihydrite-like material on the surface of the Kolumbo chimneys (SFeC) (Fig. 6.13) may be rigidly immobilized with time. These findings are valuable for making

predictions on the long-term fate of Sb associated with ferrihydrite in such shallow seafloor hydrothermal systems environments.

Due to their biogeochemical characteristics, the Sb-impacted Kolumbo vents offer unprecedented opportunities to evaluate the magnitude and significance of microbial/fungal biogeochemical Sb cycle in nature through studies of Sb-reducing and Sb-oxidizing communities. The types of biota living on the surface of the Kolumbo chimneys are only beginning to be known (i.e. Archea, *Nitrosopumilus maritimus*) (Kilias et al., 2013a), and it is unclear if specialized microorganisms (i.e. bacteria) that gain their energy requirements from redox transformations of Sb exist. For instance it is not known that Sb³⁺-oxidizing autotrophic bacteria fix CO₂ using Sb³⁺ as an electron donor, thereby oxidizing it to Sb⁵⁺ or microorganisms are capable of anaerobic respiration using antimonite (Sb⁵⁺) as a terminal electron acceptor, may be active on and around the chimneys where reduced hydrothermal Sb³⁺ is mixed with oxygenated ocean water (Robert T Kulp, pers. communication). Some strains can also oxidize Sb³⁺ with nitrate to achieve growth in the absence of O₂, in a manner analogous to anoxic As³⁺ oxidation with NO₃ (Oremland et al., 2003). Moreover, how Sb, and the other contaminants, may affect, or may be affected by, hydrothermal vent microbial ecosystems, and those at higher trophic levels, is unknown. These may be especially relevant to Kolumbo's vent system given that biological NH₄ oxidation to NO₃ occurs around the Kolumbo vents (Kilias et al., 2013).

These data provide the first evidence of a natural microbiological population that utilizes Sb⁵⁺ as a terminal electron acceptor for anaerobic heterotrophic respiration. Our results with sediments from both Sb contaminated and Sb-free environments suggest that the capacity for microorganisms to reduce Sb⁵⁺ to Sb³⁺ may be environmentally widespread, but that in populations which are not adapted to high Sb concentrations this reduction may be accomplished by detoxification mechanisms or other enzymatic pathways not linked to respiration. In sulphidic settings, Sb⁵⁺ reduction can proceed biologically or abiologically, and results in the sedimentary sequestration of Sb as Sb₂S₃ and other metastable Sb-S minerals (e.g., Sb₂S₅). In cases where Sb contamination co-occurs with high As concentrations, dissimilatory As⁵⁺ reduction may be expected to be favored over Sb⁵⁺ reduction. Our results demonstrate the complexity of predicting Sb speciation and biogeochemical behavior in the presence of sulfide and As⁵⁺ two geochemical species that commonly co-occur with the element. These findings also evoke the prospect of a microbial biogeochemical Sb cycle in nature, the magnitude and significance of which should be evaluated through studies of Sb-reducing communities from other Sb-impacted areas (Kulp et al., 2013).

Microorganisms are capable of anaerobic respiration using antimonate as a TEA. This discovery completes the biogeochemical cycle of Sb through the oxidized and reduced forms and adds Sb to the growing list of metals and metalloids whose oxidized species are capable of serving as electron acceptors for microbial respiration – a list that already includes Fe, Mn, Cr, U, V, Co, Tc, Np, Pu, As, Se, and Te. Importantly, the insoluble product of antimonate reduction, Sb_2O_3 , is a versatile compound that may be of commercial significance to the emerging nanotechnology industry. Owing to the uncertainty in the speciation of Sb in the parent fluids, its bioavailability cannot be evaluated. Formation of methyl Sb would be favored by high concentrations of dissolved C, which is a likely scenario for Kolumbo given the high organic matter content of the chimneys (Kiliias et al., 2013a). It is also possible that extremophile biota (epifauna and bacteria) may thrive on and in the antimoniferous Fe-rich layers and those microorganisms may possess enzymes that allow them to survive in such toxic environments.

8. Summary and Conclusions

- ❖ Antimony, an emergent global contaminant, that is hydrothermally discharged along with other trace metal(-loid) pollutants (As, Tl, and Hg), and precious and bioessential trace metals (i.e. Au, Ag, Fe, Cu, Zn), onto Kolumbo volcano's shallow (<500 m water depth) crater seabed, is trapped either in pyrite and/or marcasite, rare orpiment-like As-sulfides, and ferrihydrite-like Fe-oxy(hydro)oxides, or forms independent unidentified $Pb(Zn)_nSb_mS_p$ sulphosalt phases, of diffusely venting polymetallic Sb-rich (up to 2.2 wt%) seafloor hydrothermal vent chimneys.
- ❖ Optical and Scanning Electron Microscopy-Backscattered Electron (SEM-BSE) observations and analyses, combined with Synchrotron Radiation (SR) based μ -XRF elemental mapping, and μ -XAFS spectra at LIII-edge for Sb, have revealed four(4) distinct modes (A-D) of Sb sequestration and enrichment, in ore-grade (up to 2 wt% Sb) samples of Sb-polymetallic mineralization from different mineralogical zones (i.e. ISSC, OAsL, SFeC, IPCN):
 - ❖ **A:** High concentrations (up to 11 wt%) are found in early concentrically laminated chemically-zoned hydrothermal pyrite (ISSC), along individual micron-scale zones. Antimony may occur in the relatively more toxic trivalent (or lower valence) (Sb^{3+}) rather than pentavalent (Sb^{5+}) forms, which is consistent with organic-rich (C_{org} : 5.3 %TOC) and sulphide-rich reducing hydrothermal conditions. Lead (Pb) always occurs with Sb in these zones where the abundances of Sb and Pb vary inversely with Fe and S, suggesting that Sb and Pb either occupy the Fe and S sites in the pyrite/marcasite, and/or at least part of the Sb occurs in sulphosalt nanoparticles of Sb and Pb. This finding indicates that pyrite and/or marcasite can control Sb (and other trace metals of economic and environmental importance) sequestration and concentration during polymetallic shallow-submarine hydrothermal vent mineralization. Antimony is additionally partitioned in individual antimoniferous crystalline phases that constitute unidentified non-stoichiometric $Pb_nSb_mS_p$ sulphosalts.
 - ❖ **B:** The highest concentrations of Sb (up to 16 wt %) are found in aggregates of colloform banded orpiment (As_2S_3)-type As-sulphide phases (OAsL), in growth zones which appear "bright" in BSE.
 - ❖ **C:** Antimony is linked with poorly ordered ferrihydrite-type (characterized by XAFS), Fe-(hydrated)-oxyhydroxides (SFeC) in the Fe microbial mats that cover the Kolumbo hydrothermal chimneys. This is, to our knowledge, the first time that a trace

metal(loid) like Sb is reported linked with short-ordered Fe³⁺-oxyhydroxides /ferrihydrite in shallow-marine hydrothermal systems associated with submarine arc-volcanos.

- ❖ **D:** Unidentified antimoniferous (Zn_mSb_nS_p) sulphosalt phases occur as dark violet metallic aggregates, as well as filaments, of the interior porous conduits (IPCN).
- ❖ Mineralization particularly where related to Sb is ubiquitous throughout the life of a particular chimney or hydrothermal edifice and the vent field. This combined with the presence of distinct chemical variations of Sb (and Pb) arranged in a fine-scale (µm) zonal distribution, within concentrically laminated pyrite and/or marcasite, and colloform banded orpiment-like phases, may suggest that this selective partitioning of Sb is most likely the result of changes in hydrothermal fluid composition, as well as pH and temperature. The latter are likely linked to the episodic nature of the Kolumbo hydrothermal vent system, i.e. periodic influx of magmatic hydrothermal fluids and associated cycles of Sb-(Pb) rich hydrothermal activity. Alternatively, **these variations may** suggest different chemical microenvironments within chimneys that may contribute to improved understanding of geomicrobiological processes at seafloor hydrothermal vents.
- ❖ We show that the concentrations of Sb and Pb, and likely of precious metals (e.g., Au, Ag), metalloids (e.g., As, Se, Te, Tl) and heavy metals (e.g., Cu, Zn, Hg) in pyrite from seafloor hydrothermal vent systems are more significant than previously thought.
- ❖ Based on our findings, the hydrothermal systems that host pyrite and/or other sulphides likely containing numerous trace contaminant (i.e. Sb, Pb), have been extended to include seafloor hydrothermal vent systems.
- ❖ The filamentous Sb-bearing sulphosalts (Zn_mSb_nS_p) of the IPCN exhibit fungal and/or microbial features and may be considered completely Sb-(Zn)mineralized microfossils, and accordingly biogenic. The fungal/microbial organic matter may have served served as a geochemical trap for hydrothermal Sb which reacted with S possibly provided through S-bearing magmatic volatiles, or reduced from seawater sulfate, and mineralized fungal/microbial structures as Sb-Zn sulphosalts. The most important implication of this process of fungal and/or microbial Sb-Zn-S is that this is a mechanism of bio-sequestration of hydrothermal Sb in solid phases at seafloor hydrothermal sites, not reported before.

- ❖ The solid phases that were found to fix Sb on the seafloor are proved crucial for reducing the high hydrothermal flux of this notorious environmental toxin to seawater, near the fishing area of Santorini that is also one of the most popular tourist places in the world. Moreover, these results offer novel insights to the geoenvironmental and biogeochemical Sb-cycle in nature, and specifically the marine environment.
- ❖ Sb is tightly linked with the biogenic ferrihydrite-type Fe^{3+} -(hydrated)-oxyhydroxides on the surface of the Kolumbo chimneys (SFeC) suggesting that Sb may be rigidly immobilized with time. These findings are valuable for making predictions on the long-term fate of Sb associated with ferrihydrite in such shallow seafloor hydrothermal systems environments. Due to their biogeochemical characteristics, the Sb-impacted Kolumbo vents offer unprecedented opportunities to evaluate the magnitude and significance of microbial/fungal biogeochemical Sb cycle in nature through studies of Sb-reducing and Sb-oxidizing communities.
- ❖ The observed enrichment of Sb^{3+} (toxic trivalent species) emphasize the weight of shallow-submarine geothermal activity as a potential source of toxic metals (Sb^{3+}) during seafloor weathering, and/or natural disasters (i.e. explosive volcanic/hydrothermal, and seismic activity).
- ❖ Due to their biogeochemical characteristics, the Sb-impacted Kolumbo vents offer unprecedented opportunities to evaluate the magnitude and significance of microbial/fungal biogeochemical Sb cycle in nature, and its effect on seafloor microbial ecosystems through studies of Sb-reducing and Sb-oxidizing communities. It is also possible that extremophile biota (epifauna and bacteria) may thrive on and in the antimoniferous Fe-rich layers, and those microorganisms may possess enzymes that allow them to survive in such toxic environments.

References

- Abin, C.A., Hollibaugh J. T., 2014. Dissimilatory Antimonate Reduction and Production of Antimony Trioxide Microcrystals by a Novel Microorganism. *Environmental science and Technology* 48, 681–688.
- Abraitis, P.K., Patrick, R.A.D., Vaughan, D.J., 2004. Variations in the compositionl textural and electrical properties of natural pyrite: a review. *Int. J. Miner. Process.* 74, 41-59.
- Adams, F., Vincze, L., Vekemans, B., 2011. Synchrotron Radiation for Microscopic X-ray Fluorescence Analysis. *Handbook of Nuclear Chemistry*, 1737-1759.
- Alexandri, M., Papanikolaou, D., Nomikou, P., 2003. Santorini Volcanic Field-New Insights Based on Swath Bathymetry. Abstracts IUGG, 30 June-11 July 2003, Sapporo, Japan.
- Allwood, A.C., Walter, M.R., Kamber, B.S., Marshall, C.P., Burch, I.W., 2006. Stromatolite reef from the Early Archaean era of Australia. *Nature* 441 (7094), 714–718.
- Amarasiriwardena, D., Wu.,F., 2011. Antimony: Emerging toxic contaminant in the environment. *Microchemical Journal* 97 , 1–3.
- Anangi, A., Hofmann, A., Wohlgemuth-Ueberwasser, C.C., 2012. Pyrite zoning as a record of mineralization in the Ventersdorp Contact Reef, Witwatersrand Basin, South Africa. *Economic geology* 108, 1243-1272.
- Andreae, M.O., Froelich, P.N., 1984. Arsenic, antimony, and germanium biogeochemistry in the Baltic Sea. *Tellus* 36B, 101–117.
- Bau, M., 1991. Rare-earth element mobility during hydrothermal and metamorphic fluid-rock interaction and the significance of the oxidation state of europium. *Chem. Geol.* 93, 219–230.
- Bau, M., Dulski, P., 1996. Distribution of yttrium and rare-earth elements in the Penge and Kuruman Iron-Formations, Transvaal Supergroup, South Africa. *Precambrian Res.* 79, 37–55.
- Bell, K.L.C., Nomikou, P., Carey, S.N., Stathopoulou, E., Polymenakou, P., Godelitsas, A., Roman, c., Parsks, M., 2012. Continued exploration of the Santorini volcanic field and cretan basin, Aegean Sea. *Oceanography* 25, 1.
- Belzile, N., Chen, Y-W., Filella, M., 2011. Human Exposure to Antimony: I. Sources and Intake. *Critical Reviews in Environmental Science and Technology*, 41, 1309–1373.
- Bencze, K., 1994. Antimony. In: Seiler, H.G., Sigel, A., Sigel, H. (Eds.), *Handbook on Metals in Clinical and Analytical Chemistry*. Marcel Dekker, New York 227–236.
- Berkenbosch, H.A., de Ronde, C.E.J., Gemmell, J.B., McNeill., A.W., Goemann, K., 2012. Mineralogy and formation of black smoker chimneys from Brothers submarine volcano, Kermadec arc. *Economic geology* 107, 1613-1633.
- Beyersmann, D., Hartwig, A., 2008. Carcinogenic metal compounds: recent insight into molecular and cellular mechanisms. *Arch Toxicol.* 82(8), 493-512.
- Bijun, L., Wu, F., Li, X., Fu, Z., Deng, Q., Mo, C., Zhu, J., Zhu, Y., Liao, H., 2011. Arsenic, antimony and bismuth in human hair from potentially exposed individuals in the vicinity of antimony mines in Southwest China *Microchemical Journal* 97, 20–24.
- Borch, T., Kretzschmar, R., Kappler, A., Cappelen, P.V., Ginder-Vogel, M., Voegelin, A., Campbell, K., 2009. Biogeochemical Redox Processes and their Impact on Contaminant Dynamics. *Environ. Sci. Technol.* 2010, 44, 15-23.
- Boyle, R.W., Jonasson, I.R., 1983. The geochemistry of antimony and its use as an indicator element in geochemical prospecting. *Journal of Geochemical Exploration*, 20, 223-302.
- Buchholz, P., Oberthur, T., Luders, V., Wilkinson, J., 2007. Multistage Au-As-Sb Mineralization and Crustal-Scale Fluid Evolution in the Kwekwe District, midlands Greenstone belt, Zimbabwe: A Combined Geochemical, Mineralogical, Stable Isotope, and Fluid Inclusion Study. *economic Geology*, 102, 347-378.

- Butler, I.B., Nesbitt, R.W., 1999. Trace element distributions in the chalcopyrite wall of a black smoker chimney: insights from laser ablation inductively coupled plasma mass spectrometry (LA-ICP-MS). *Earth and Planetary Science Letters* 167, 335–345).
- Byrne, R.H., 2002. Inorganic speciation of dissolved elements in seawater: the influence of pH on concentration ratios. *Chemochem. Trans* 3 (11).
- Canet, C., Prol-Ledesma, R.M., Antonio Proenza, J.A., Rubio-Ramos, M.A., Forrest, M.J., Torres-Vera, M.A., Rodriguez-Diaz, A.A., 2005. Mn–Ba–Hg mineralization at shallow submarine hydrothermal vents in Bahia Concepcion, Baja California Sur, Mexico. *Chemical Geology* 224, 96–112.
- Cantner, K., Carey, S., Nomikou, P., 2013. Integrated volcanologic and petrologic analysis of the 1650AD eruption of Kolumbo submarine volcano, Greece. *Journal of Volcanology and Geothermal Research* 269, 28–43.
- Carey, S., Nomikou, P., Croff-Bell, K., Lilley, M., Lupton, J., Roman, C., Stathopoulou, E., Bejelou, K., Ballard, R., 2013. CO₂ degassing from hydrothermal vents at Kolumbo submarine volcano, Greece and the accumulation of acidic crater water. *Journal of Geochemical Exploration* 20, 223–302.
- Cavalazzi, B., Barbieri, R., & Ori, G. G., 2007. Chemosynthetic microbialites in the Devonian carbonate mounds of Hamar Laghdad (Anti-Atlas, Morocco). *Sedimentary Geology*, 200(1), 73–88.
- Chi Fru, E., Ivarsson, M., Kiliyas, S.P., Bengtson, S., Belivanova, V., Marone, F., Fortin, D., Broman, C., Stampanoni, M., 2013. Fossilized iron bacteria reveal a pathway to the biological origin of banded iron formation. *Nat. Commun.* 4:2050.
- Cook, N.J., Ciobanu, C.L. and Mao, J.W., 2009. Textural control on gold distribution in As-free pyrite from the Dongping, Huangtuliang and Hougou gold deposits, North China Craton, (Hebei Province, China). *Chemical Geology* 264, 101–121.
- Corliss, J.B., Dymond, J., Gordon, L.I., Edmond, J.M., Von Herzen, R.P., Ballard, R.D., Green, K., Williams, D., Bainbridge, A., Crane, K., Van Andel, T.H., 1979. Submarine thermal springs on the Galapagos Rift. *Science*.
- Cornell, R., Schwertmann, U., 2003. *The Iron Oxides: Structures, Properties, Reactions, Occurrences and Uses*, 2nd ed. Wiley-VCH, Weinheim.
- Craddock P.R., Bach, W., Seewald, J.S., Rouxel, O.J., Reeves, E., Tivey, M.K., 2010. Rare earth element abundances in hydrothermal fluids from the Manus Basin, Papua New Guinea: Indicators of sub-seafloor hydrothermal processes in back-arc basins. *Geochimica et Cosmochimica Acta* 74, 5494–5513.
- Critical Raw Materials for the EU. Report of the Ad-hoc Working Group on Defining Critical Raw Materials, 2010. Downloaded from http://ec.europa.eu/enterprise/policies/rawmaterials/documents/index_en.htm (October 2011).
- Cutter, G.A., 1991. Dissolved arsenic and antimony in the Black Sea. *Deep-Sea Res.* 38, S825–S843.
- Cutter, G.A., Cutter, L.S., Featherstone, A.M., Lohrenz, S.E., 2001. Antimony and arsenic biogeochemistry in the western Atlantic Ocean. *Deep-Sea Res.*, II 48, 2895 – 2915.
- d'Amore, J. J., Al-Abed, S. R., Scheckel, K. G., Ryan, J. A., 2005. Methods for Speciation of Metals in Soils: A Review. *J. Environ. Qual.* 34:1707–1745.
- de Roche, T.E., Colomer, J.M., Conesa, N., Torres, B., Castillo-Oliver, M., Jawhari, T., Bailo, E. and Melgarejo, J.C., 2012. Thallian arsenian pyrite from submarine vents in Dominica, Lesser. *European Mineralogical Conference*. Vol. 1, EMC2012-707-100.
- de Ronde, C. E. J., Massoth, G. J., Butterfield, D. A., Christenson, B. W., Ishibashi, J., Ditchburn, R. G., Hannington, M. D., Brathwaite, R. L., Lupton, J. E., Kamenetsky, V. S., Graham, I. J., Zellmer, G. F., Dziak, R. P., Embley, R. W., Dekov, V. M., Munnik, F., Lahr, J., Evans, L. J., and Takai, K., 2011. Submarine hydrothermal activity and gold-rich

- mineralization at Brothers Volcano, Kermadec Arc, New Zealand. *Mineralium Deposita* 46, 541-584.
- de Ronde, C.E.J., Hannington, M.D., Stoffers, P., Wright, I.C., Ditchburn, R.G., Reyes, A.G., Baker, E.T., Massoth, G.J., Lupton, J.E., Walker, S.L., Greene, R.R., Soong, C.W.R., Ishibashi, J., Lebon, G.T., 2005. Evolution of a submarine Magmatic-Hydrothermal system: Brothers volcano, southern Kermadec arc, New Zealand. *Economic geology*, 100, 109-1133.
- Deditius, A.P., Utsunomiya, S., Ewing, R. C., Chryssoulis, S.L., Venter, D., Kesler, S.E., 2009. Decoupled geochemical behavior of As and Cu in hydrothermal systems. *Geology*; 37(8),707-710; doi: 10.1130/G25781A.1; 4 figures; Data Repository item 2009170.
- Deditius, Artur P., Utsunomiya, S., Reich, M., Kesler, S.E., Ewing, R.C., Hough, R., Walshe, J., 2011. Trace metal nanoparticles in pyrite. *Ore Geology Reviews* 42, 32–46.
- Dekov, M., Bindi, L., Burgaud, G., Petersen, S., Asael, D., Rédou, V., Fouquet, Y., Pracejus, B., 2013. Inorganic and biogenic As-sulfide precipitation at seafloor hydrothermal fields Vesselin Marine Geology 342, 28–38.
- Dominey-Howes, D.T.M., Papadopoulos, G.A., Dawson, A.G., 2000. Geological and geochemical evolution of the Kermadec Arc, New Zealand. *Journal of Metamorphic Geology* 18, 109–124.
- É., Charlou, J. L., Donval, J. P., Hureau, D., & Appriou, P., 1999. As and Sb behaviour in fluids from various deep-sea hydrothermal systems. *Comptes Rendus de l'Académie des Sciences Series IIA Earth and Planetary Science*, 328(2), 97-104.
- Duester, L., Van der Geest, H.G., Moelleken, S., Hirner, A.V., Kueppers, K., 2011. Comparative phytotoxicity of methylated and inorganic arsenic –and antimony species to *Lemna minor*, *Wolffia arrhiza* and *Selenastrum capricornutum*. *Microchemical journal* 97(1):30-37.
- Eckhardt, J.-D., Glasby, G. P., Puchelt, H., Berner, Z., 2008. Hydrothermal manganese crusts from Enarete and Palinuro seamounts in the Tyrrhenian Sea. *Marine Georesources and Geotechnology*, 15:175-208, 1997.
- Fan, D., Zhang, T., Ye, J., 2004. The Xikuangshan Sb deposit hosted by the Upper Devonian black shale series, Hunan, China. *Ore Geology Reviews* 24, 121-133.
- Feng, R., Wei, C., Tu, S., Tang, S., Wu, F., 2011. Detoxification of antimony by selenium and their interaction in paddy rice under hydroponic conditions. *Microchemical Journal* 97, 57–61.
- Feng, S., Cokus, S.J., Zhang, X., Chen, P.-Y., Bostick, M., Goll, M.G., Hetzel, J., Jain, J., Strauss, S.H., Halpern, M.E., Ukomadu, C., Sadler, K.C., Pradhan, S., Pellegrini, M., Jacobsen, S., 2010. Conservation and divergence of methylation patterning in plants and animals. *Proc Natl Acad Sci U S A*. 107(19): 8689–8694.
- Fengchang F.W., Bijun, M.C., Zhu, L.J., Deng, Q., Liao, H., Zhang, Y., 2011. Bioaccumulation of antimony, arsenic, and mercury in the vicinities of a large antimony mine, China Zhiyou. *Microchemical Journal* 97, 12–19.
- Filella, M., 2011. Antimony interactions with heterogeneous complexants in waters, sediments and soils: A review of data obtained in bulk samples. *Earth-Science Reviews* 107, 325–341.
- Filella, M., Belzile, N., Chen Yu-Wei., 2002a. Antimony in the environment: a review focused on natural waters. I Occurrence. *Earth-Science Reviews* 57, 125-176.
- Filella, M., Belzile, N., Chen Yu-Wei., 2002b. Antimony in the environment: a review focused on natural waters. II Relevant solution chemistry. *Earth-Science Reviews* 59, 265-285.
- Filella, M., Belzile, N., Lett, M. C., 2007. Antimony in the environment: a review focused on natural waters. III Microbiota relevant interactions. *Earth-Science Reviews* 80, 195-217.
- Filella, M., Philippo, S., Belzile, N., Chen, Y., Quentel, F., 2009. Natural attenuation processes applying of antimony: A study in the abandoned antimony mine in Goesdorf, Luxemburg. *Science of the Total Environment* 407, 6205-6216.

- Filella, M., Williams, M.P., 2012. Antimony interactions with heterogeneous complexants in waters, sediments and soils: A review of binding data for homologous compounds. *Chemie der Erde* 72, S4, 49–65
- Filella, M., Williams, P.A., Belzile, N., 2009. Antimony in the environment: Knowns and unknowns. *Environ. Chem.* 6, 95-105.
- Finneran, K. T., Housewright, M. E., Lovley, D. R., 2002 Multiple influences of nitrate on uranium solubility during bioremediation of uranium-contaminated subsurface sediments. *Environ. Microbiol.* 4, 510-516.
- Florence, T.M., Morrison, G.M., Stauber, J.L., 1992. Determination of trace element speciation and the role of speciation in aquatic toxicity. *The science of the Total Environment* 125, 1-13.
- Florence, T.M., Morrison, G.M., Stauber, J.L., 1992. Determination of trace element speciation and role of speciation in aquatic toxicity. *The Science of the Total Environment*, 125, 1-13.
- Forster, M.A., Lister, G.S., 1999. Detachment faults in the Aegean core complex of Ios, Cyclades, Greece. In: *Exhumation Processes: Normal Faulting, Ductile Flow and Erosion.* (eds Ring, U., Brandon, M.T., Lister, G.S. & Willett, S.D.). *Spec. Publ. Geol. Soc. London* 154, 305-324.
- Fouquet, Y. et al., 1993 Metallogenesis in back-arc environments: the Lau Basin example. *Econ. Geol.* 88, 2154–2181.
- Fouquet, Y., Cambon, P., Etoubleau, J., Charlou, J.L., Ondréas, H., Barriga, F.J.A.S., Cherkashov, G., Semkova, T., Poroshina, I., Bohn, M., Donval, J.P., Henry, K., Murphy, P., Rouxel, O., 2010. Geodiversity of hydrothermal processes along the Mid-Atlantic Ridge and ultramafic-hosted mineralization: a new type of oceanic Cu–Zn–Co–Au volcanogenic massive sulfide deposit. In: Rona, P.A., Devey, C.W., Dymont, J., Murton, B.J. (Eds.), *Diversity of Hydrothermal Systems on Slow Spreading Ocean Ridges.* *Geophysical Monograph*, 188, 321–367.
- Fu, Z., Wu, F., Mo, C., Liu, B., Zhu, J., Deng, Q., Liao, H., Zhang, Y., 2011. Bioaccumulation of antimony, arsenic, and mercury in the vicinities of a large antimony mine, China. *Microchemical Journal*, 12-19.
- Fu, Z.Y., Wu, F.C., Amarasiwardena, D., Mo, C.L., Liu, B.J., Zhu, J., Deng, Q.J., Liao, H.Q., 2010. Antimony, arsenic and mercury in the aquatic environment and fish in a large antimony mining area in Hunan, China. *Sci. Total Environ.* 408, 3403-3410.
- Fytikas, M., Innocenti, F., Manetti, G., Mazzuoli, R., Peccerilo, A., Villari, L., 1984. Tertiary to Quaternary evolution of the volcanism in the Aegean Region. In: Dixon, J.E., Robertson, A.H.F. (Eds.), *The Geological Evolution of the Eastern Mediterranean* : *Geol Soc London* 17, 687-699.
- Fytikas, M., Kolios, M., Vougiouklakis, G., 1990. Post-Minoan volcanic activity of the Santorini volcano: Volcanic hazard and risk, forecasting possibilities, in Thera and the Aegean World III, 2, *Earth Sciences*, edited by Hardy, D.A, 183-198, Thera Found., Essex, UK.
- Galvez, T., Parmentier, M-L., Joly, C., Malitschek, B., Kaupmann, K., Kuhn, R., Bittiger, H., Froestl, W., Bettler, B., Pin, J-P., 1999. Mutagenesis and modeling of the GABA-B.
- Gamaletsos, P., Godelitsas, A., Dotsika, E., Tzamos, E., Göttlicher, J., & Filippidis, A., 2013. Geological sources of As in the environment of Greece: a review. In: A. Scozzari and E. Dotsika (eds.), *Threats to the Quality of Groundwater Resources: Prevention and Control* , *Hdb Env Chem*, DOI 10.1007/698_2013_230, Springer-Verlag Berlin Heidelberg 2013.
- Gebel, T., 1997. Arsenic and antimony: comparative approach on mechanistic toxicology. *Chemico-Biological Interactions* 107, 131–144.
- Grichuk, D. V., 2012. Thermodynamic model of ore-forming processes in a submarine island-arc hydrothermal system. *Geochemistry International*, 50(13), 1069-1100
- Gunn, G. (Ed.), 2013. *Critical metals handbook.* Wiley-Blackwell

- Gurnani, N., Sharma, A., Talukder, G., 1994. Effects of antimony on cellular systems in animals. *Nucleus* 37, 71–96.
- Halbach, P., Pracejus, B., Marten, A., 1993. Geology and mineralogy of massive sulfide ores from the central Okinawa trough, Japan. *Economic geology*, 88, 2210-2225.
- Hannington, M. D., de Ronde, C. D. J. and Petersen, S., 2005. Sea-floor tectonics and submarine hydrothermal systems In: *Economic Geology 100th Anniversary Volume*, ed. by Hedenquist, J. W., Thompson, J. F. H., Goldfarb, R. J. and Richards, J. P. Society of Economic Geologists, Littleton, Colorado, USA, pp. 111-141.
- Hannington, M.D., Peter, J.M., Scott, S.D., 1986. Gold in Sea-Floor Polymetallic Sulphide Deposit. *Economic Geology*, 81, 1867-1883.
- Hannington, M., Jamieson, J., Monecke, T., Petersen, S., Beaulieu, S., 2011. The abundance of seafloor massive sulfide deposits. *Geology*. 39, 1155–1158.
- Hein, J.R., 2005. Mercury- and Silver-Rich Ferromanganese Oxides, Southern California Borderland: Deposit model and environmental implications. *Society of economic geologists, Inc. economic geology*, 100, 1151-1168.
- Herzig, P.M., Hannington, M.D., 1995. Polymetallic massive sulfides at the modern seafloor. A review. *Ore geology reviews*, 10, 95-115.
- Hiller, E., Lalinska, B., Chovan, m., Jurkovic, L., Klimko, T., Jankular, M., Hovorik, R., Sottnik, P., Flakova, R., Zenisova, Z., 2012. Arsenic and antimony contamination of waters, stream sediments and soils in the vicinity of abandoned antimony mines in the Western Carpathians, Slovakia. *Applied Geochemistry* 27, 598-614.
- historical investigation of the 1650 Mt. Columbo (Thera Island) eruption and tsunami, Aegean Sea, Greece. *Natural Hazards* 21 (1), 83– 96.
- Hodkinson, R.A., Cronan, D.S., Varnavas, S.P., Perissoratis, C., 1994. Regional geochemistry of sediments from the Hellenic Volcanic Arc in regard to submarine hydrothermal activity. *Mar. Georesour. Geotechnol.* 12, 83-129.
- Huebscher, C., Hensch, M., Dahm, T., Dehghani, A., Dimitriadis, I., Hort, m., Taymaz, t., 2006. Toward a Risk Assessment of central Aegean Volcanoes. *EOS* 87 (39).
- Huerta-Diaz, M.A., Delgadillo-Hinojosa, F., Siqueiros-Valencia, A., Valdivieso-Ojeda, J., Reimer, J.J., Segovia-Zavala J. A., 2012. Millimeter-scale resolution of trace metal distributions in microbial mats from a hypersaline environment in Baja California, Mexico. *Geobiology*, 10, 531–547.
- Ivarsson, M., Bengtson, S., Skogby, H., Belivanova, V. & Marone, F., 2013. Fungal colonies in open fractures of subseafloor basalt. *Geo-Mar. Lett.* 33, 233–243.
- Juraj Majzlan and Montserrat Filella., 2012. *Chemie der Erde* 72 S4, 1.
- Kantin, R., 1983. Chemical speciation of antimony in marine algae. *Limnol. Oceanogr.* 28, 165–168.
- Kearey, P., Klepeis, K.A., Vine, F., 2009. *Global Tectonics* (3rd ed), 482 (Wiley-Blackwell, John Wiley & Sons, West Sussex UK).
- Kelley, D. S., 2005. From the Mantle to Microbes: The Lost City Hydrothermal Field. *Oceanography* 18, 32-45.
- Kelley, D.S., Fruh-Green, G.L., Karson, J.A., Ludwig, K.A., 2007. The Lost city hydrothermal field revisited. *Oceanography*, 20, 4.
- Kilias, S. P., Nomikou, P., Papanikolaou, D., Polymenakou, P. N., Godelitsas, A., Argyraki, A., Scoullou, M., 2014. Unique nexus between geodynamic and biogeochemical processes at shallow hydrothermal vents, Kolumbo submarine arc-volcano (Santorini). 1st International Geo-Cultural Symposium, 6-8 June, Thira, Santorini, Abstracts volume, p. 24.
- Kilias, S.P., Nomikou, P., Papanikolaou, D., Polymenakou, P.N., Godelitsas, A., Argyraki, A., Carey, S., Gamaletsos, P., Mertzimekis, T.J., Stathopoulou E., Goettlicher, J., Steininger, R., Betzelou, K., Livanos, I., Christakis, C., Bell, K.C., Scoullou, M., 2013. New insights into

- hydrothermal vent processes in the unique shallow-submarine arc-volcano, Kolumbo (Santorini), Greece. *Scientific Reports*. *Scientific Reports* 3, Article number: 2421.
- Klinhammer, G. P., Elderfield, H., Edmond, J.M., Mitra, A., 1994. Geochemical implications of rare earth element patterns in hydrothermal fluids from mid-ocean ridges. *Geochimica et Cosmochimica Acta*, 58, (23), 5 105-5113.
- Koski, R.A., Jonasson, I.R., Kadko, D.C, Smith,V.K., Wong,F.L.,1994. Compositions, growth mechanisms, and temporal relations of hydrothermal sulfide-sulfate-silica chimneys at the northern Cleft segment, Juan de Fuca Ridge.*Journal of geophysical research* 99: 4, 813-4, 832.
- Koski, R.A., Jonasson, I.R., Kadko, D.C., Smith, V.K., Wong, F.L.,1994. Compositions, growth mechanisms, and temporal relations of hydrothermal sulfide-sulfate silca chimneys at the northern Cleft segment, Juan de Fuca Ridge. *Journal of geophysical research* 99, B3, 4813-4832.
- Krachler, M., Zheng,J., Koerner,R., Zdanowicz,C., Fisher, D., Shotyk,W.,2005. Increasing atmospheric antimony contamination in the northern hemisphere: snow, ice and evidence from Devon Island, Arctic Canada. *J. Environ. Monit* 7, 1169. doi:10.1039/B509373B
- Kříbek, B., Sýkorová, I., Pašava, J., Machovič, V., 2007. Organic geochemistry and petrology of barren and Mo–Ni–PGE mineralized marine black shales of the Lower Cambrian Niutitang Formation (South China). *International Journal of Coal Geology*, 72(3), 240-256).
- Kristall, B., Kelley, D.S., Hannington, M.D., Delaney, J.R., 2006. The growth history of a diffusely venting sulfide structure from the Juan de Fuca Ridge: a petrological and geochemical study. *Geochemistry Geophysics Geosystems* 7. doi: 10.1029/2005GC001166.
- Kristall,B., Nielsen, D., Hannington, M.D., Kelley, D.S., Delaney, J.R., 2011. Chemical microenvironments within sulfide structures from the Mothra hydrothermal field: Evidence from high resolution zoning of trace elements. *Chemical Geology* 290, 12-30.
- Kucha,H., Schroll, E., Raith , J. G., Halas, S., 2010. Microbial Sphalerite Formation in Carbonate-Hosted Zn-Pb Ores, Bleiberg, Austria: Micro- to Nanotextural and Sulfur Isotope Evidence. *Economic Geology*, v. 105, pp. 1005–1023.
- Kulp, T. R., Miller, L. G., Braiotta, F., Webb, S. M., Kocar, B. D., Blum, J. S., & Oremland, R. S.,2014. Microbiological reduction of Sb (V) in anoxic freshwater sediments. *Environ. Sci. Technol.*, 48 (1),218–226.
- Lack, J. G., Chaudhuri, K.C., Coated,J.D.,2002 Immobilization of radionuclides and heavy metals through anaerobic 19 bio-oxidation of Fe(II). *Appl. Environ. Microbiol.* 68, 2704-2710.
- Large, R.R., Danyushevsky, I., Hollit, C., Maslennikov, V., Meffre, S., Gilbert, S., Bull, S., Scott, R., Emsbo,P., Thomas, H., Singh, B., Foster, J., 2009. Gold and trace element zonation in pyrite using a lazer imaging technique: Implications for the timing of gold in orogenic and carlin-style sediment-hosted deposits. *Economic Geology*, 104, 635-668.
- Laurila T.E., Hannington ,M.D., Petersen, S ., Garbe-Schonberg, D., 2014. Early depositional history of metalliferous sediments in the Atlantis II Deep of the Red Sea: Evidence from rare earth element geochemistry. *Geochimica et Cosmochimica Acta* 126 , 146–168.
- Lazăr, I., Grădinaru , M., Petrescu, L., 2013. Ferruginous microstromatolites related to Middle Jurassic condensed sequences and hardgrounds (Bucegi Mountains, Southern Carpathians, Romania). *Facies*, 59(2),359-390.
- Leuz, A.K., Johnson, C.A.R., 2005. Oxidation of Sb(III) to Sb(V) by O₂ and H₂O₂ in aqueous solutions. *Geochim. Cosmochim. Acta* 69 , 1165–1172.

- Liu, B., Wu, F., Li, X., Fu, Z., Deng, Q., Mo, C., Zhu, J., Zhu, Y., Liao, H., 2010. Arsenic, antimony and bismuth in human hair from potentially exposed individuals in the vicinity of antimony mines in Southwest China.
- Lowell, R. P., P. A. Rona, R. P. Von Herzen, Seafloor hydrothermal systems, *J. Geophys. Res* 100, 327–352, 1995.
- Maher, M ; 2010. Critical Raw Materials for the EU. Report of the Ad-hoc Working Group on defining critical raw materials.
- Maher, W. A ., 2009. Antimony in the environment – the new global puzzle. *Environ. Chem* 6, 93–94.
- Melekestseva, I. Y., Tret'yakov, G. A., Nimis, P., Yuminov, A. M., Maslennikov, V. V., Maslennikova, S. P., Vasily A. Kotlyarov, Victor E. Beltenev, Leonid V. Danyushevsky, Large, R., 2014. Barite-rich massive sulfides from the Semenov-1 hydrothermal field (Mid-Atlantic Ridge, 13° 30.87' N): Evidence for phase separation and magmatic input. *Marine Geology* 349, 37–54.
- Metaxas, A. & Commission Internationale pour l'Exploration de la Mer Mediterranee -CIESM, Monaco. In., 2003. Current challenges in the study of biological communities at deep sea hydrothermal vents.
- Michard. A., 1989. Rare earth element systematics in hydrothermal fluids. *Geochemica et Cosmochimica Acta* 53, 745-750.
- Mitra, A., Elderfield, H., Greaves, M.J., 1994. Rare earth elements in submarine hydrothermal fluids and plumes from the Mid-Atlantic Ridge. *Marine Chemistry* 46, 217-235.
- Mitsunobu, S., Muramatsu, C., Watanabe, K., Sakata, M., 2013. Behavior of Antimony (V) during the Transformation of Ferrihydrite and Its Environmental Implications. *Environ. Sci. Technol*, 47, 9660-9667.
- Mitsunobu, S., Takahashi, Y., Terada, Y., Sakata, M., 2010. Antimony (V) Incorporation into Synthetic Ferrihydrite, Goethite, and Natural Iron Oxyhydroxides. *Environ. Sci. Technol*, 44, 3712–3718.
- Mottl, Michael J., Jeffrey S. Seewald, C. Geoffrey Wheat, Margaret K. Tivey, Peter J. Michael, Giora Proskurowski, Thomas M. Mc Collom., 2011 "Chemistry of hot springs along the Eastern Lau Spreading Center." *Geochimica Et Cosmochimica Acta* 75, no. 4, 1013-1038.
- Nakashima, K., Sakai, H., Yoshida, H., Chiba, H., Tanaka, Y., Gamo, T., Ishibashi, J and Tsunogai, U., 1995. Hydrothermal mineralization in the Mid-Okinawa Trough. *Biogeochemical Processes and Ocean Flux in the Western Pacific* (Sakai, H and Nozaki, Y., eds.), 487-508, Terra Sci. Pub. Co., Tokyo.
- Newman, M.C., Jagoe, C.H., 1994. Ligands and the bioavailability of metals in aquatic environments. In: Hamelink, J.L., Landrum, P.F., Bergman, H.L., Benson, W.H. (Eds.), *Bioavailability: Physical, Chemical, and Biological Interactions*. Lewis Publications, Boca Raton, FL, pp. 39-62.
- Nirel, P.V., Morel, F.M., 1990. Pitfalls of sequential extractions. *Water Res.* 24: 1055-1056.
- Nomikou, P., Carey, S., Papanikolaou, D., Brill, K.C., Sakellariou, D., Alexandri, M., Bejelou, K., 2012. Submarine Volcanoes of the Kolumbo volcanic zone NE of Santorini Caldera, Greece. *Global and Planetary Change* 90-91, 135-151.
- Nomikou, P., Papanikolaou, D., Alexandri, S., Ballas, D., 2004. New insights on the Kos-Nisyros volcanic field from the morphotectonic analysis of the swath bathymetric map. *Rapp. Comm. Int. Mer. Medit.*, 37, 60.
- Nomikou, P., Papanikolaou, D., Carey, S., Bejelou, K., Sakellariou, D., Kiliass, S., Camilli, R., Escartin, J., Bell, K., Parks, M., 2013. Geodynamic features along the Christianna-Santorini-Kolumbo tectonic line (South Aegean Sea, Greece) *Geophysical Research Abstracts Vol. 15*, EGU2013-4552, EGU General Assembly 2013.

- Obolensky, A.A., Gushchina, L.V., Borisenko, A.S., Borovikov, A.A., Pavlova, G.G., 2007. Antimony in hydrothermal processes: solubility, conditions of transfer, and metal-bearing capacity of solutions. *Russian Geology and Geophysics* 48(12) 992–1001.
- Oorts, K., Smolders, E., Degryse, F., Buekers, J., Garso, G., Cornelis, G., Mertens, J., 2008. Solubility and toxicity of antimony trioxide (Sb₂O₃) in soil. *Environ. Sci. Technol* 42, 4378. doi:10.1021/ES703061T.
- Oremland, R. S., D. K. Newman, B. W. Kail, and J. F. Stolz.,** 2002. Bacterial respiration of arsenate and its significance in the environment, p. 273-296. *In* W. T. Frankenberger, Jr. (ed.), *Environmental chemistry of arsenic*. Marcel Dekker, Inc., New York, N.Y.
- Oremland, R.S., Stolz, J.F., 2003. The ecology of arsenic. *Science* 300(5621), 939-944.
- Papanikolaou, D., Nomikou, P., 2001. Tectonic structure and volcanic centres at the eastern edge of the Aegean volcanic arc around Nisyros Island. *Bulletin of the Geological Society of Greece* 34(1), 289-296.
- Papanikolaou, D., 1993. Geotectonic evolution of the Aegean. *Bull. Geol. Soc. Greece*, 27, 33-48.
- Pérez-Sirvent, C., Martínez-Sánchez, M.J., Martínez-López, S., Hernández-Córdoba, M., 2011. Antimony distribution in soils and plants near an abandoned mining site. *Microchemical Journal* 97, 52-56.
- Peter, J. M., & Goodfellow, W. D. (1996). Mineralogy, bulk and rare earth element geochemistry of massive sulphide-associated hydrothermal sediments of the Brunswick Horizon, Bathurst Mining Camp, New Brunswick. *Canadian Journal of Earth Sciences*, 33(2), 252-283.
- Petersen, S., Herzig, P.M., Hannington, M. D., Jonasson, I.R., Arribas, A., 2002. Submarine Gold Mineralization Near Lihir Island, New Ireland Fore-Arc, Papua New Guinea. *Econ. Geol.* 97, 1795-1813.
- Peterson, E. C., & Mavrogenes, J. A., 2014. Linking high-grade gold mineralization to earthquake-induced fault-valve processes in the Porgera gold deposit, Papua New Guinea. *Geology*, 42(5), 383-386.
- Pichler, T., Veizer, J., & Hall, G. E., 1999. The chemical composition of shallow-water hydrothermal fluids in Tutum Bay, Ambitle Island, Papua New Guinea and their effect on ambient seawater. *Marine Chemistry*, 64(3), 229-252.
- Planavsky, N. et al., 2009. Iron oxidizing microbial ecosystems thrived in late Paleoproterozoic redox-stratified oceans. *Earth Plan. Sci.* 286, 230–242 .
- Planavsky, N. et al., 2010a. Rare earth element and yttrium compositions of Archean and Paleoproterozoic Fe formations revisited: new perspectives on the significance and mechanisms of deposition. *Geochim. Cosmochim. Acta.* 74, 6387–6405.
- Planavsky, N., Bekker, A., Rouxel, O.J., Kamber, B., Hofmann, A., Knudsen, A., Lyons T.W., 2010b. Rare Earth Element and yttrium compositions of Archean and Paleoproterozoic Fe formations revisited: New perspectives on the significance and mechanisms of deposition. *Geochimica et Cosmochimica Acta* 74, 6387–6405.
- Pokrovski, G.S., Borisova, A.Y., Roux, J., Hazemann, J.L., Petdang, A., Tella, M., Testemale, Denis., 2006. Antimony speciation in saline hydrothermal fluids: A combined X-ray absorption fine structure spectroscopy and solubility study. *Geochimica et Cosmochimica Acta* 70, 4196-4214.
- Pokrovski, G.S., Zakirov, I.V., Roux, J., Testemale, D., Hazemann, J.L., Bychkov, A.Y., Golikova, G.V., 2002b. Experimental study of arsenic speciation in vapor phase to 500°C. Implications for As transport and fractionation in low density crustal fluids and volcanic gases. *Geochim. Cosmochim. Acta* 66, 3453-3480.

- Price, R.E., Pichler, T., 2005. Distribution, speciation and bioavailability of arsenic in a shallow-water submarine hydrothermal system, tutum Bay, Ambitle Island, PNG. *Chemical Geology* 224, 122-135.
- Qi, C.C., Wu, F.C., Deng, Q.J., Liu, G.J., Mo, C.L., Liu, B.J., Zhu, J., 2011. Distribution and accumulation of antimony in plants in the super-large Sb deposit areas, China. *Microchemical Journal* 97, 44–51.
- Ramdohr, Paul. 1980. *The ore minerals and their intergrowths*. Oxford: Pergamon Press.
- Rauret, G., Lopez-Sanchez, J.F., Sahuquillo, A., Rubio, R., Davinson, C., Ure, A., Quevauviller, ph., 1998. Improvement of the BCR three step sequential extraction procedure prior to the certification of new sediment and soil reference materials.. *J. Environ. Monit.*, 1999, 1, 57-61.
- Ravel, B., Newville, M., 2005. ATHENA, ARTEMIS, HEPHAESTUS: data analysis for X-ray absorption spectroscopy using IFEFFIT. *Journal of Synchrotron Radiation* v.12, Part 4, 537-541.
- Reich, M., Deditius, A., Chryssoulis, S., Li, J-W., Mae, C-Q., Parada, M.A., Barra, F., Mittermayr, F., 2013. Pyrite as a record of hydrothermal fluid evolution in a porphyry copper system: A SIMS/EMPA trace element study. *Geochimica et Cosmochimica Acta* 104, 42–62.
- Reich, M., Hough, R.M., Deditius, A., Utsunomiya S., Ciobanu, C.L. and Cook N. J., 2011. Nanogeoscience in ore systems research: principles, methods, and applications. *Ore Geol. Rev.* 42, 1–5.
- Reich, M., Kesler, S.E., Utsunomiya. S., Palenik, C.S., Chryssoulis, S.L., and ewing, R., 2005. Solubility of gold in arsenian pyrite. *Geochimica et Cosmochimica Acta*, 69, 2781-2796.
- Reich, M., Utsunomiya S., Kesler, S.E., Wang, L., Ewing, R.C., Becker, U., 2006. Thermal behavior of metal nanoparticles in geologic materials. *Geology*, (12), 1033-1036.
- Reimann, C., Matschullat, J., Birke, M., Salminen, R., 2010. Antimony in the environment: Lessons from geochemical mapping. *Applied Geochemistry* 25, 175-198.
- Relvas, J.M.R.S., Barriga, F.J.A.S., Ferreira, A., Noiva, P.C., Pacheco, N., Barriga, G., 2006. Hydrothermal alteration and mineralization in the Neves-Corvo volcanic-hosted massive sulfide deposit, Portugal. I. *Geology, mineralogy, and geochemistry. Econ. Geol.* 101, 753–790.
- Ring, U., Glodny, J., Will, T., Thomson, S., 2010. The Hellenic Subduction System: High-Pressure Metamorphism, Exhumation, Normal Faulting, and Large-Scale Extension. *Annu. Rev. Earth Planet. Sci.* 38, 45-76.
- Roper, A.J., Williams, P.A., and Filella, M., 2012, Secondary antimony minerals: Phases that control the dispersion of antimony in the supergene zone: *Chemie der Erde Geochemistry* 72, S4, 9-14.
- Royden, L. H., Papanikolaou, D. J., 2011. Slab segmentation and late Cenozoic disruption of the Hellenic arc. *Geochem. Geophys. Geosyst.* 12.
- Rudnick, R.L., Gao, S., 2003. Composition of the Continental Crust. *Treatise on Geochemistry: Ten Volume Set* Edited by Turekian, K.K., Holland, H.D.
- Safina, N.P., Maslennikov, V.V., 2009. Sequence of mineral formation in clastic ores of the Saf'yanovka. *Geology of Deposits*, 51, 7, 633-643
- Sakellariou, D., Sigurdsson, h., Alexandri, m., Carey, S., Rousakis, g., Nomikou, p., Georgiou, P., Ballas, D., 2010. Active tectonics in the hellenic volcanic arc: The Kolumbo submarine volcanic zone. *Bulletin of the geological society of Greece. Proceedings of the 12th Interbational Congress, Patras.*
- Salamons, W and Forstner, U., 1984. *Metals in the Hydrocycle*. Springer-Verlag, Berlin.

- Saunders, J. A. and Brueseke, M. E., 2012. Volatility of Se and Te during subduction-related distillation and the geochemistry of epithermal ores of the western United States. *Econ. Geol.* 107, 165–172 .
- Scheckel, K.G., Impellitteri, C.A., Ryan, J.A., Mc Evoy, T., 2003. Assessment of a sequential extraction procedure for perturbed lead contaminated samples with and without phosphorus amendments. *Environ. Sci. Technol.* 37: 1892-1898.
- Scheinost, A., Rossberg, A., Vantelon, D., Xifra, J., Kretzschmar, R., Leuz, A.K., Funke, H., Johnson, C.A., 2006. Quantitative antimony speciation in shooting-range soils by EXAFS spectroscopy. *Geochimica et Cosmochimica Acta* 70, 3299–3312.
- Schopf, J.W., Kudryavtsev, A.B., Czajac, A.D., Tripathi, A.B., 2007. Evidence of Archean life: Stromatolites and microfossils. *Precambrian Research* 158 141–155.
- Schwarz-Schampera, U., 2014. Antimony, in *Critical Metals Handbook* (ed G. Gunn), John Wiley & Sons, Oxford.
- Senn, D. B., Hemond, H. F., 2002 Nitrate controls on iron and arsenic in an urban lake. *Science* 296, 2373-2376.
- Sherman, D. M., Ragnarsdottir, K. V., & Oelkers, E. H. (2000). Antimony transport in hydrothermal solutions: an EXAFS study of antimony (V) complexation in alkaline sulfide and sulfide–chloride brines at temperatures from 25° C to 300° C. *Chemical Geology*, 167(1), 161-167.
- Shotyk, W., Chen, B., Krachler, M., 2005 Lithogenic, oceanic and anthropogenic sources of atmospheric Sb to a maritime blanket bog, Myrarna, Faroe Islands. *J. Environ. Monit* 7, 1148. doi:10.1039/B509928P.
- Sigurdsson, H., Carey, S., Alexandri, M., Vougioukalakis, Croff, K., Roman, C., Sakellariou, D., Anagnostou, C., Rousakis, G., Ioakim, C., Gogou, A., Ballas, D., Misaridis, T., Nomikou, P., 2006. Marine Investigations of Greece's Santorini Volcanic Field. *EOS* 87, 337-339.
- Smith, A. J. B., Beukes, N. J. & Gutzmer, J., 2013. The composition and depositional environments of Mesoarchean iron formations of the West Rand group of the Witwatersrand Supergroup, South Africa. *Econ. Geol.* 108, 111–134.
- Spycher, N.F., Reed, 1989. As(III) and Sb(III) sulfide complexes: an evaluation of stoichiometry and stability from existing experimental data. *Geochim. Cosmochim. Acta* 53, 2185-2194.
- Stoffers, P., Worthington, U., Schwarz-Schampera, U., Hannington, M.D., Massoth, M.D., Massoth, G.J., Hekinian, R., Schmidt, M., Lundsten, L.J., 2006. Submarine volcanoes and high-temperature hydrothermal venting on the Tonga arc, southwest Pacific. *Geology*; v.34; no.6; p. 453-456.
- Suzuki, R., Ishibashi, J.I., Nakaseama, M., Konno, Tsunogai, U., Gena, K., Chiba, H., 2008. Diverse Range of Mineralization Induced by Phase Separation of Hydrothermal Fluid: Case Study of the Yonaguni Knoll IV Hydrothermal Field in the Okinawa Trough Back-Arc Basin. *Resource Geology* Vol. 58, No. 3: 267 – 288.
- Sylvan, J.B., Toner, B.M., Edwards, K.J., 2012. Life and death of deep-sea vents: bacterial diversity and ecosystem succession on inactive hydrothermal sulfides. *mBio* 3: e00279–00211. doi: 10.1128/mbio.00279-11.
- Takahashi, Y., Sakuma, K., Itai, T., Zheng, G., Mitsunobu, S., 2008. Speciation of antimony in PET bottles produced in Japan and China by X-ray absorption fine structure spectroscopy. *Environ. Sci. Technol.* 42, 9045–9050.
- Tanaka, M., Shimizu, H and Masuda, A., 1990. Features of the heavy rare-earth elements in seawater. *Geochem. J.*, 24, 39-46.
- Tao, C., Li, H., Huang, W., Han, X., Wu, G., Su, X., Zhou, N., Lin, J., He, Y., Zhou, J., 2011. Mineralogical and geochemical features of sulfide chimneys from the 49°39'E hydrothermal field on the Southwest Indian Ridge and their geological inferences. *Chin. Sci. Bull.* 56:2828 –2838.

- Taylor, B.E., 2007. Epithermal gold deposits. In: Goodfellow, W.D. (ed.). Mineral deposits of Canada: A synthesis of major deposit types, district metallogeny, the evolution of geological provinces, and exploration methods. Geological Association of Canada, Mineral Deposits Division, Special Publication 5, 113-139.
- Telford, K., Maher, W., Krikowa, F., Foster, S., Ellwood, M.J., Ashley, P.M., 2009. Bioaccumulation of antimony and arsenic in a highly contaminated stream adjacent to the Hillgrove Mine, NSW, Australia. *Environ Chem* ; 6: 133–43.
- Tella, M., & Pokrovski, G. S. (2009). Antimony (III) complexing with O-bearing organic ligands in aqueous solution: an X-ray absorption fine structure spectroscopy and solubility study. *Geochimica et Cosmochimica Acta*, 73(2), 268-290.
- Tella, M., & Pokrovski, G. S. (2012). Stability and structure of pentavalent antimony complexes with aqueous organic ligands. *Chemical Geology*, 292, 57-68.
- Tessier, A., Campbell, P. G.C., Bisson, M., 1979. Sequential extraction Procedure for Speciation of Particulate Trace Metals. *Analytical chemistry*, 51(7).
- Thompson, J.F.H., Sillitoe, R.H., Baker, T., Lang, J.R., Mortensen, J.K., 1999. Intrusion-related gold deposits associated with tungsten-tin provinces. *Mineralium Deposita* 34, 323-334.
- Tivey, M.K., 2007. Generation of seafloor hydrothermal vent fluids and associated mineral deposits. *Oceanography*, 20 (1), 50-65.
- Ulrich, T., Long, D.G.F., Kamber, B.S., Whitehouse, M.J., 2011. In situ trace element and sulfur isotope analysis of pyrite in a paleoproterozoic gold placer deposit, Pardo and Clement Townships, Ontario, Canada. *Economic geology*, 106, 667-686.
- Van Grieken, R.E., Markowicz, A.A., 2002. *Handbook of X-Ray Spectrometry*. 2nd Edn, Marcel Dekker, New York.
- Varnavas S.P., Cronan D.S., 2005. Submarine hydrothermal activity off Santorini and Milos in the Central Hellenic Volcanic Arc: A synthesis. *Chemical Geology* 224, 40– 54.
- Voegelin, A., Kaegi, R., Frommer, J., Vantelon, D., Hug, S.J., 2010. Effect of phosphate, silicate, and Ca on Fe(III)-precipitates formed in aerated Fe(II)- and As (III)- containing water studied by X-ray absorption spectroscopy. *Geochimica et Cosmochimica Acta*, 74(1), 164-186.
- Von Damm and Lilley, 2004. Diffuse flow hydrothermal fluids from 9°50'N East Pacific Rise: Origin, evolution, and biogeochemical controls *Geophys. Monogr.*, AGU 144.
- Wedepohl, K.H., 1995. The composition of the continental crust. *Geochimica et Cosmochimica Acta* 59: 1, 217-1, 239.
- Williams-Jones A. E. and Normand C., 1997. Control of mineral parageneses in the system Fe-Sb-S-O. *Econ. Geol.* 92, 308–324.
- Williams-Jones, A.E., Normand, C., 1997. Controls of mineral parageneses in the system Fe-Sb-s-O. *Econ. Geol.* 92, 308-324.
- Wilson, S.C., Lockwood, P.V., Ashley, P.M., Tighe, M., 2010. The chemistry and behaviour of antimony in the soil environment with comparisons to arsenic: A critical review. *Environmental Pollution* 158, 1169-1181.
- Xu, L., Lehmann, B., & Mao, J. (2013). Seawater contribution to polymetallic Ni–Mo–PGE–Au mineralization in Early Cambrian black shales of South China: Evidence from Mo isotope, PGE, trace element, and REE geochemistry. *Ore Geology Reviews*, 52, 66-84.
- Xu, L., Wu, F., Zheng, J., Xie, Q., Li, H., Liao, X., Zhao, X., Guo, F., 2011. Sediment records of Sb and Pb stable isotopic ratios in Lake Qinghai. *Microchemical journal* 97, 25-29.
- Xu, Q., Scott S.D., 2005. Spherulitic pyrite in seafloor hydrothermal deposits: products of rapid crystallization from mixing fluids. In: Mao J, Bierlein FP (eds) *Mineral deposit research: meeting the global challenge*, vol 1. Springer, Berlin, 711–713.

- Zeng Z G, Jiang F Q, Qin Y S, et al., 2001 Rare earth element geochemistry of massive sulfides from the Jade hydrothermal field in the central Okinawa Trough (in Chinese). *Acta Geol Sin*, 75: 244–249
- Zhimin, C., Hong, C., Chunhui, T., Jun, L., Zenghui, Y., Liping, S., 2012. Rare earth element geochemistry of hydrothermal deposits from Southwest Indian Ridge. *Acta Oceanol. Sin.* 31(2), 62-69.
- Zotov, A. V., Shikina, N. D., & Akinfiyev, N. N., 2003. Thermodynamic properties of the Sb (III) hydroxide complex Sb (OH) at hydrothermal conditions. *Geochimica et Cosmochimica Acta*, 67(10), 1821-1836.